

Electronic Thesis and Dissertation Repository

---

4-18-2011 12:00 AM

# From Isolated Tumour Cells to Overt Lymph Node Metastases: Biological and Imaging Studies on the Development of Experimental Lymph Node Metastases

Michael M. Lizardo  
*The University of Western Ontario*

Supervisor

Dr. Ann F. Chambers  
*The University of Western Ontario* Joint Supervisor

Dr. Ian C. MacDonald  
*The University of Western Ontario*

Graduate Program in Medical Biophysics

A thesis submitted in partial fulfillment of the requirements for the degree in Doctor of  
Philosophy

© Michael M. Lizardo 2011

Follow this and additional works at: <https://ir.lib.uwo.ca/etd>



Part of the [Medical Biophysics Commons](#), [Neoplasms Commons](#), and the [Oncology Commons](#)

---

## Recommended Citation

Lizardo, Michael M., "From Isolated Tumour Cells to Overt Lymph Node Metastases: Biological and Imaging Studies on the Development of Experimental Lymph Node Metastases" (2011). *Electronic Thesis and Dissertation Repository*. 129.

<https://ir.lib.uwo.ca/etd/129>

This Dissertation/Thesis is brought to you for free and open access by Scholarship@Western. It has been accepted for inclusion in Electronic Thesis and Dissertation Repository by an authorized administrator of Scholarship@Western. For more information, please contact [wlsadmin@uwo.ca](mailto:wlsadmin@uwo.ca).

**From Isolated Tumour Cells to Overt Lymph Node Metastases:  
Biological and Imaging Studies on the  
Development of Experimental Lymph Node Metastases**

(Spine title: Experimental Lymph Node Metastases)

(Thesis format: Integrated-Article)

By

Michael M. Lizardo

Graduate Program  
In Medical Biophysics

A thesis submitted in partial fulfillment  
of the requirements for the degree of  
Doctor of Philosophy

School of Graduate and Postdoctoral Studies  
The University of Western Ontario  
London, Ontario, Canada

© Michael M. Lizardo 2011

THE UNIVERSITY OF WESTERN ONTARIO  
SCHOOL OF GRADUATE AND POSTDOCTORAL STUDIES

**CERTIFICATE OF EXAMINATION**

Supervisor

\_\_\_\_\_  
Dr. Ann Chambers

Co-Supervisor

\_\_\_\_\_  
Dr. Ian MacDonald

Examiners

\_\_\_\_\_  
Dr. Donna Goldhawk

\_\_\_\_\_  
Dr. Tamie Poepping

\_\_\_\_\_  
Dr. Peeyush Lala

\_\_\_\_\_  
Dr. Bruce Elliott

The thesis by

**Michael Lizardo**

entitled:

**From Isolated Tumour Cells to Overt Lymph Node Metastases:  
Biological and Imaging Studies on the Development of Experimental  
Lymph Node Metastases**

is accepted in partial fulfilment of the  
requirements for the degree of

**Doctor of Philosophy**

Date \_\_\_\_\_

\_\_\_\_\_  
Chair of the Thesis Examination Board

## ABSTRACT

Metastatic colonization and establishment of overt lymph node (LN) tumors indicates poor prognosis for cancer patients. However, the basic biology that influences the development of LN metastasis is poorly understood. The following work provides a new lymph node experimental metastasis assay (LEMA) that permits the assessment of tumor cell fate after they arrest in draining LNs. Using a mouse melanoma cell model, we discovered that only 8% of the tumor cells that arrive in the LN are successful in forming overt tumors. This work also explored the use of imaging approaches to monitor the process on LN metastasis in mice. To study the dynamic growth of LN metastases *in vivo*, we used three-dimensional high frequency ultrasound (HFUS) to non-invasively and longitudinally monitor the progression of LN metastases in mice. We observed that growth rates of LN tumors varied from mouse to mouse. Furthermore, HFUS allowed us to visualize small metastatic deposits and micrometastases and their growth over time. In order to provide some ground work for the development of magnetic resonance imaging (MRI) of lymph node metastases, we developed a gel phantom that simulated the progressive metastatic colonization of LNs. By labeling cells with gadofluorine M (GdF, a positive contrast agent), we were able to demonstrate that MRI ( at 3T) detected differences in tumor cell number in our gel phantom that contained a series of cell pellets with different percentages of labeled tumor cells mixed with unlabeled tumor cells. We found that the lower limit of detection of GdF-labeled cells was 546 cells per voxel. The research described herein will expedite future research



by providing a new experimental lymph node metastasis assay and novel imaging techniques that will permit the study of metastasis development in the lymph node.

**KEYWORDS:** lymphatic metastasis, lymph node metastasis, lymph node, metastasis, high frequency ultrasound, magnetic resonance imaging

## **CO-AUTHORSHIP**

Chapter 1 contains concepts and parts of a previously published review article “A New Breast Cancer Model for Lymphatic Metastasis,” by M.M. Lizardo, I.C. MacDonald, A.B. Tuck, and A.F. Chambers, in: *Cancer Metastasis and the Lymphovascular System Basis for Rational Therapy*, Leong S.P.L. (ed). Springer, 2007. I wrote this review with the assistance from I.C. MacDonald, A.B. Tuck, and A.F. Chambers.

Chapter 2 contains unpublished material that is currently being prepared as a manuscript for submission to *Clinical and Experimental Metastasis*. A.B. Tuck, I.C. MacDonald, and A.F. Chambers are providing supervision and assistance in editing the manuscript. I designed and developed the lymph node experimental metastasis assay (LEMA), and performed the animal surgeries with the help of N. Hague. I carried out the tissue processing, staining, and stereological analysis of histology sections. All histological sections were evaluated by a clinical pathologist A.B. Tuck.

Chapter 3 contains unpublished material that is currently being prepared as a manuscript for submission to *Investigative Radiology*. A.B. Tuck, I.C. MacDonald, J.C. Lacefield, and A.F. Chambers are providing supervision and assistance in editing the manuscript. I designed the experiments and imaging protocol. I performed the animal surgeries with the help of N. Hague. I carried out the ultrasound imaging, image segmentation and analysis. I carried out the tissue

processing, staining, and stereological analysis of the histology sections. All histological sections were evaluated by a clinical pathologist A.B. Tuck.

Chapter 4 contains unpublished materials that are currently being prepared as a manuscript for submission to Molecular Imaging and Biology. The manuscript was written with the assistance of J.A. Ronald and Y.Chen. P. Foster, B. K. Rutt, B. Misselwitz, I.C. MacDonald, and A.F. Chambers are providing supervision and assistance in editing the manuscript. The design of the experiments in this chapter was a collaborative effort between J.A. Ronald, and Y. Chen, and myself. I designed the cell culture experiments, construction of the MRI phantom, image analysis, and statistical analysis of data. J.A. Ronald provided the initial idea for the application of gadofluorine in assessing the detectability of cancer cells; Y. Chen provided his theoretical and practical knowledge in operating the MRI scanners. B Misselwitz provided positive contrast agents for the magnetic resonance imaging work.

## **ACKNOWLEDGMENTS**

The work presented in this thesis would not be possible without the guidance and support from my thesis advisors: Dr. Ann Chambers and Dr. Ian MacDonald. From Ann, I have learned about the importance and urgency of distilling biological inquiry into translatable knowledge. From Ian, I have gained invaluable experience in animal surgical techniques and intravital videomicroscopy. The complementary teachings of these two mentors have made me a better experimentalist in metastasis research.

I would also like to thank my collaborators at the Robarts Research Institute: Dr. James Lacefield and Dr. Paula Foster. I have gained a deeper appreciation about micro-ultrasound and cellular MRI, and I look forward to incorporating these imaging modalities in my future endeavors in metastasis research.

To members of the Chambers' group (past and present): Dr. Kevin Graham, David Dales, Carl Postenka, Carmen Simedrea, and most importantly Nicole Hague; I couldn't have done it on my own. Thank you!

My time in London wouldn't be as memorable without the friends I have made throughout the years: Danielle and John Ronald, Jason Townson and family, Jenn MacLean and family, Amanda Hamilton, Piya Lahiry, and Jen Mutrie, and Leslie Souter. To the students I have mentored over the years: Baraa Al-Khazraji, Dean Percy, Lenny Guizzetti, and Matthew Lowerison; it was a pleasure working and learning together.

## **GRANT SUPPORT**

The work described in this thesis has been supported in part through grant #42511 from the Canadian Institutes of Health Research.

Michael M. Lizardo was funded by studentships from the Translational Breast Cancer Research Unit of the London Regional Cancer Program, Strategic Training Fellowship in Vascular Research from the Canadian Institutes of Health Research, and Schulich Graduate Scholarship.

## TABLE OF CONTENTS

<b>CERTIFICATE OF EXAMINATION</b>	ii
<b>ABSTRACT</b>	iii
<b>CO-AUTHORSHIP</b>	v
<b>ACKNOWLEDGEMENTS</b>	vii
<b>GRANT SUPPORT</b>	viii
<b>THESIS TABLE OF CONTENTS</b>	ix
<b>LIST OF TABLES</b>	xvii
<b>LIST OF FIGURES</b>	xviii
<b>LIST OF ABBREVIATIONS</b>	xxi
<b><u>CHAPTER 1.0:</u> INTRODUCTION OF LYMPHATIC METASTASIS</b>	1
<b>1.1 NATURAL HISTORY OF         LYMPHATIC METASTASIS IN CANCER</b>	1
<b>1.2 LYMPHANGIOGENESIS</b>	2
<b>1.3 LYMPHOVASCULAR INVASION</b>	4
<b>1.4 LYMPH NODE METASTASIS</b>	5
1.4.1 Metastatic progression in the lymph node	6
1.4.2 Clues from studies of hematogenous experimental metastasis	8

<b>1.5</b>	<b>ANIMAL MODELS OF LYMPHATIC METASTASIS</b>	<b>9</b>
<b>1.6</b>	<b>UNANSWERED QUESTIONS</b>	<b>10</b>
<b>1.7</b>	<b>THESIS HYPOTHESIS</b>	<b>12</b>
<b>1.8</b>	<b>THESIS OBJECTIVE</b>	<b>12</b>
	1.8.1 Specific aims	12
<b>1.9</b>	<b>REFERENCES</b>	<b>14</b>
<b><u>CHAPTER 2.0: ASSESSING THE FATE OF ISOLATED TUMOUR CELLS</u></b>		
<b>AND MICROMETASTASES IN THE DEVELOPMENT</b>		
<b>OF OVERT LYMPH NODE METASTASES</b>		
		<b>21</b>
<b>2.1</b>	<b>INTRODUCTION</b>	<b>21</b>
<b>2.2</b>	<b>MATERIALS AND METHODS</b>	<b>26</b>
	2.2.1 Cell culture and cell labeling	26
	2.2.2 Animal model and surgical technique	27
	2.2.3 Micro-lymphangiography	28
	2.2.4 Lymph node staining and histology	28
	2.2.5 Histological and stereological analysis	29
	2.2.6 Determining tumour cell survival in lymph nodes	30
	2.2.7 Statistical analysis	31
<b>2.3</b>	<b>RESULTS</b>	<b>33</b>
	2.3.1 Experimental lymph node metastasis model	33

2.3.2	Incidence of isolated tumour cells, micrometastases, and overt metastases	38
2.3.3	Stereological analysis of whole-mount surface tumour burden	40
2.3.4	Stereological analysis of histological tumour burden	43
2.3.5	Consistent delivery of reference beads in all time-end point groups	46
2.3.6	Assessment of tumour cell survival and fate with respect to formation of micrometastases and overt metastases	49
2.3.7	Sinus histiocytes as a possible source of tumour cell toxicity in the lymph node	53
<b>2.4</b>	<b>DISCUSSION</b>	55
<b>2.5</b>	<b>REFERENCES</b>	60
<b><u>CHAPTER 3.0: HIGH-FREQUENCY (40 MHz) ULTRASOUND IMAGING</u></b>		
<b>OF THE DEVELOPMENT OF EXPERIMENTAL LYMPH</b>		
<b>NODE METASTASES</b>		66
<b>3.1</b>	<b>INTRODUCTION</b>	66
<b>3.2</b>	<b>MATERIALS AND METHODS</b>	70
3.2.1	Cell culture	70
3.2.2	Animal model and surgical technique	70
3.2.3	Ultrasound B-mode & power Doppler imaging	73
3.2.4	Ultrasound imaging analysis	76



3.2.5	Assessing sensitivity and specificity of ultrasound parameters in detecting lymph node metastases	77
3.2.6	Lymph node staining and histology	79
3.2.7	Histological and stereological analysis	79
3.2.8	Statistical analysis	80
<b>3.3</b>	<b>RESULTS</b>	<b>81</b>
3.3.1	Lymph node experimental metastasis assay	81
3.3.2	Changes in lymph node volume during the development of metastases	83
3.3.3	Changes in lymph node roundness index during the development of metastases	86
3.3.4	Changes in lymph node B-mode brightness during the development of metastases	89
3.3.5	Intranodal hyperechoic regions in lymph nodes correspond to small metastatic deposits	92
3.3.6	A positive correlation between ultrasound volumetric and histological area measurements	92
3.3.7	Longitudinal imaging of micrometastatic deposits and small metastases	97
3.3.8	Lymph node percent vascularity of negative lymph nodes and metastatic lymph nodes	99
3.3.9	The sensitivity and specificity of ultrasound parameters in the detection of lymph node metastases	101
<b>3.4</b>	<b>DISCUSSION</b>	<b>104</b>
<b>3.5</b>	<b>REFERENCES</b>	<b>108</b>

<b><u>CHAPTER 4.0:</u> THE CELLULAR DETECTABILITY OF POSITIVE CONTRAST-LABELED TUMOUR CELLS AT CLINICAL FIELD-STRENGTH MRI</b>	113
<b>4.1 INTRODUCTION</b>	113
<b>4.2 MATERIALS AND METHODS</b>	118
4.2.1 Cell culture and <i>in vitro</i> labeling with Gadofluorine M	118
4.2.2 Visualizing intracellular localization of GdF in breast cancer cells	119
4.2.3 In vitro MRI of cell pellets labeled at different GdF-loading concentrations	120
4.2.4 Measurement of $T_1$ relaxation times of cell pellets labeled at different GdF-loading concentrations	121
4.2.5 Quantification of intracellular GdF by inductively coupled plasma atomic emission spectroscopy	122
4.2.6 Construction of gel phantom for in vitro MRI scanning	122
4.2.7 Evaluating 3D SPGR and FIESTA pulse sequences for imaging an MRI phantom	123
4.2.8 Measurements of $T_1$ relaxation times of cell pellets containing different ratios of GdF-labeled tumour cells	124
4.2.9 Statistical analysis	124
<b>4.3 RESULTS</b>	126
4.3.1 Labeling efficiency and cell viability at different Loading concentrations of GdF	126

4.3.2	Visualization of intracellular localization of GdF by immunofluorescence microscopy	126
4.3.3	MRI of cell pellets with different loading concentrations of GdF scanned at 1.5T & 3T	130
4.3.4	Quantification of signal enhancement and $T_1$ relaxation of cell pellets of different GdF- loading conditions at 1.5T & 3T	130
4.3.5	Intracellular concentration of GdF of cell pellets over a range of GdF-loading conditions	131
4.3.6	In vitro MRI phantom to assess the detectability of GdF-labeled tumour cells at varying numbers	136
4.3.7	Comparison of CNR from 3D SPGR and FIESTA pulse sequences	136
4.3.8	Increased signal enhancement and $R_1$ relaxation rates of cell pellets with higher numbers of GdF- labeled tumour cells	140
4.3.9	The change in MR signal enhancement and $R_1$ measurements strongly correlates to the number of GdF-labeled tumour cells	140
<b>4.4</b>	<b>DISCUSSION</b>	145
<b>4.5</b>	<b>REFERENCES</b>	148
<b><u>CHAPTER 5.0: GENERAL DISCUSSION</u></b>		154
<b>5.1</b>	<b>THESIS SUMMARY</b>	154

<b>5.2</b>	<b>DISCUSSION – ASSESSING THE FATE OF ISOLATED TUMOUR CELLS AND MICROMETASTASES IN THE DEVELOPMENT OF OVERT LYMPH NODE METASTASES</b>	<b>156</b>
5.2.1	The need for a new model of lymph node Metastasis	156
5.2.2	LEMA and metastatic inefficiency in the lymph node	156
5.2.3	Clinical relevance	157
5.2.4	Future studies	158
<b>5.3</b>	<b>DISCUSSION – HIGH-FREQUENCY (40 MHz) ULTRASOUND IMAGING OF THE DEVELOPMENT OF EXPERIMENTAL LYMPH NODE METASTASES</b>	<b>159</b>
5.3.1	The utility of HFUS in tracking the dynamic growth of lymph node tumours	159
5.3.2	Non-invasive and longitudinal imaging of micrometastases	160
5.3.3	Clinical relevance	161
5.3.4	Future studies	161
<b>5.4</b>	<b>DISCUSSION – THE CELLULAR DETECTABILITY OF POSITIVE CONTRAST-LABELED TUMOUR CELLS AT CLINICAL FIELD STRENGTH MRI</b>	<b>163</b>
5.4.1	Problems in quantifying iron-oxide labeled tumour cells	163

5.4.2	Assessment of tumour cell number by positive contrast cellular MRI <i>in vitro</i> micrometastases	164
5.4.3	Clinical relevance	164
5.4.4	Future studies	165
<b>5.5</b>	<b>CONCLUSIONS</b>	<b>167</b>
<b>5.6</b>	<b>REFERENCES</b>	<b>168</b>
	<b>APPENDIX 1 – Copyright agreements</b>	<b>170</b>
	<b>APPENDIX 2 – Ethics approval for use of animal subjects</b>	<b>171</b>
	<b>CURRICULUM VITAE</b>	<b>172</b>

## LIST OF TABLES

TABLE	Page
<b>CHAPTER 2:</b>	
<b>Table 2.1</b> Metastasis incidence from experimental lymph node Metastasis assay.....	39
<b>CHAPTER 3:</b>	
<b>Table 3.1</b> Metastasis incidence from experimental lymph node Metastasis assay .....	82
<b>Table 3.2</b> Sensitivity and specificity of ultrasound parameters in detecting lymph node metastases.....	103

## LIST OF FIGURES

FIGURE		Page
<b>CHAPTER 1:</b>		
<b>Figure 1.1</b>	Schematic diagram of the progression of lymphatic metastasis .....	7
<b>CHAPTER 2:</b>		
<b>Figure 2.1</b>	Lymph node experimental metastasis assay (LEMA).....	36
<b>Figure 2.2</b>	A time-dependent experiments to study the progression of lymph node metastasis progression.....	37
<b>Figure 2.3</b>	Visualization and quantification of surface tumour burden of axillary lymph nodes.....	42
<b>Figure 2.4</b>	Quantification of time-dependent changes in histological tumour burden.....	45
<b>Figure 2.5</b>	Quantification of the average number of reference beads delivered per lymph node for all time points.....	48
<b>Figure 2.6.</b>	Quantification of the fate of tumour cells in the lymph node.....	51
<b>Figure 2.7.</b>	A flow chart showing the fate of tumour cells after they arrest in the axillary lymph node.....	52
<b>Figure 2.8</b>	Quantification of sinus histiocytes containing 3 $\mu$ m beads.....	54
<b>CHAPTER 3:</b>		
<b>Figure 3.1</b>	A novel animal model recapitulating lymph node metastasis.....	72

<b>Figure 3.2</b>	Imaging protocol to longitudinally study the progression of lymph node metastasis.....	75
<b>Figure 3.3</b>	Ultrasound analysis of lymph node volume during the development of metastases.....	85
<b>Figure 3.4</b>	Ultrasound analysis of lymph node roundness index during the development of metastases.....	88
<b>Figure 3.5</b>	Ultrasound analysis of lymph node B-mode brightness during the development of metastases.....	91
<b>Figure 3.6</b>	Hyperechoic subregions of the lymph node corresponding to micro- and macrometastatic deposits.....	95
<b>Figure 3.7</b>	Strong positive correlation between ultrasound volumetric and histological area measurements.....	96
<b>Figure 3.8</b>	Growth of small non-palpable metastatic deposits in lymph nodes.....	98
<b>Figure 3.9</b>	Lymph node percent vascularity of negative lymph nodes and metastatic lymph nodes.....	100

#### **CHAPTER 4:**

<b>Figure 4.1.</b>	Tumour cell uptake of GdF-cc, labeling efficiency, and cell viability from GdF-loading.....	128
<b>Figure 4.2</b>	Visualization of intracellular location of GdF-cc in tumour cells by immunofluorescent microscopy .....	129
<b>Figure 4.3</b>	Cellular MRI of cell pellets labeled at different loading concentrations of GdF.....	132
<b>Figure 4.4</b>	Cellular MRI of cell pellets at 1.5T and 3T.....	134
<b>Figure 4.5</b>	Measurement of intracellular GdF of cell pellets by ICP-AES....	135



<b>Figure 4.6</b>	MRI phantom to assess the sensitivity of positive-contrast enhancement at 3T in detecting differing amounts of GdF-labeled tumour cells.....	137
<b>Figure 4.7</b>	Comparison of image quality between 3D SPGR and FIESTA pulse sequences.....	139
<b>Figure 4.8</b>	MRI of cell pellets containing different proportions of GdF-labeled tumour cells.....	143
<b>Figure 4.9</b>	Changes in MR signal enhancement and $R_1$ values strongly correlate with the number of tumour cells per voxel.....	144

## LIST OF ABBREVIATIONS, SYMBOLS & NONMENCLATURE

<b><math>\alpha</math>-MEM</b>	<b>alpha minimal essential medium</b>
<b><math>\mu\text{m}</math></b>	<b>micrometer</b>
<b><math>\mu\text{m}^2</math></b>	<b>micrometer squared</b>
<b><math>\mu\text{M}</math></b>	<b>micromolar</b>
<b>2D</b>	<b>2 dimensional</b>
<b>3D</b>	<b>3 dimensional</b>
<b>3D HFUS</b>	<b>3 dimensional high frequency ultrasound</b>
<b>3D SPGR</b>	<b>3 dimensional spoiled gradient recalled</b>
<b>Ar</b>	<b>argon</b>
<b>ANOVA</b>	<b>analysis of variance</b>
<b>BSA</b>	<b>bovine serum albumin</b>
<b>BW</b>	<b>bandwidth</b>
<b>CCR7</b>	<b>chemokine cysteine-cysteine motif receptor type 7</b>
<b>cm</b>	<b>centimeter</b>
<b>CNR</b>	<b>contrast-to-noise ratio</b>
<b>CO<sub>2</sub></b>	<b>carbon dioxide</b>
<b>COX-2</b>	<b>cyclooxygenase-2</b>
<b>CXCR3</b>	<b>cysteine-x-cysteine chemokine receptor 3</b>
<b>DAPI</b>	<b>4',6-diamidino-2-phenylindole</b>
<b>dB</b>	<b>decibel</b>
<b>DTPA</b>	<b>diethylene triamine pentaacetic acid</b>
<b>EDTA</b>	<b>ethylenediaminetetraacetic acid</b>
<b>FIESTA</b>	<b>fast imaging employing steady state acquisition</b>
<b>FITC</b>	<b>fluorescein isothiocyanate</b>
<b>FPF</b>	<b>false positive fraction</b>

<b>Freq.</b>	<b>frequency</b>
<b>Gd</b>	<b>gadolinium</b>
<b>GdF</b>	<b>gadofluorine M</b>
<b>GdF-cc</b>	<b>gadofluorine M carbocyanine</b>
<b>HBSS</b>	<b>Hank's buffered salt solution</b>
<b>HFUS</b>	<b>high frequency ultrasound</b>
<b>HIFU</b>	<b>high intensity focused ultrasound</b>
<b>H&amp;E</b>	<b>hematoxylin and eosin</b>
<b>HNO<sub>3</sub></b>	<b>nitric oxide</b>
<b>ICP-AES</b>	<b>inductively coupled atomic emission spectroscopy</b>
<b>Ig</b>	<b>immunoglobulin</b>
<b>ITCs</b>	<b>isolated tumour cells</b>
<b>IVFVM</b>	<b>intravital fluorescence videomicroscopy</b>
<b>IVVM</b>	<b>intravital videomicroscopy</b>
<b>kHz</b>	<b>kiloHertz</b>
<b>kg</b>	<b>kilogram</b>
<b>Kr</b>	<b>krypton</b>
<b>LEMA</b>	<b>lymph node experimental metastasis assay</b>
<b>LMVD</b>	<b>lymphatic microvessel density</b>
<b>LN</b>	<b>lymph node</b>
<b>LYVE-1</b>	<b>lymphatic vessel endothelial receptor 1</b>
<b>M</b>	<b>molarity</b>
<b>mg</b>	<b>milligrams</b>
<b>MHz</b>	<b>megaHertz</b>
<b>ms</b>	<b>milliseconds</b>
<b>NEX</b>	<b>number of excitations</b>
<b>nm</b>	<b>nanometers</b>

<b>PET</b>	<b>positron emission tomography</b>
<b>Pp</b>	<b>point fraction</b>
<b>PV</b>	<b>percent vascularity</b>
<b>R<sub>1</sub></b>	<b>relaxation rate (s<sup>-1</sup>)</b>
<b>r<sup>2</sup></b>	<b>correlation coefficient</b>
<b>RI</b>	<b>roundness index</b>
<b>ROI</b>	<b>region of interest</b>
<b>SD</b>	<b>standard deviation</b>
<b>SE</b>	<b>standard error</b>
<b>SNR</b>	<b>signal-to-noise ratio</b>
<b>SPIO</b>	<b>superparamagnetic iron oxide</b>
<b>T<sub>1</sub></b>	<b>relaxation time (s)</b>
<b>TE</b>	<b>time to echo</b>
<b>TI</b>	<b>time to inversion</b>
<b>TPF</b>	<b>true positive fraction</b>
<b>TR</b>	<b>time to repetition</b>
<b>VEGF-C</b>	<b>vascular endothelial growth factor-C</b>
<b>VEGF-D</b>	<b>vascular endothelial growth factor-D</b>
<b>VEGF-R3</b>	<b>vascular endothelial growth factor receptor 3</b>

## **Chapter 1.0: Introduction of lymphatic metastasis**

### **1.1 Natural history of lymphatic metastasis in cancer**

Lymphatic vessels provide one of the main anatomical routes by which invasive tumour cells can disseminate from the primary tumour (Pantel and Brakenhoff, 2004). Certain types of cancer, including breast, prostate, and melanoma, have a propensity to disseminate via the lymphatics. Yet despite the prevalence of lymphatic metastasis, experimental work elucidating the underlying biology, until the last decade, has been relatively limited. In the past decade, there has been a surge in the number of studies uncovering the molecular determinants of lymphatic metastasis. The following chapter aims to highlight pre-clinical experimental work that contributes to our basic understanding of lymphatic metastasis. Before continuing, however, a brief overview of clinical and pathological studies that detail the natural history of lymphatic metastasis will establish the disease model which experimental models must mimic.

Physicians have described the spread of cancer to axillary lymph nodes as early as the 18<sup>th</sup> century (Weiss, 2000). Since then, a multitude of clinical and pathological studies have been published, suggesting that the lymphatic spread of breast cancer cells and formation of axillary lymph node metastases are common events in the natural history of the disease. The incidence of lymph node metastases in breast cancer is 30% to 50% (Foster 1996), 10% in prostate cancer (Swanson et al, 2006), and 50% in malignant melanoma (Buzzell and Zitelli, 1996). Upon review of the current literature, it is evident that there are at

least three potentially clinically relevant steps in lymphatic metastasis: 1) lymphangiogenesis, 2) lymphovascular invasion, and 3) lymph node metastasis.

## **1.2 Lymphangiogenesis**

Neo-vascularization contributes to the dissemination of tumour cells by increasing the likelihood of tumour cell intravasation into vessels (Folkman, 1992). In the context of lymphatic metastasis, it is reasonable to presume that increased lymphatic vessel density as a result of lymphangiogenesis would increase the likelihood of tumour cell invasion into lymphatic vessels. Indeed, there are clinical studies supporting this notion. Nakamura and colleagues (2005) examined archived and fresh frozen patient tissue samples, and demonstrated that elevated expression levels of vascular endothelial growth factor C (VEGF-C) was associated with increased lymphatic vessel density, lymph node metastases, and decreased patient survival. Schoppman and colleagues (2006) analyzed archival tissue from patients with invasive breast cancer and found a significant association between VEGF-C expression from tumour-associated macrophages and lymphatic microvessel density (LMVD), as well as LMVD and lymphovascular invasion. These findings support the idea of the local peritumoural inflammatory reaction that contains VEGF-C expressing macrophages, may contribute to lymphangiogenesis and thereby increasing the likelihood of lymphatic invasion by tumour cells (Coussens and Werb, 2002).

To model tumour-associated lymphangiogenesis, Skobe and associates (2001) engineered MDA-MB-435 human breast cancer cells to over-express VEGF-C. These cells were able to significantly increase intratumoural lymphangiogenesis when implanted in nude mice. Moreover over-expression of VEGF-C was also associated with a 60% increase in the incidence of lymph node metastasis. Similar findings have been demonstrated in MCF-7 human breast cancer cells (Karpanen et al, 2001; Mattila et al, 2002). Another growth factor that was discovered to stimulate lymphangiogenesis is VEGF-D. Stacker and colleagues (2001) transfected the non-metastatic 239EBNA cells to express VEGF-D (designated VEGF-D-293 cells). When injected into mice, VEGF-D-293 tumours had a higher amount of lymphatic vessels compared to tumours of the parental cell line. Furthermore, VEGF-D expression in VEGF-D-293 cells led to a higher incidence of lymph node metastases compared to parental cells. The authors demonstrated that the treatment of mice bearing VEGF-D-293 cells with anti-VEGF-D antibodies reduced the amount of tumour-associated lymphatic vessels, and inhibited the spread of tumour cells to draining lymph nodes. Metastasis to draining lymph nodes can also be inhibited by the administration of antibodies against the cognate receptor VEGF-R3, as demonstrated by Shimizu and colleagues in 2005.

Another biological factor that has been implicated in inducing tumour lymphangiogenesis is cyclooxygenase-2 (COX-2; Su et al, 2004; Timoshenko et al, 2006). Bhattacharjee and colleagues (2010) demonstrated that the role of

cyclooxygenase (COX)-2 in the up-regulation of VEGF-C production is associated with lymphangiogenesis in patient samples. In an experimental mouse model, the inhibition of COX-2 by etodolac resulted in both decreased tumour lymphangiogenesis and lymph node tumour burden (Iwata et al, 2007).

### **1.3 Lymphovascular invasion**

Tumour cell intravasation into lymphatic vessels is requisite for the initiation of lymphatic metastasis (Nathanson et al, 1997). Lymphatic or vascular invasion, a sign of poor prognosis, is commonly referred to as “lymphovascular invasion”, and means any involvement of an endothelial-lined space. Although it has been said that differentiating between vascular vs. lymphatic space involvement is not important in terms of prognostic value (both are felt to be associated with poor outcome), the use of this definition precludes the ability to tease out the relative significance of a lymphatic vs. a vascular route of metastasis. The development of new and improved markers of lymphatic endothelium, however, have allowed the specific evaluation of tumour cells found within lymphatic vessels, as defined by positive staining for markers such as lymphatic vessel endothelial hyaluronan receptor-1 (LYVE-1; Banurji et al, 1999), podoplanin (Breiteneder-Geleff et al, 1999), D2-40 (Kahn et al, 2002), or Prox-1 (Wigle and Oliver, 1999). Using dual-color immunofluorescence staining for LYVE-1 and podoplanin, Schoppman and colleagues (2004) demonstrated that lymphatic invasion was associated with an increased risk of developing lymph node metastasis, as well as lower overall patient survival. The same authors also



found a correlation between high lymphatic microvessel density and lymphatic invasion. This supports the notion that increased vessel density increases the likelihood of tumour cell intravasation, in the context of lymphatic vessels (Folkman, 1992).

#### **1.4 Lymph node metastasis**

The prognostic value of axillary lymph node metastasis has been well known, and provides one of the strongest prognostic factors in breast cancer (Foster, 1996, Koscielny and Tubiana, 1996; Fisher et al., 1984; Contesso et al, 1977; Nemoto et al, 1980; Peloquin et al, 1991). This is very well established for metastatic nodal deposits > 2.0 mm (Huvos et al, 1971). With lesser degrees of nodal involvement, the association with outcome is less clear. The preponderance of the literature would suggest that micrometastatic nodal involvement (ie. recognizable on routine H&E stained slides, as > 0.2 mm, but not > 2.0 mm; ) is also significant, but perhaps with a lesser degree of impact on prognosis (Maibenco et al, 2006; Park et al, 2009; Weaver et al, 2011). The clinical significance of nodal deposits no greater than 0.2 mm however (referred to as isolated tumour cells, pN0i<sup>+</sup> by AJCC 6<sup>th</sup> edition staging criteria) is controversial (Singletary and Greene, 2003; Querzoli et al, 2006).

#### **1.4.1 Metastatic progression in the lymph node**

As with step-wise progression of hematogenous (blood-borne) metastasis, lymphatic metastasis is presumed to be a step-wise phenomenon (Carr and Carr, 1982). From the aforementioned clinical data, we can model that lymphatic metastasis can occur in five steps, illustrated in the Figure 1.1. The steps depicted in Figure 1.1 manifest as distinct histopathological entities in the clinic, some of which have prognostic significance (eg. lymphatic invasion and lymph node metastasis). However, whether the model represents a true continuous progression has yet to be ascertained.

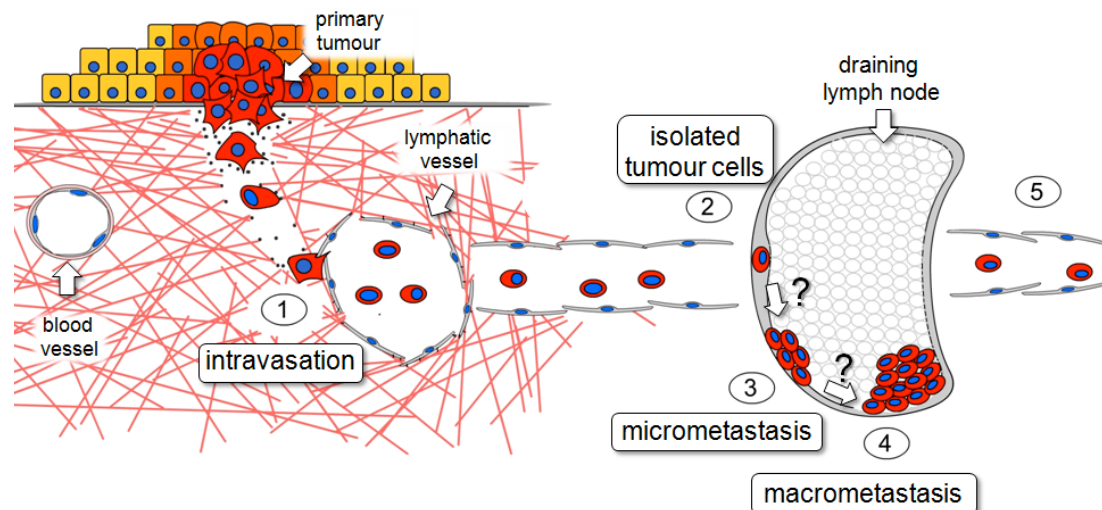


**Figure 1.1 Schematic diagram of the progression of lymphatic metastasis.**

(1) Tumour cell entry and transit within lymphatics (lymphatic invasion), (2) arrest in the draining lymph node as isolated tumour cells (ITCs), (3) formation of micrometastasis in the lymph node, (4) establishment of macrometastasis in the lymph node, and (5) further dissemination to downstream lymphatic vessels and lymph nodes.

#### **1.4.2 Clues from studies of hematogenous experimental metastasis**

Questions regarding the fate of tumour cells once they arrest at the secondary site can potentially be addressed by using the experimental tools that were used to ascertain the timing of events and molecular determinants of hematogenous metastasis, and applying them to the study of the lymphatic metastasis. For example, Luzzi and colleagues (1998), through the use of intravital videomicroscopy (IVVM), have demonstrated that tumour cells that are introduced into systemic circulation arrest and extravasate into secondary organs with high efficiency. However, only a small proportion of these cells was able to establish growth at the secondary site. More strikingly, Naumov and colleagues (1999) employed IVVM to demonstrate the presence of “dormant” single non-dividing cells that have extravasated into the liver parenchyma and have survived two weeks after injection. More recently, Heyn et al, (2006) employed magnetic resonance imaging (MRI) to study the fate of breast cancer cells in a mouse model of brain metastasis. Their work supports the notion that only a small proportion of extravasated tumour cells have the capacity to establish metastases. Using non-invasive imaging techniques to longitudinally monitor the lymphatic spread of tumour cells *in vivo* can provide insight into which step(s) of lymphatic metastasis do tumour cells accomplish with low efficiency, and thereby elucidating the rate-limiting step(s) of the process.

## 1.5 Animal models of lymphatic metastasis

With respect to experimental studies of lymphatic metastasis in breast cancer, earlier work in the 1970's by Ian Carr merits discussion. At the University of Saskatchewan, Carr and colleagues studied a series of rat mammary carcinomas that reproducibly metastasized to the popliteal lymph node when injected into the foot pad. In one study using Rd/3 cells, Carr and associates demonstrated that the primary tumour in the footpad continually seeds the popliteal lymph node with tumour cells thereby recapitulating the progressive steps of lymph node metastasis. However, if the footpad was removed before 24 hours have elapsed, progressive lymphatic metastasis did not occur (Carr and McGinty, 1976). In another study using Walker rat carcinoma cells, cannulation of the lymphatic trunk efferent to the primary tumour revealed a progressive rise, with time, in the number of tumour cells leaving the primary tumour (Carr et al, 1980).

To model tumour-associated lymphangiogenesis, Skobe and associates (2001) engineered MDA-MB-435 human breast cancer cells to over-express VEGF-C. These cells were able to significantly increase intratumoural lymphangiogenesis when implanted in nude mice. Moreover over-expression of VEGF-C was also associated with a 60% increase in the incidence of lymph node metastasis. Similar findings have been demonstrated in MCF-7 human breast cancer cells (Karpanen et al, 2001; Mattila et al, 2002).

There is mounting evidence suggesting tumour cells may actively migrate towards and intravasate into lymphatic vessels by conscripting the same mechanisms of adhesion and migration that leukocytes use for entry into the lymphatic system. In a seminal paper by Muller and associates (2001), the authors provide clinical and experimental data suggesting that breast cancer cells express chemokine receptors (CXCR-4) that actively promote tumour cell migration into lymphatics and draining lymph nodes. In their experimental mouse studies, the inhibition of CXCR-4 with neutralizing anti-CXCR-4 antibodies significantly inhibited metastasis to the inguinal and axillary lymph nodes and lung.

## **1.6 Unanswered questions**

The recent discoveries in lymphatic biology and lymphatic metastasis are indeed proving to be an exciting time in this field. Such studies are important in addressing questions regarding the progression of lymphatic metastasis. For example, during tumour progression, how many cells are shed into the lymphatics? What proportion of these tumour cells survives to form lymph node metastases? To what degree do lymph node metastases contribute (if at all) to systemic dissemination? What biological factors affect the progression of lymph node metastases? Such questions not only aim to determine the biological significance of isolated tumour cells (ITCs) and micrometastases, but to also find biological markers that have predictive value when assessing patient outcome.

These unanswered questions underscore the need for more models of lymphatic metastasis. Current experimental research is beginning to uncover the molecular determinants of lymphatic metastasis. However, at the same time, it's also important to develop imaging models that permit the *in vivo* longitudinal imaging of the progression of lymphatic metastasis. The intersection between imaging and biological modeling of lymphatic metastasis will be a forward-thinking approach to investigating the *in vivo* dynamics of lymphatic metastasis; and more importantly, such models will permit the non-invasive and longitudinal evaluation of the efficacy of anti-lymphatic metastatic therapeutics.

## 1.7 THESIS HYPOTHESIS

Based on previous studies examining tumour cell fate in secondary organs such as the liver, lung, and brain, it is hypothesized that metastasis progression in lymph nodes is an inefficient process. Specifically, it is predicted that cancer cell survival will significantly decrease over progressive time points.

## 1.8 THESIS OBJECTIVE

To address the above hypothesis, the primary objective of this thesis is to develop and characterize a novel lymph node experimental metastasis assay that recapitulates the progressive steps of metastasis development in the lymph node. This model will be used to assess tumour cell fate (cancer cell survival) after their arrest in the lymph node

### 1.8.1 SPECIFIC AIMS

- 1) To create a new lymph node experimental metastasis assay (LEMA) that permits the quantification of tumour cell fate after arrest in draining lymph nodes
- 2) To assess the utility of high frequency ultrasound in the non-invasive and longitudinal characterization of lymph node metastasis development *in vivo*



- 3) To develop quantitative methods that utilize positive-contrast MRI to assess tumour cell number in a lymph node phantom.

## 1.9 References

- Banerji S, Ni J, Wang SX, et al. LYVE-1, a new homologue of the CD44 glycoprotein, is a lymph-specific receptor for hyaluronan. *Journal of Cell Biology*. 1999; 144: 789-801.
- Bhattacharjee RN, Timoshenko AV, Cai J, et al. Relationship between cyclooxygenase-2 and human epidermal growth factor receptor 2 in vascular endothelial growth factor –C up-regulation and lymphangiogenesis in human breast cancer. *Cancer Science*. 2010; 101: 2026-2032.
- Breiteneder-Geleff S, Soleiman A , Kowalski H, et al. Angiosarcomas express mixed endothelial phenotypes of blood and lymphatic capillaries: podoplanin as a specific marker for lymphatic endothelium. *American Journal of Pathology*. 1999; 154: 385-394.
- Buzzell RA, Zitelli JA. Favorable prognostic factors in recruitment and metastatic melanoma. *Journal of the American Academy of Dermatology*. 1996; 34: 798-803.
- Carr J, Carr I, Dreher B, et al. Lymphatic metastasis: invasion of lymphatic vessels and efflux of tumour cells in the afferent popliteal lymph as seen in the Walker rat carcinoma. *Journal of Pathology*. 1980; 132: 287-305.
- Carr I, McGinty F. Neoplastic invasion and metastasis within the lymphoreticular system. *Advances in Experimental Medicine and Biology*. 1976; 73: 319-329.

- Carr I, Carr J. Tumor Invasion and Metastasis: Experimental models of lymphatic metastasis. In: Liotta LA, IR Hart eds. *Developments in Oncology 7*. Boston, MA: Martinus Nijhoff Publishers; 1982: 189-206.
- Contesso G, Rouesse J, Petit JY, et al. Les facteurs anatomo-pathologiques du pronostic des cancers du sein. *Bulletin du Cancer*. 1977; 64: 525-236.
- Coussens LM, Werb Z. Inflammation and cancer. *Nature*. 2002; 420:860-867.
- Fisher ER, Sass E, Fisher B. Pathological findings from the NSABP Protocol 4: discriminants for tenth year treatment failure. *Cancer*. 1984; 53:712-723.
- Folkman J. The role of angiogenesis in tumor growth and metastasis. *Seminars in Oncology*. 1992; 6: 15-18.
- Foster RS. The Biologic and Clinical Significance of Lymphatic Metastasis in Breast Cancer. *Surgical Oncology Clinics of North America*. 1996; 5: 79-104.
- Heyn C, Ronald JA, Ramadan SS, et al. In vivo MRI of cancer cell fate at the single-cell level in a mouse model of breast cancer metastasis to the brain. *Magnetic Resonance Medicine*. 2006; 56: 1001-1010.
- Huvos AG, Hutter RV, Berg JW. Significance of axillary macrometastases and micrometastases in mammary cancer. *Annals of Surgery*. 1971; 173: 44-46.

- Iwata C, Kano MR, Komuro A, et al. Inhibition of cyclooxygenase-2 suppresses lymph node metastasis via reduction of lymphangiogenesis. *Cancer Research*. 2007; 67:10181-10189.
- Kahn HJ, Bailey D, Marks A. Monoclonal antibody D2-40, a new marker of lymphatic endothelium, reacts with Kaposi's sarcoma and a subset of angiosarcomas. *Modern Pathology*. 2002; 15:434-40.
- Karpanen T, Egeblad M, Karkkainen MJ, et al. Vascular endothelial growth factor C promotes tumor lymphangiogenesis and intralymphatic tumor growth. *Cancer Research*. 2001; 61: 1786-1790.
- Koscielny S, Le MG, Tubiana M. The natural history of human breast cancer: The relationship between involvement of axillary lymph nodes and the initiation of distant metastases. *British Journal of Cancer*. 1989; 59: 775-782.
- Lauria R, Perrone F, Carlomagno C, et al. The prognostic value of lymphatic and blood vessel invasion in operable breast cancer. *Cancer*. 1995; 76: 1772-1778.
- Luzzi KJ, MacDonald IC, Schmidt EE, et al. Multistep nature of metastatic inefficiency: dormancy of solitary cells after successful extravasation and limited survival of early micrometastases. *American Journal of Pathology*. 1998; 153: 865-873.

- Maibenco DC, Dombi GW, Kau TY, et al. Significance of micrometastases on the survival of women with T<sub>1</sub> breast cancer. *Cancer*. 2006; 107:1234-1239.
- Mattila, M M, Ruohola, J K, Karpanen, T, et al. VEGF-C induced lymphangiogenesis is associated with lymph node metastasis in orthotopic MCF-7 tumors. *International Journal of Cancer*. 2002; 98: 946-951.
- Muller A, Homey B, Soto H, et al. Involvement of chemokine receptors in breast cancer metastasis. *Nature*. 2001; 410: 24-25.
- Nakamura Y, Yasuoka H, Tsujimoto M, et al. Lymph vessel density correlates with nodal status, VEGF-C expression, and prognosis in breast cancer. *Breast Cancer Research and Treatment*. 2005; 91:125-132.
- Nathanson SD, Anaya P, Avery M, et al. Sentinal lymph node metastasis in experimental melanoma: relationships among primary tumor size, lymphatic vessel diameter, and 99mTc-labeled human albumin clearance. *Annals of Surgical Oncology*. 1997; 4: 161-168.
- Naumov GN, Wilson SM, MacDonald IC, et al. Cellular expression of green fluorescent protein, coupled with high-resolution in vivo videomicroscopy, to monitor steps in tumor metastasis. *Journal of Cell Science*. 1999; 112:1833-1842.

- Nemoto T, Vana J, Bedwani RN, et al. Management and survival of female breast cancer: results of a national survey by the American College of Surgeons. *Cancer*. 1980; 45:2917-2924.
- Pantel K, Brakenhoff RH. Dissecting the metastatic cascade. *Nature Reviews Cancer*. 2004; 4: 448-456.
- Park D, Karesen R, Naume B, et al. The prognostic impact of occult metastasis in early breast carcinoma. *Breast Cancer Research and Treatment*. 2009; 118:57-66.
- Peloquin A, Poljicak M, Falardeau M, et al. Cancer of the breast: a study of 1520 consecutive patients operated on between 1960 and 1980. *Canadian Journal of Surgery*. 1991; 34:151-156.
- Querzoli P, Pedriali M, Rinaldi R, et al. Axillary lymph node nanometastases are prognostic factors for disease-free survival and metastatic relapse in breast cancer patients. *Clinical Cancer Research*. 2006; 12:6696-6701.
- Schoppmann SF, Bayer G, Aumayr K, et al. Prognostic value of lymphangiogenesis and lymphovascular invasion in invasive breast cancer. *Annals of Surgery*. 2004; 240:306-312.
- Schoppmann SF, Fenzl A, Nagy K, et al. VEGF-C expressing tumor-associated macrophages in lymph node positive breast cancer: impact on lymphangiogenesis and survival. *Surgery*. 2006; 139:839-846.

- Shimizu K, Kubo H, Yamaguchi K, et al. Suppression of VEGFR-3 signaling inhibits lymph node metastasis in gastric cancer. *Cancer Science*. 2004; 95:328-333.
- Singletary SE, Greene FL. Revision of breast cancer staging: the 6th edition of the TNM Classification. *Seminars in Surgical Oncology*. 2003; 21:53-59.
- Skobe M, Hawighorst T, Jackson DG, et al. Induction of tumor lymphangiogenesis by VEGF-C promotes breast cancer metastasis. *Nature Medicine*. 2001; 7:192-198.
- Swanson GP, Thompson IM, Basler J. Current status of lymph node-positive prostate cancer: Incidence and predictors of outcome. *Cancer*. 2006; 107: 439-450.
- Stacker SA, Caesar C, Baldwin ME, et al. VEGF-D promotes the metastatic spread of tumour cells via the lymphatics. *Nature Medicine*. 2001; 7: 186-191.
- Su JL, Shih JY, Yen ML, et al. Cyclooxygenase-2 induces EP1- and HER-2/Neu-dependent vascular endothelial growth factor-C up-regulation: a novel mechanism of lymphangiogenesis in lung adenocarcinoma. *Cancer Research*. 2004; 64:554-564.
- Timoshenko AV, Chakraborty C, Wagner GF, et al. COX-2 mediated stimulation of the lymphangiogenic factor VEGF-C in human breast cancer. *British Journal of Cancer*. 2006; 94:1154-1163.

Weaver DL, Ashikaga T, Krag DN, et al. Effect of occult metastases on survival in node-negative breast cancer. *New England Journal of Medicine*. 2011; 364:412-421.

Weiss L. Metastasis of Cancer: A Conceptual History from Antiquity to the 1990s. *Cancer and Metastasis Reviews*. 2000; 19: 219-234.

Wigle JT, Oliver G. Prox1 function is required for the development of the murine lymphatic system. *Cell*. 1999; 96: 769-778



## **Chapter 2.0: Assessing the fate of isolated tumour cells and micrometastases in the development of overt lymph node metastases**

### **2.1 Introduction**

The dissemination of tumour cells into the lymphatic vasculature is common in the natural history of many types of cancer. After transit within the lymphatic vasculature, tumour cells eventually arrest and begin to colonize draining lymph nodes. The successful establishment of overt lymph node metastases (> 2 mm in diameter) becomes a clinically relevant event for the cancer patient since the assessment of the number of lymph node metastases and extent of nodal involvement is currently standard clinical practice in evaluating disease aggressiveness and determining patient prognosis (Das and Skobe, 2008). Although lymph node metastases themselves are not fatal to the patient, it is hypothesized that lymph node metastases act as reservoirs of metastatic cells which can disseminate further into systemic circulation (Sleeman, 2000; Morton et al, 2003). This notion is supported by Rebhun et al (2008), who demonstrated lymph node tumours can seed tumour cells into the systemic circulation.

Each step of the (lymphatic) metastatic cascade may be a rate-limiting step (Chambers et al, 2002; Pantel and Brakenhoff, 2004). From tumour cell invasion into local stroma, intravasation into nearby vessels, transit within vessels, arrest at the secondary site, and successful formation of overt metastases – all potentially offer a window of therapeutic intervention. Therefore,

in order to produce efficacious anti-metastatic treatments in the clinic, it is paramount to study and understand the basic underlying biology that drives each step of the cascade. Indeed, within the last decade, several groups in lymphatic metastasis research have studied a particular aspect of the cascade *in vivo* and conceived a novel anti-metastatic therapy. For example, Wiley and colleagues (2001) demonstrated how the lymphatic dissemination of B16 cells over-expressing chemokine receptor-7 can be inhibited by injecting neutralizing antibodies against C-C chemokine ligand 21 (cognate ligand of CCR7). In another study examining tumour-induced lymphangiogenesis, He and colleagues (2005) studied how blockage of VEGFR3 activation on lymphatic vessels by soluble VEGF-R3-Ig fusion proteins inhibited lymphangiogenesis and the incidence of lymph node metastases was reduced.

Despite the plethora of basic research studies examining how tumour cells gain entry into the lymphatic vasculature, relatively few studies have examined the events following tumour cell arrest in draining lymph nodes. With the exceptions of a few studies (Dadiani et al, 2006; Yokoyama et al, 2006), the majority of studies in lymphatic metastasis have regarded lymph node metastases as a “black-box” labeled “end-point” rather than being viewed as the result of a series of discrete steps involving a number of possible pathways (MacDonald et al, 2002). Clinical data provides evidence that earlier stages of lymph node metastases can manifest as the following histologically distinct entities whose prognostic significance is controversial: (1) isolated tumour cells

or clusters of tumour cells less than 0.2 mm in diameter, (2) micrometastases which are lesions greater than 0.2 mm and no greater than 2 mm, and finally (3) overt metastases greater than 2 mm (Kahn et al, 2006; Singletary et al, 2002). From these clinical observations, formation of lymph node metastases is presumed to begin with isolated tumour cells arresting in the subcapsular sinus of the lymph node. These tumour cells then proliferate to form a micrometastatic deposit, which eventually grows into an overt lymph node tumour. Despite the voluminous amount of clinical observations, exactly how each step progresses to the next is unknown. What proportion of isolated tumour cells survive to form micrometastases? What proportion of micrometastases grow into overt lymph node metastases? What genetic factors positively or negatively regulate the progression in each of these steps?

Insight into answering these questions comes from animal models of metastasis where the fate of tumour cells after arrest at the secondary site is quantified (Luzzi et al, 1998; Cameron et al, 2000, Heyn et al, 2006; Kienast et al, 2010). To quantify the fate of tumour cells, Luzzi et al (1998) and Cameron et al (2000) used an experimental metastasis assay in which tumour cells and similar sized reference beads are directly injected into the vessel upstream of the target organ. The reference beads permit a “cell accounting” analysis where the percent survival of the initial injected population of tumour cells that form metastatic lesions at progressive intervals can be calculated (MacDonald et al, 2002). Collectively, these studies demonstrate that upon arrival in the secondary

site, the progression of single tumour cells into overt metastases is an inefficient process. More specifically, the majority of single tumour cells that arrive in the secondary site do not survive to form overt tumours, and only 0.02% and 5.8% of tumour cells survive to form metastases in the liver and lung, respectively (Luzzi et al, 1998; Cameron et al 2000). Heyn and colleagues (2006) employed high-resolution cellular MRI to track the fate of magnetically labeled cancer cells arrested in the brain and determined that 1.5% of the cells were able to form metastases. Kienast et al (2010) also found similarly low values of efficiency in the brain; furthermore the authors define several critical steps unique to the brain microenvironment that contribute to this inefficiency. The studies described above focused on hematogenous metastasis. However, with respect to assessing metastatic inefficiency lymph node, there are currently no metastasis models that permit the quantification of the discrete series of events that occur after tumour cells arrest in the lymph node.

In the research described herein, the use of the B16F10 melanoma model is described in a novel metastasis assay, called lymph node experimental metastasis assay (LEMA), which permits the quantitative assessment of tumour cell fate after arrest in lymph nodes. We demonstrate how our model recapitulates the progressive steps of metastasis development: from isolated tumour cells, micrometastases, and overt lymph node metastases. Furthermore, using the “cell accounting” technique, we provide quantitative evidence that suggests metastasis formation in the lymph is also an inefficient process. We

found that only a small proportion of cells delivered to the lymph node (0.37%) go on to form micrometastases, and that even a smaller proportion (~0.08%) that arrest in the lymph node are successful in forming overt lymph node tumours.

## 2.2 Materials and Methods

### 2.2.1 Cell culture and cell labeling

Briefly, a B16F10 murine melanoma cell line carrying a lacZ expressing vector (Kirstein et al, 2009) was maintained in  $\alpha$ -MEM medium containing 10% fetal bovine serum at 37°C and 5% CO<sub>2</sub>. For labeling cells with 3 $\mu$ m microspheres, cells were grown in a T75 tissue culture flask using medium with fetal bovine serum until 80% to 90% confluent.

To determine if macrophages in the lymph node (sinus histiocytes) phagocytose the tumour cells, tumour cells were labeled with 3 $\mu$ m polystyrene beads (Polysciences, Warrington, Pennsylvania) *in vitro* prior to injection into mice. For cell labeling, 5mL of Opti-MEM medium (Invitrogen, Burlington, Ontario) containing  $1.68 \times 10^8$  beads were added to 70-80% confluent B16F10-LacZ cells (T75 flask) and incubated for 1 h at 37°C. After incubation, the media was aspirated, and cells were washed thoroughly with Hank's buffered salt solution (HBSS) to remove unincorporated 3 $\mu$ m beads. Cells were then trypsinized, centrifuged, then resuspended in HBSS. The cell pellet was washed twice in HBSS prior to performing a trypan blue exclusion assay to test cell viability. Cell viability was between 95-99%. From these cells, a working cell suspension containing  $1.5 \times 10^7$  B16F10-lacZ cells and  $7.5 \times 10^5$  16 $\mu$ m polystyrene reference beads (Polysciences), at a 20:1 cell:bead ratio, in a volume of 1mL was prepared for intranodal (inguinal) injection in mice.

### **2.2.2 Animal model and surgical technique**

Female C57Bl/6 mice (Harlan Sprague Dawley, Indianapolis, Indiana), 5 weeks of age, were cared for in accordance with standards of the Canadian Council on Animal Care, under an approved protocol of the University of Western Ontario Council on Animal Care. During surgery, mice were kept under gas anesthesia with 1.5% isoflurane in oxygen and restrained on a water-heated stage. A one-inch incision was made in the lower ventral midline, and skin and underlying fascia were bluntly dissected to expose the 4th mammary fat pad. The skin flap attached to the mammary gland was reflected back and pinned with sterile needles for easy access to the mammary fat pad and inguinal lymph node. Under a dissecting microscope, the surface of the inguinal lymph node was exposed by removing adjacent mammary fat pad tissue. A suspension of tumour cells and 16 $\mu$ m reference beads (200 $\mu$ L of working cell suspension described above) was infused into the lymphatic microvasculature via intranodal injection with a pulled borosilicate glass needle (inner diameter 200  $\mu$ m) that was connected to an 18 gauge needle and 1mL syringe with Tygon tubing. Infusion of the cell suspension was done over a period of 5 minutes. In order to maintain the tumour cell to reference bead ratio in the axillary lymph node, further seeding from tumour cell growth in the inguinal lymph node (site of injection) was prevented by surgically removing the inguinal immediately after completion of the injection. Large blood vessels connected to the mammary fat pad were cauterized. The surgical wound was closed with surgical staples. Mice were then

injected with Metacam (0.1mg/kg; Boehringer Ingelheim Vetmedica Inc, St. Joseph, Missouri) and saline and allowed to recover.

To assess the growth of tumour cells in the axillary lymph node at progressive time intervals, surgery and tumour cell injection was performed on 40 mice that were divided into 4 time end-point groups: 90 minutes, 3 days, 7 days, and 14 days post-injection, with 10 mice per group. At the end of each time interval, axillary lymph nodes were collected for gross morphological assessment, histological processing and analysis.

### **2.2.3 Micro-lymphangiography**

To highlight the lymphatic drainage pathway from the inguinal lymph node, a blue tissue marking dye TMD™ (Triangle Biomedical Sciences Inc., Durham, North Carolina) was injected in the same manner as described in the previous section.

### **2.2.4 Lymph node staining and histology**

At each time end-point, whole axillary lymph nodes and lungs were harvested and placed in ice-cold phosphate buffer (0.1 M sodium phosphate monobasic, 0.1 M sodium phosphate dibasic, pH 7.3 until the organs from all mice were collected. Organs were subsequently stained with X-gal (Bioshop, Burlington, Canada) solution as described by Goring *et al* (1987) to visualize LacZ-expressing cells. X-gal stained lymph nodes were imaged in whole mount using a SteREO Lumar (Zeiss, Toronto, Canada) dissection scope attached to a



Canon PowerShot A640 with a vertical and horizontal resolution of 180 dots per inch..

For histologic examination, fixed organs were paraffin-embedded for routine histological sectioning (thickness, 5  $\mu\text{m}$ ) and staining with hematoxylin and eosin (H&E). Digital images of histology sections were captured using a color CCD camera and analyzed using Optimas TM 6.1 image analysis software (Optimas Corporation, Bothell, Washington).

### **2.2.5 Histological and stereological analysis**

To acquire an estimate of the surface distribution of LacZ-expressing tumour cells in lymph nodes at each time point, a point count ( $P_P$ ) method described by Underwood (1970) was used to calculate the fractional surface area of the lymph node covered with tumour cells. Using ImageJ analysis software (Abramoff et al, 2004), a point grid consisting of squares with an area of 0.14  $\text{mm}^2$  was superimposed onto digital images of whole mount lymph nodes (both sides of the lymph node were assessed). The point estimate ( $P_P$ ) is calculated by determining the number of points falling on LacZ/melanin staining divided by the total number of points falling on the lymph node.

To calculate histological tumour-burden, the same point count method was applied to digital images of H&E sections of lymph nodes. Using a point grid consisting of squares with an area of  $1000\mu\text{m}^2$ ,  $P_P$  is calculated by determining the number of points falling in areas of frank tumour divided by the total number

of points falling on the lymph node.  $P_p$  was calculated for three 5  $\mu\text{m}$ -thick sections (spaced 20  $\mu\text{m}$  apart) per lymph node to obtain an average per mouse.

### **2.2.6 Determining tumour cell survival in lymph nodes**

To determine the percentage of injected melanoma cells that survived as isolated tumour cells, micrometastases, and/or overt metastases, we based our calculation on the assumption that metastatic deposits originated from a single cell (Fidler and Talmadge, 1986). As defined by the American Joint Committee on Cancer (Green et al, 2002 ; Singletary et al, 2002), isolated tumour cells are defined as tumour cell clusters that are less than 0.2 mm in diameter; micrometastases are tumour deposits larger than 0.2 mm but no larger than 2 mm; overt metastases are larger than 2 mm. Therefore, by tabulating the number of isolated tumour cells, micrometastases, and overt metastases from axillary lymph node wholemount images (1 wholemount image per mouse, 10 mice per time point) and the average number of reference beads from corresponding histology sections ( $n = 6$ ), the observed tumour cell-to-reference bead ratio for each lymph node was calculated for each time point. For each mouse in each time point, the observed ratio was divided by the initially injected tumour cell-to-reference bead ratio to calculate tumour cell survival. Reference bead counts for lymph node sections were obtained from the average of 6 histology sections per lymph node. To estimate the number of the reference beads per lymph node, the numerical density of reference beads per section volume (area of section  $\times$

section thickness, 5 $\mu$ m) was multiplied by the number of section volumes that fit in the total lymph node volume.

### **2.2.7 Statistical analysis**

Statistical analysis was performed using Microsoft Excel 2007 (Microsoft Corporation, Redmond, Washington) and GraphPad Prism version 4.0 (GraphPad Software Inc., San Diego, California) for Windows XP. When raw percentage values were binomial in distribution, raw values were transformed using the arcsine (square root(x)) function in order to normalize the distribution. The mean and standard deviation of transformed data were analyzed by one-way ANOVA to compare multiple groups. Upper and lower confidence intervals were calculated, back-transformed and graphed with the untransformed mean percentage value for each group. A p value < 0.05 was regarded statistically significant. To determine which groups were significantly different, Tukey's multiple comparisons test was used. When data were not percentage values, data were tested for normality using Kolmogorov-Smirnov test that is available in the Graphpad Prism software package.

When data were normal in distribution, parametric one-way ANOVA was used to compare the means of multiple groups, and post-hoc Tukey's multiple comparisons test was performed to determine which groups were significantly different. When data were not normally distributed, the means of multiple groups were compared by non-parametric Kruskal-Wallis ANOVA, and when means were found to be statistically different, a post-hoc Dunn's multiple comparisons

was performed to determine which groups were significantly different.

## 2.3 Results

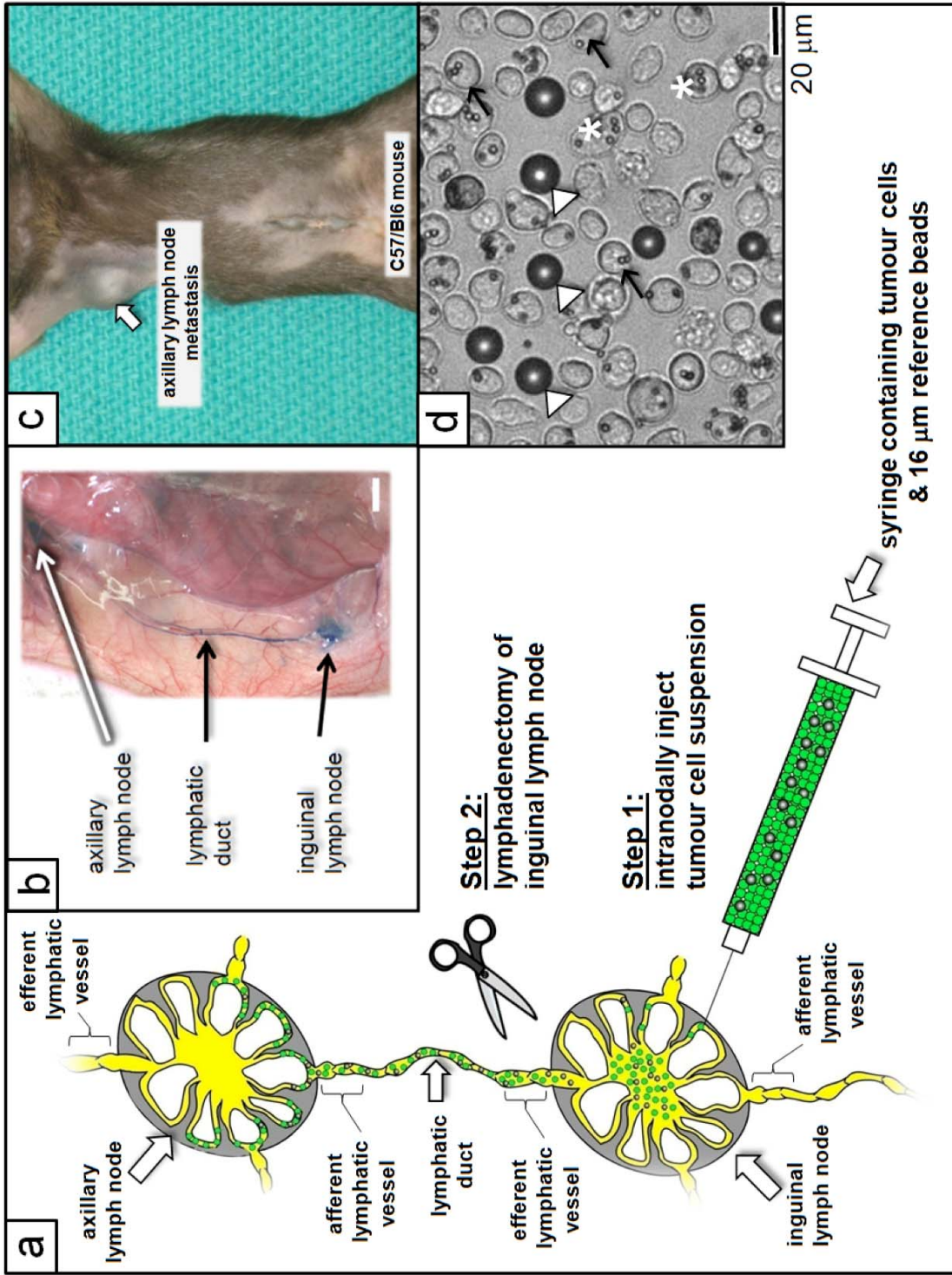
### 2.3.1 Experimental lymph node metastasis model

Our first goal was to devise and test a new *in vivo* model that recapitulated the progressive stages of metastasis development in the lymph node. This model utilizes two interconnected lymph nodes: the inguinal lymph node (injection site), and axillary lymph nodes (site of metastasis), as illustrated in Figure 2.1A. When labeling cells with 3 $\mu$ m beads *in vitro*, the majority of cells (~70%) were efficiently labeled with the beads, and labeling did not inhibit cell growth *in vitro* or the ability of cells to form metastases *in vivo* (data not shown). In the first step illustrated in Figure 2.1, a cell suspension, containing a ~16:1 mixture of B16F10-LacZ cells and 16 $\mu$ m reference beads (see Figure 2.1D), was injected directly into the inguinal lymph node. By applying slow and steady pressure to the syringe, the injectate traveled (~40 $\mu$ L per minute) through the inguinal lymph node, lymphatic duct, and drained into the axillary lymph node. This is simulated in Figure 1B, where a blue tissue dye was injected into the inguinal lymph node. In the second step, after injection, the inguinal lymph node was surgically removed to prevent tumour growth that may further seed the axillary lymph node, thereby abolishing the injected 16:1 tumour cell-to-bead ratio. Two weeks post-injection, overt axillary lymph node metastases were apparent (Figure 2.1C). To assess whether tumour cells were phagocytosed by immune cells, tumour cells were labeled with 3 $\mu$ m beads prior to injection into the inguinal lymph node (shown by black arrows in Figure 2.1D). We then used this

model to study the development of axillary lymph node metastases, by performing a time-dependent experiment that permitted the evaluation of changes in tumour burden at progressive time points as described in the **Methods & Materials** Section, section 2.2.2 (Figure 2.2).

**Figure 2.1 Lymph node experimental metastasis assay (LEMA).**

A diagram of the experimental lymph node metastasis model is shown (panel A). A suspension of tumour cells and 16  $\mu\text{m}$  reference beads are intranodally injected into the inguinal lymph node. Excess fluid pressure cause the suspension to leave the inguinal lymph node (via efferent lymphatic vessel) into the lymphatic duct. The cell suspension then arrives in the axillary lymph node via the afferent lymphatic vessel. Tumour cells and 16  $\mu\text{m}$  reference beads arrest in the subcapsular region of the afferent side of the axillary lymph node. In panel B, the drainage route of the cell suspension is simulated where a blue tissue dye was injected in the same manner to visualize the lymphatic drainage pathway. After injection with tumour cells, a large axillary lymph node metastasis became apparent after 14 days (panel C). In panel D, a bright-field micrograph is shown of the cell suspension containing B16F10-lacZ cells (white \*) and 16 $\mu\text{m}$  reference beads (white arrowheads) is shown. In addition, the B16F10-lacZ cells were pre-labeled with 3 $\mu\text{m}$  beads (black arrows) to determine if host cells phagocytosed tumour cells once they arrive in the lymph node. Scalebar = 20 $\mu\text{m}$  in Panel D.





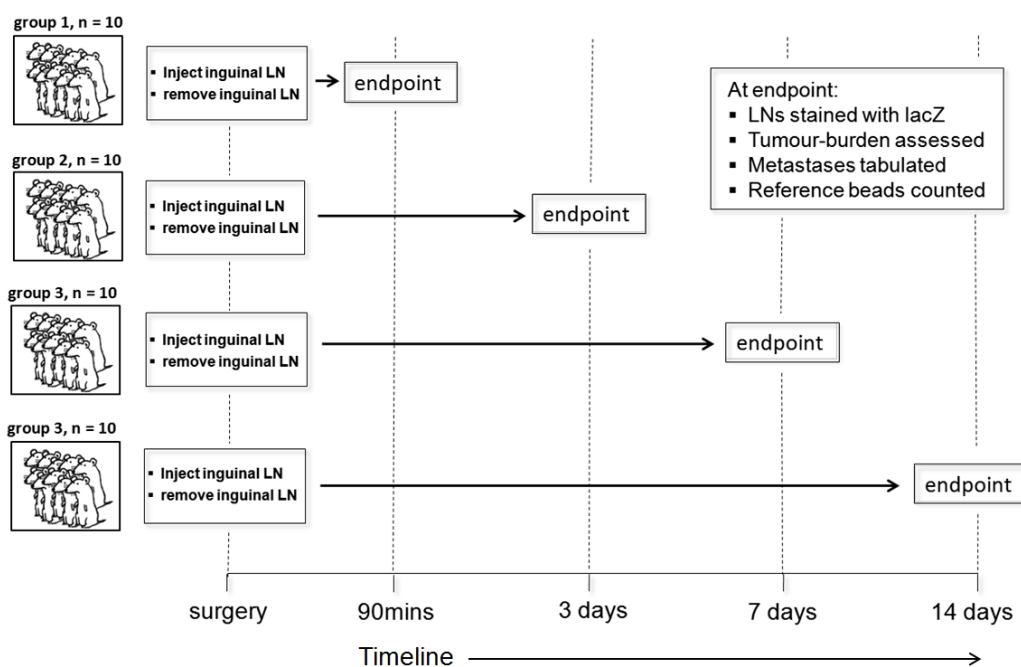


**Figure 2.2 A time-dependent study to investigate the progression of lymph node metastasis progression.** Forty mice underwent surgery in which B16F10-lacZ cells were intranodally injected into the inguinal lymph node of female C57/Bl6 mice. The inguinal lymph node was then surgically removed, and the mouse was allowed to recover. Forty mice were divided into 4 groups that were euthanized at 90 minutes, 3, 7, and 14 days post-injection. Lymph nodes were then examined for the presence of isolated tumour cells, micrometastases and overt metastases.

### **2.3.2 Incidence of isolated tumour cells, micrometastases, and overt metastases**

The growth of lymph node metastases over time, including incidences of each type of metastatic deposit (isolated tumour cells, micrometastases, overt metastases), is summarized in Table 2.1. The presence or absence of each type of lesion was tabulated. Shortly after injection into the inguinal lymph node (90 minutes), isolated tumour cells were observed in the axillary lymph node in all 10 mice. After 3 days had elapsed, isolated tumour cells were found in 9/10 mice, and micrometastases were found in 7/10 mice. At 7 days post-injection, no isolated tumour cells were found in any of the mice. The incidences of micrometastases and overt metastases were 1/10 and 2/10, respectively. By 14 days, 1/10 mice had a micrometastasis, and the majority of lymph nodes in mice (6/10) were overrun by tumour tissue. The assessment of incidence of a particular metastatic lesion type was binary: only the presence or absence of the lesion type was denoted. Since this did not provide information about the extent of nodal involvement, we subsequently assessed metastatic tumour burden by quantifying the proportion of lymph node surface area occupied by tumour and tumour area in histological sections.

Table 2.1 Metastasis incidence from experimental lymph node metastasis assay

Time elapsed post-injection n = 10 per group	Mean axillary lymph node volume (mm <sup>3</sup> ), mean + S.E. <sup>#</sup>	Metastatic lesion type		
		Isolated tumor cells <sup>1</sup>	Micrometastases <sup>2</sup>	Overt metastases <sup>3</sup>
		Incidence	Incidence	Incidence
90 minutes	13.0 ± 1.0 <sup>a</sup>	10/10	0/10	0/10
3 days	23.5 ± 3.8 <sup>b</sup>	9/10	7/10	0/10
7 days	40.5 ± 10.7	0/10	1/10	2/10
14 days	83.7 ± 23.9 <sup>a,b</sup>	0/10	1/10	6/10

<sup>1</sup> Tumor cell clusters less than 0.2mm in diameter, <sup>2</sup> Multicellular tumor foci between 0.2mm and 2mm in diameter, <sup>3</sup> Metastatic deposits larger than 2mm, 6<sup>th</sup> ed. AJCC Staging Manual (Green *et al.*, 2002).

<sup>#</sup> Means were significantly different from each other (ANOVA, p < 0.01).

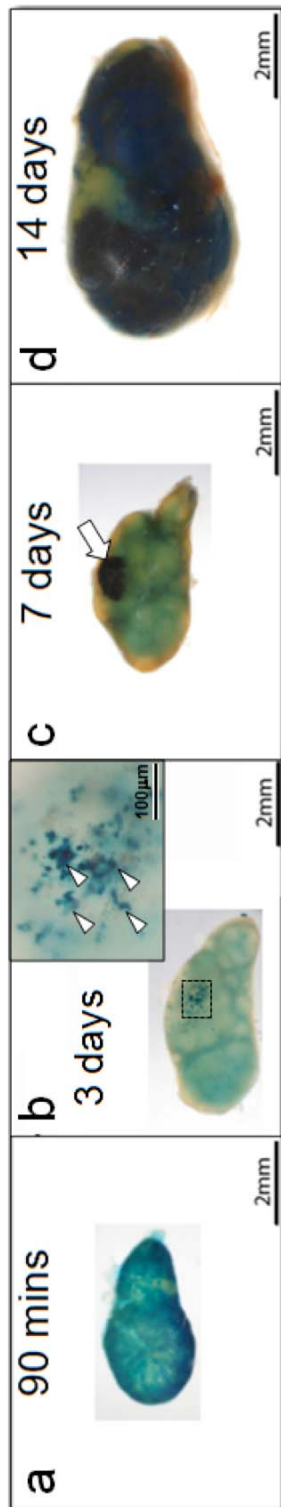
<sup>a,b</sup> Post-hoc Tukey's multiple comparison test, p < 0.01

### 2.3.3 Stereological analysis of whole-mount surface tumour burden

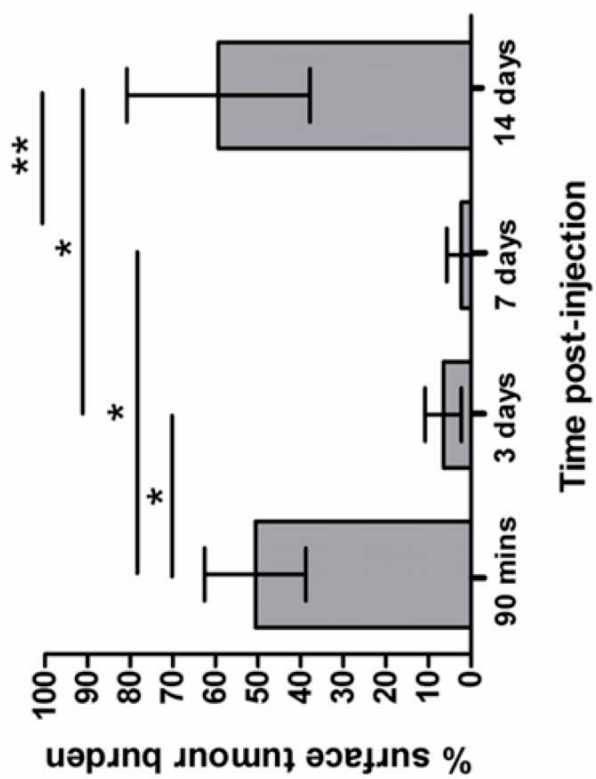
To measure the surface area of lymph nodes that was occupied by tumour, tumour cell expression of  $\beta$ -galactosidase (blue in color) on the surface of the lymph node was assessed. Representative axillary lymph nodes from each time point are shown in Figure 2.3 A-D. After injection into the inguinal lymph node, tumour cells drained into the subcapsular sinus of the axillary lymph node, and can be visualized as blue staining at the lymph node surface (90 minutes; Figure 2.3A). In Figure 2.3B, the surface distribution of tumour cells was reduced at 3 days post-injection. The reduction in surface tumour burden continued to decrease at 7 days. One lymph node harbored a micrometastasis at this timepoint, as shown in Figure 2.3C. By 14 days, large overt metastases had formed in the majority of lymph nodes, Figure 2.3D.

The observations above were supported by quantitative measurements of surface tumour burden as determined by stereological analysis (point count method) in Figure 2.3E, where the means ( $\pm$  standard deviations) are shown. At 90 minutes post-injection, tumour cells were found on average, to occupy 50.7% of the lymph node surface area. The surface area occupied by tumour cells significantly dropped to 10% and then 8%, at 3 and 7 days post-injection, respectively. By 14 days, the surface area of tumour tissue significantly rose to 54.6%, which reflects the increase in overt metastases at this time point (see Table 1).

**Figure 2.3 Visualization and quantification of surface tumour burden of axillary lymph nodes.** Panels A-D depict the stages of lymph node metastasis development: initial arrest of tumour cells in the lymph node (A), isolated tumour cells (B), micrometastasis (C), and an overt metastasis (D), at the time points indicated. Scalebar = 2 mm. In panel B, inset shows higher magnification showing clusters of isolated tumour cells (arrowheads). Scalebar = 100 $\mu$ m. The changes in surface tumour burden are quantified in panel E, where untransformed means and back transformed standard deviations are shown, n = 10 mice per group. Statistics were performed on transformed data in which the means were analyzed by one-way ANOVA ( $p < 0.001$ ), and a post-hoc Tukey's multiple comparisons test was used to determine which groups were significantly different from each other (\*  $p < 0.05$ , \*\*  $p < 0.01$ ).



**e**

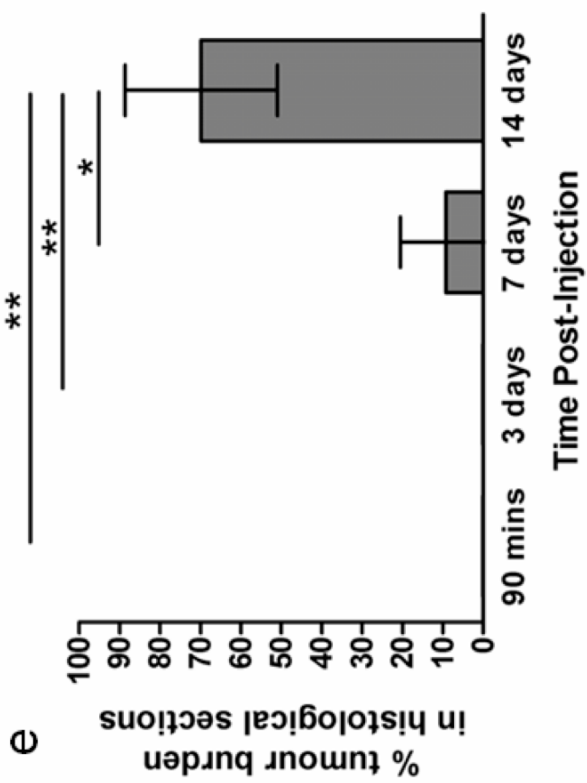
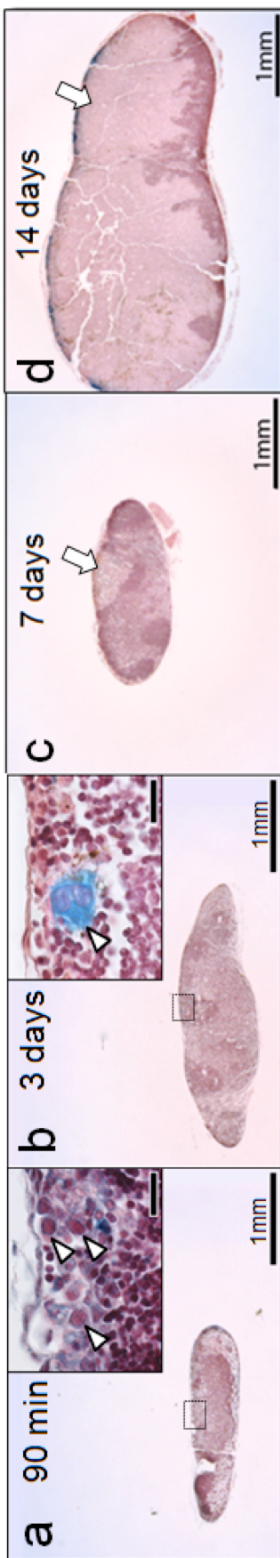


### 2.3.4 Stereological analysis of histological tumour burden

Analysis of surface tumour burden is useful in providing a whole (albeit superficial) view of metastatic colonization on a per-lymph node basis over progressive time points. To study the growth of metastatic deposits that extend beyond the subcapsular sinus, however, analysis of the histological cross-sections of the lymph node was performed. Figure 2.4A-D show representative histological cross-sections taken at each time point (low magnification, 25X). Although the presence of tumour cells was confirmed at higher magnification (1000X) at 90 minutes and 3 days post-injection (see insets of Figure 2.4A-B), histological tumour burden at low magnification did not become apparent until 7 and 14 days, as seen in panels C and D, respectively. This is due to the diminished sensitivity of the point count method in detecting single tumour cells at low magnification. Only when tumour deposits grow larger than  $0.01 \text{ mm}^2$  does the probability of a grid point falling on tumour tissue (and being enumerated) increase. The changes in histological tumour burden over time are shown in Figure 2.4E. The means and standard deviations are shown, where  $n = 10$  per group. The means of transformed data was analyzed by one-way ANOVA ( $p < 0.001$ ), and a post-hoc Tukey's multiple comparisons test was used to determine which groups were significantly different from each other (\*  $p < 0.5$ , \*\*\*  $p < 0.001$ ).

**Figure 2.4 Quantification of time-dependent changes in histological tumour burden.** Panels A-D show histological sections at low magnification (25X) that are representative of their respective time points. Scalebar = 1 mm. In A-B, although tumour burden was not apparent at low magnification, tumour cells are seen to be arrested in the subcapsular sinus at high magnification (1000X, see insets). Arrow heads denote the location of tumour cells. Scalebar = 20 $\mu$ m. Although single tumour cells are difficult to detect at 25X magnification, tumour burden can be quantified by the point count method at 25X magnification when micrometastases (an example shown in panel C) and overt metastases (an example in panel D) form. Histological tumour burden between the time groups are quantified in E, where untransformed mean and back transformed standard deviations are shown, n = 10 per group. The means of transformed data (as in square root) was analyzed by one-way ANOVA ( $p < 0.001$ ), and a post-hoc Tukey's multiple comparisons test was used to determine which groups were significantly different from each other (\*  $p < 0.05$ , \*\*\*  $p < 0.001$ ).





### **2.3.5 Consistent delivery of reference beads in all time-end point groups**

The role of 16  $\mu\text{m}$  reference beads is central to LEMA for two important points: (1) the observations on lymph node tumour burden over progressive time intervals are presumably due to an actual biological phenomenon rather than technical issues such as an inconsistent delivery of injectate between groups of mice, (2) the accuracy of quantifying tumour cell fate by the “cell accounting” technique hinges upon the reference beads arresting in the same anatomical regions as tumour cells due to their similarity in sizes. Both of these assumptions imply that the average number of reference beads do not significantly vary between groups of mice. Therefore to determine if these assumptions are correct, the average number of reference beads per section was counted in six histological sections spaced 25  $\mu\text{m}$  apart from each other. The graph in Figure 2.5 C demonstrates that the average number of reference beads per section did not significantly vary from 90 minutes, 3, 7 and 14 days. Furthermore, from these values we extrapolated the number of reference beads per entire volume of lymph node and found the values did not significantly vary from each other at any of the time points. Therefore we can conclude the two assumptions in LEMA are correct. One should note, however, there were 2 cases where reference beads were absent in histology sections. In one case, a mouse in the 3 day time point, where the lymph node harbored only a few scattered isolated tumour cells. The other case was in day 7 in a mouse where the lymph node was negative for

metastasis. Slides containing lymph node sections that did not contain reference beads could be due to sampling error when sectioning the lymph node during histological preparation.

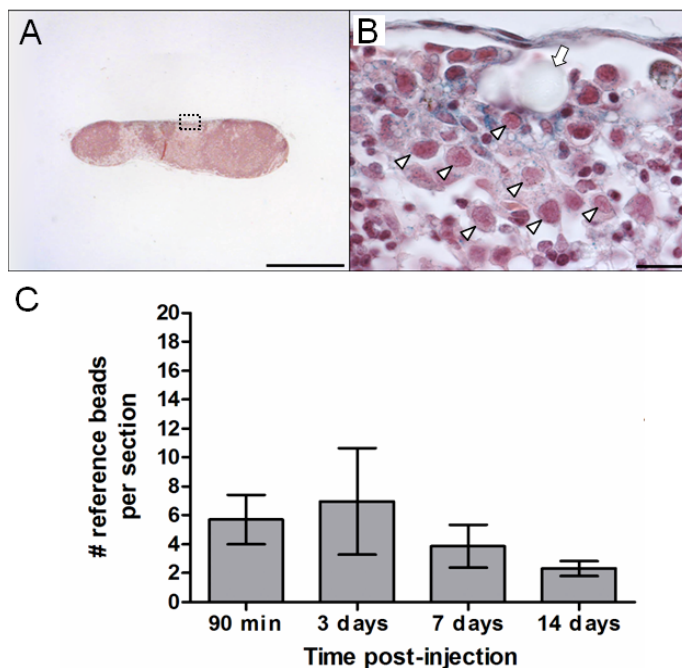
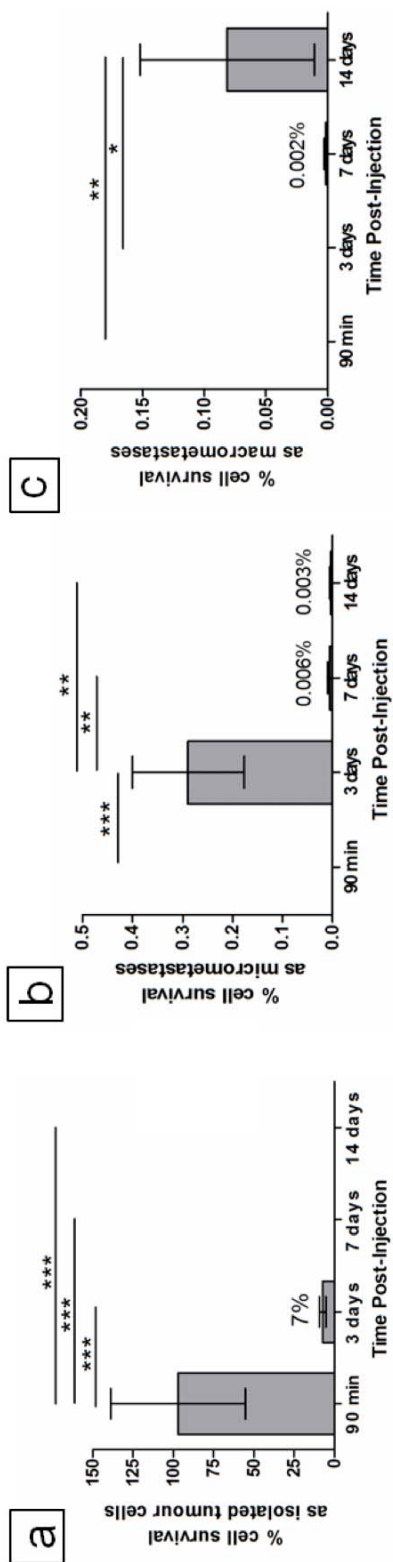


**Figure 2.5 Quantification of the average number of reference beads delivered per lymph node for all time points.** Panel A depicts an example of an area (subcapsular sinus, dashed box) where tumour cells and reference beads first arrest in the axillary lymph node. Scalebar = 2 mm. In B, a higher magnification of the dashed box area in A is shown. Arrow points to a reference bead, arrow heads denote tumour cells. Scalebar = 20 $\mu$ m. The mean number of reference beads per section was averaged from six sections per axillary lymph node per mouse. In panel C, the average of the means from all mice per time point are shown, error bars represent the standard error of the mean. The means were shown to not significantly vary between all time points, one-way ANOVA ( $p > 0.05$ ). The numbers of mice enumerated per time point were 10, 9, 9 and 10, at 90 minutes, 3, 7 and 14 days, respectively.

### **2.3.6 Assessment of tumour cell survival and fate with respect to formation of micrometastases and overt metastases**

In determining the fate of tumour cells after they arrest in the lymph node, we assumed that various types of metastatic deposits (isolated tumour cells, micrometastases, and overt metastases) are clonal in origin (Fidler and Talmadge, 1986). With this assumption, the percentage of tumour cells in the lymph node that have survived as a particular type of metastatic lesion was calculated. The percent tumour cells delivered to the lymph node that were present as isolated tumour cells, micrometastases, and overt metastases at the various time points is shown in Figure 2.6 A, B, and C, respectively. These survival data are summarized in the fate map in Figure 2.7, where stages of lymph node metastasis development are arranged in chronological order. 97% of the tumour cell injectate survived as isolated tumour cells at 90 minutes post-injection. Strikingly, tumour cell survival dropped from 97% to 7% from 90 minutes to 3 days. Single tumour cells were no longer found in the axillary lymph node beyond 3 days. Micrometastases that have formed at 3 days may contribute to the formation of overt metastases observed at 7 days post-injection. Also, some of the micrometastases at 3 days may have remained dormant, which may explain their presence at 7 and 14 days. In addition, there is a larger percentage of the originally delivered cells present as micrometastases at 3 days (0.36%), than detected as overt metastases at days 7 and 14, suggesting inefficiency in conversion from micrometastases to overt metastases.

**Figure 2.6.** Quantification of the fate of tumour cells in the lymph node. In panel A, the percentages of the tumour cells in the lymph node that survived as isolated tumour cells for each time point are shown. Means and standard errors are shown. Means were compared by parametric one-way ANOVA in graph A ( $p < 0.0001$ ), and Tukey's multiple comparisons test was used to determine which means were significantly different (\*\*\*,  $p < 0.001$ ). Panel B shows the percentage of the tumour cells in the lymph node that formed micrometastases. In panel C, at 7 and 14 days post-injection, the proportion of tumour cells in the lymph node that were able to successfully form overt tumours was 0.002% and 0.08%, respectively. Means and standard errors are shown. In graphs B & C, means were compared by non-parametric ANOVA (Kruskal-Wallis test) where  $p < 0.001$  and  $p < 0.01$ , respectively. Dunn's multiple comparisons test was used to determine which means were significantly difference (\*,  $p < 0.05$ ; \*\*,  $p < 0.01$ ; \*\*\*,  $p < 0.001$ ).



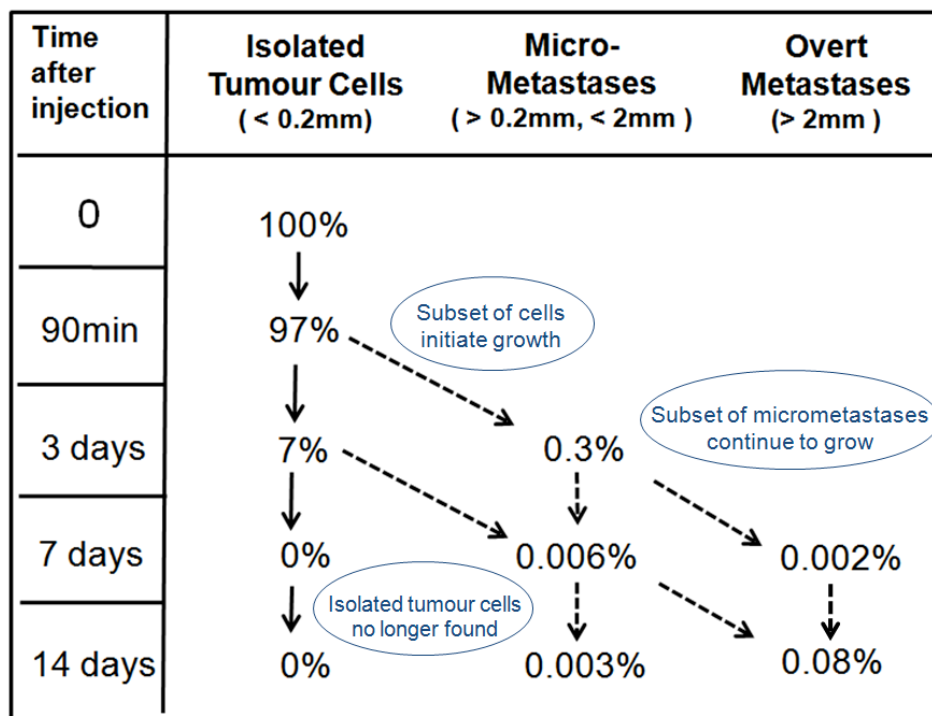


**Figure 2.7. A flow chart showing the fate of tumour cells after they arrest in the axillary lymph node.** Note the rapid loss of isolated tumour cells over time. The micrometastatic compartment also showed progressive loss from 3 days to 14 days post-injection. At 7 days, 0.002% of the tumour cells that arrested in the lymph node had formed overt metastases, and at 14 days, 0.08% of the tumour cells had formed overt metastases. Dotted arrows denote possible fates of the metastatic lesion. From this flow chart, it is apparent that there are several major sources of metastatic inefficiency in the lymph node: 1) there was a significant loss of isolated tumour cells and 2) only a small proportion of isolated tumour cells were able to form micrometastases, and 3) only a small proportion of micrometastases were able to successfully form overt metastases.



### **2.3.7 Sinus histiocytes as a possible source of tumour cell toxicity in the lymph node**

To determine if phagocytic activity of sinus histiocytes in the lymph node contributed to tumour cell death, tumour cells were pre-labeled with 3  $\mu\text{m}$  polystyrene beads prior to injection into mice. The greatest amount of tumour cell loss occurred between 90 minutes and 3 days post-injection of tumour cells. Therefore to assess whether sinus histiocytes contributed to tumour cell loss between these two time points, we examined lymph node histology sections for changes in the proportion of immune cells that contained 3  $\mu\text{m}$  beads from 90 minutes to 3 days (Figure 2.8). Indeed, we found that the average proportion of sinus histiocytes containing 3 $\mu\text{m}$  beads doubled from 90 minutes to 3 days, however this trend did not reach significance.

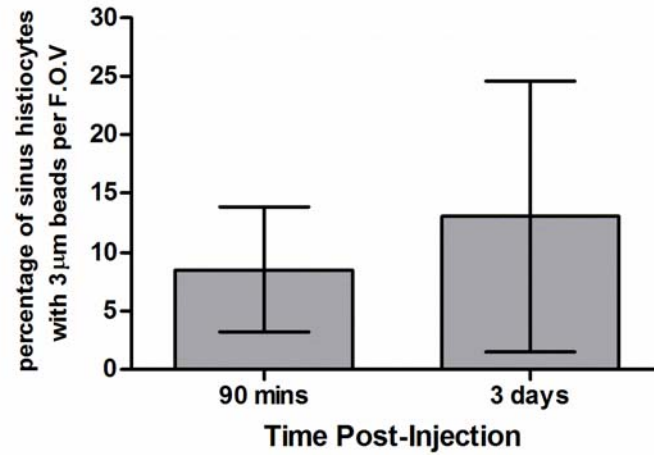


**Figure 2.8 Quantification of sinus histiocytes containing 3 μm beads.** A trend towards an increase in the number of sinus histiocytes containing 3 μm polystyrene beads from 90 minutes to 3 days post-injection is observed. The mean of averages and standard deviations are shown. The means were shown to not significantly vary between 90 minutes and 3 days (unpaired t-test,  $p > 0.05$ ).

## 2.4 Discussion

To date, research in lymphatic metastasis has largely focused on the site of the primary tumour where metastatic cells gain entry into lymphatic vessels. From these studies, several molecules have been implicated in promoting lymphatic metastasis *in vivo* including: VEGF-C (Karpanen et al, 2001; Hoshida et al, 2006), VEGF-D (Stacker et al, 2001), CXCR3 (Kawada et al, 2004), CCR7 (Wiley et al. 2001), and COX-2 (Bhattacharjee et al, 2010), to name several. Tumour cells gain entry into peritumoural lymphatic vessels and eventually drain into regional lymph nodes. The events occurring after tumour cell arrest in lymph nodes have been less studied in basic scientific literature. On the other hand, clinical data clearly demonstrate distinct histological stages of metastasis development which eventually result in clinically relevant overt metastasis. It is the subclinical metastatic lesions such as isolated tumour cells and micrometastases that stir controversy with respect to their impact on patient survival (Millis et al 2002; Imoto et al, 2006; Andersson et al, 2010). To clarify the biological significance of subclinical nodal disease, animal models are required to study the progression of single tumour cells to micrometastases, and eventually overt metastases. More importantly, cancer researchers can use these animal models to discover predictive biomarkers that can help clinicians easily assess the clinical impact of isolated tumour cells and micrometastases. However, there are very few appropriate animal models that permit the study of the events after tumour cell arrest in the lymph node (Yokoyama et al, 2006).

Thus, to devise an animal model that would permit a quantitative study of the events preceding the formation of overt lymph node metastases, I turned to previous studies of metastasis using the experimental (hematogenous) metastasis assay to quantify the fate of tumour cells after arrest at the secondary organ (Luzzi et al, 1998; Cameron et al 2000). LEMA uses the same approach as these previous studies by injecting a cell suspension with a known ratio of tumour cells and similar sized reference beads upstream of the secondary organ. Although the intranodal injection of tumour cells is an artificial method to introduce tumour cells into the lymphatic vasculature, the progressive steps of metastasis development in the axillary lymph node observed in this study (see Figure 2.4 A-D) mimics the progressive stages of metastasis development observed in patient lymph nodes – from isolated tumour cells, micrometastases, and overt lymph node metastases.

Once the tumour cells and 16  $\mu\text{m}$  reference beads arrest in the axillary lymph node, the reference beads permit a “cell accounting” analysis to be performed in which the percent survival values of the population of tumour cells that have arrested in the lymph node were calculated at progressive intervals. Our analysis revealed a precipitous drop in tumour cell survival from 97% to 7% from 90 minutes to 3 days post-injection, respectively. Thereafter, no isolated tumour cells were found. Also, we found that a small proportion of isolated tumour cells (ie. 0.36% from 90 minutes) survived to form micrometastatic deposits. We also observed that the number of micrometastases decreased over

time from ~0.3% to 0.003% from 3 to 14 days post-injection. Lastly, only 0.08% of the tumour cells that arrest in the lymph node were able to form overt metastases 14 days post-injection.

The metastatic inefficiency observed in the lymph node is similar to observations of metastasis progression in the liver (Luzzi et al, 1998), lung (Cameron et al, 2000), and brain (Heyn et al, 2006; Kienast et al, 2010) with a few notable differences. The drop in the number of isolated tumour cells from day 1 to 3 days post-injection is 6% in liver, 24% in lung, and ~ 5% to 41% in the brain (depending upon the cell line, Kienast et al, 2010), whereas in the lymph node, we saw a 90% drop from 90 minutes to 3 days post-injection. Another notable difference observed in the other studies is that the percent survival of the original tumour cell injectate arrested at the secondary site persisting as single non-dividing tumour cells is 36% in liver and 3.5% in lung (both after 14 days), 4.5% in brain after 28 days (Heyn et al 2006), and 1.7% after 42 days (Kienast et al, 2010), whereas in the lymph node, no single tumour cells were found at 7 or 14 days post-injection. From a broader perspective, these differences in metastatic efficiencies of different cell lines and the organ they grow in illustrate Paget's hypothesis that a disseminated cancer cells can only form metastases in organs that are permissive for growth (Paget, 1889).

The steep drop in the number of isolated tumour cells over time, and their absence at later time points observed in this model, suggest that the lymph node microenvironment is not conducive to the growth of single tumour cells when

compared to survival values in the previously mentioned studies. Peripheral lymph nodes are known to be major immunological sites harboring many types of immune cells including natural killer cells and phagocytic sinus histiocytes. These immune cells have been demonstrated to have anti-tumour activity in the lymph node in spontaneous metastasis assays (Kurokawa 1970; Carr and McGuinty, 1974; Yokoyama et al, 2006). Therefore, to determine if these immune cells play a role in the progressive loss of tumour cells in LEMA, B16F10-LacZ cells were labeled with 3 $\mu$ m polystyrene beads *in vitro* prior to injection into mice. Indeed the cytoplasm of sinus histiocytes was observed to contain 3 $\mu$ m beads, as well as blue and brown melanotic granules, at various time points, suggesting that histiocytes may contribute to the observed metastatic inefficiency in LEMA. At the same time, however, it is possible that tumour cells can die, and their cellular debris would be subsequently scavenged by sinus histiocytes, as is their function. Therefore, future studies using intravital videomicroscopy are needed to provide direct evidence of the role of sinus histiocytes in tumour cell loss in the lymph node.

The current study provides the first quantitative analysis of the steps leading to the formation of metastases in the lymph node. Although lymph node metastases themselves are not lethal to the patient (Das and Skobe, 2008), they may act as reservoirs of metastatic cells that can further disseminate into systemic circulation (Sleeman, 2000). Observations by Rehman and Fidler (2008) suggest that lymph node tumours can seed the lung with metastases with

equal propensity as the primary tumour. It would be interesting to determine if reducing the tumour burden in lymph nodes results in reduced lung tumour burden. If so, this would strengthen the notion of lymph node metastases as being reservoirs of metastatic cells. In the context with our study, we discovered that for this B16 melanoma model, metastasis formation is an inefficient process within the lymph node. As with previous reports on metastatic inefficiency, we also observed “bottleneck” effects where only a few isolated tumour cells or micrometastases can successfully progress to the next stage of metastasis development.

LEMA is a new metastasis assay that has been developed to address the need for animal models which permit the study of metastasis development in the lymph node microenvironment. This is the first report to quantify the fate of tumour cells after they arrest in the lymph node. The “bottleneck” effect observed at each step of metastasis suggests there are mechanisms that regulate how isolated tumour cells and micrometastases successfully form overt lymph node tumours. It is our hope this model will facilitate future research that will examine these regulatory mechanisms. In doing so, novel anti-metastatic therapeutics can be discovered that inhibit the formation of lymph node tumours, but more importantly, potentially prevent further systemic dissemination of metastatic cells.

## 2.5 References

Abramoff MD, Magelhaes PJ, Ram SJ. Image Processing with ImageJ. *Biophotonics International*. 2004; 11: 36-42.

Andersson Y, Frisell J, Sylvan M, et al. Breast cancer survival in relation to the metastatic tumour burden in axillary lymph nodes. *Journal of Clinical Oncology*. 2010; 28: 2868-2873.

Bhattacharjee RN, Timoshenko AV, Cai J, et al. Relationship between cyclooxygenase-2 and human epidermal growth factor receptor 2 in vascular endothelial growth factor –C up-regulation and lymphangiogenesis in human breast cancer. *Cancer Science*. 2010; 101: 2026-2032.

Cameron MD, Schmidt EE, Kerkvliet N, et al. Temporal progression of metastasis in lung: cell survival, dormancy, and local dependence of metastatic inefficiency. *Cancer Research*. 2000; 60:2541-2546.

Carr I, McGinty F. Lymphatic metastasis and its inhibition: an experimental model. *Journal of Pathology*. 1974; 113: 85-95.

Chambers AF, Groom AC, MacDonald IC. Dissemination and growth of cancer cells in metastatic sites. *Nature Reviews Cancer*. 2002; 2:563-572.



- Dadiani M, Kalchenko V, Yosepovich A, et al. Real-time imaging of lymphogenic metastasis in orthotopic human breast cancer. *Cancer Research*. 2006; 66(16): 8037-8041.
- Das S, Skobe M. Lymphatic vessel activation in cancer. *Annals of the New York Academy of Sciences*. 2008; 1131:235-241.
- Fidler IJ, Talmadge JE. Evidence that intravenously derived murine pulmonary melanoma metastases can originate from the expansion of a single tumour cell. *Cancer Research*. 1986; 46: 5167-5171.
- Green FL, Page DL, Fleming ID, et al. *AJCC Cancer Staging Manual* 6<sup>th</sup> ed. 2002; Springer, New York, New York, USA
- Gorring DR, Rossant J, Clapoff S, et al. In situ detection of beta-galactosidase in lenses of transgenic mice with a gamma-crystallin/lacZ gene. *Science*. 1987; 235(4787): 456-458.
- He Y, Rajante I, Pajusola K et al. Vascular endothelial cell growth factor receptor 3-mediated activation of lymphatic endothelium is crucial for tumour cell entry and spread via lymphatic vessels. *Cancer Research*. 2005; 65(11): 4739-4746.
- Heyn C, Ronald JA, Ramadan SS, et al. In vivo MRI of cancer cell fate at the single-cell level in a mouse model of breast cancer metastasis to the brain. *Magnetic Resonance in Medicine*. 2006; 56:1001-1010.

Hoshida T, Isaka N, Hagendoorn J, et al. Imaging steps of lymphatic metastasis reveals that vascular endothelial growth factor-C increases metastasis by increasing delivery of cancer cells to lymph nodes: therapeutic implications. *Cancer Research*. 2006; 66: 8065-8075.

Imoto S, Ochiai A, Okumura C, et al. Impact of isolated tumour cells in sentinel lymph nodes detected by immunohistochemical staining. *European Journal of Surgical Oncology*. 2006: 1-5.

Kahn HJ, Hanna WM, Chapman JA, et al. Biological significance of occult micrometastases in histologically negative axillary lymph nodes in breast cancer patients using the recent American Joint Committee on Cancer Breast Cancer Staging System. *The Breast Journal*. 2006; 12: 294-301.

Karpanen T, Egeblad M, Karkkainen MJ, et al. Vascular endothelial growth factor C promotes tumour lymphangiogenesis and intralymphatic tumour growth. *Cancer Research*. 2001; 61:1786-1790.

Kawada K, Sonoshita M, Sakashita H, et al. Pivotal role of CXCR3 in melanoma cell metastasis to lymph nodes. *Cancer Research*. 2004; 64: 4010-4017.

Kienast Y, von Baumgarten L, Fuhrmann M, et al. Real-time imaging reveals the single steps of brain metastasis formation. *Nature Medicine*. 2010; 16(1): 116-123.

Kirstein JM, Graham KC, MacKenzie LT, et al. Effect of anti-fibrinolytic therapy on experimental melanoma metastasis. *Clinical and Experimental Metastasis*. 2009; 26: 121-131.

Kurokawa Y. Experiments on lymph node metastasis by intralymphatic inoculation of rat ascites tumour cells, with special reference to lodgement, passage, and growth of tumour cells in lymph node. *Gann*. 1970; 61: 461-471.

Luzzi KJ, MacDonald IC, Schmidt EE, et al. The multistep nature of metastatic inefficiency. *American Journal of Pathology*. 1998; 153:865-873.

MacDonald IC, Groom AC, Chambers AF. Cancer spread and micrometastasis development: quantitative approaches for in vivo models. *Bioassays*. 2002; 24: 885-893.

Millis RR, Springall R, Lee AH, et al. Occult axillary lymph node metastases are of no prognostic significance in breast cancer. *British Journal of Cancer*. 2002; 86: 396-401.

Morton DL, Hoon DS, Cochran AJ et al. Lymphatic mapping and sentinel lymphadenectomy for early-stage melanoma. Therapeutic utility and implications of nodal microanatomy and molecular staging for improving the accuracy of detection of nodal metastases. *Annals of Surgery*. 2003; 238(4): 538-550.

- Paget S. The distribution of secondary growths in the cancer of the breast. *Lancet*. 1889; 133: 571-573.
- Pantel K, Brakenhoff RH. Dissecting the metastatic cascade. *Nature Reviews Cancer*. 2004; 4: 448-456.
- Querzoli P, Padriali M, Rinaldi R, et al. Axillary lymph node nanometastases are prognostic factors for disease-free survival and metastatic relapse in breast cancer patients. *Clinical Cancer Research*. 2006; 12 6696-6701.
- Rebhun RB, Lazar AJ, Fidler IJ. Impact of sentinel lymphadenectomy on survival in a murine model of melanoma. *Clinical and Experimental Metastasis*. 2008; 25:191-199.
- Singletery SE, Allred C, Ashley P, et al. Revision of the American Joint Committee on Cancer Staging System for Breast Cancer. *Journal of Clinical Oncology*. 2002; 20): 3638-3636.
- Sleeman JP. The lymph node as a bridgehead in the metastatic dissemination of tumours. *Recent Results in Cancer Research*. 2000; 157: 55-81.
- Stacker SA, Caesar C, Baldwin ME, et al. VEGF-D promotes the metastatic spread of tumour cells via the lymphatics. *Nature Medicine*. 2001; 7: 186-191.
- Underwood EE. *Quantitative Stereology*. 1970. Addison-Wesley, Massachusetts, USA.

Wiley HE, Gonzales EB, Maki W, et al. Expression of CC chemokine receptor-7 and regional lymph node metastasis of B16 murine melanoma. *Journal of the National Cancer Institute*. 2001; 92(21): 1638-1643.

Yokoyama H, Nakanishi H, Kodera Y, et al. Biological significance of isolated tumour cells and micrometastasis in lymph nodes evaluated using a green fluorescent protein-tagged human gastric cancer cell line. *Clinical Cancer Research*. 2006; 12(2): 361-368.

## **Chapter 3.0: High-Frequency (40 MHz) Ultrasound Imaging of the Development of Experimental Lymph Node Metastases**

### **3.1 Introduction**

Evaluation of lymph node status and removal of metastatic lymph nodes has been part of standard care for cancer patients. When metastatic tumour cells escape into the lymphatic vasculature, they eventually drain into the first lymph node, termed *sentinel node*, of the regional drainage basin (Cabanas, 1977). From the sentinel node, tumour cells can disseminate and establish metastases in several lymph nodes in the drainage basin. Considering the sequence of these events, biopsy of the sentinel nodal provides a good indicator of the nodal status of downstream regional lymph nodes (Morton et al, 1992). The assessment of nodal status is of particular clinical importance since degree of nodal involvement foretells the statistical probability of future or current risk of systemic metastases to distant organs (Cady et al., 2007). In an effort to discover new avenues of anti-metastatic therapeutic intervention, the pathological processes that drive lymphatic metastasis are an area of intense research in preclinical studies (for review, see Mumprecht and Detmar, 2009).

To study the stages of lymph node metastasis progression in mice, I have recently developed a novel animal model termed *lymph node experimental metastasis assay* (LEMA; see Chapter 2.0). This previous study demonstrated, through progressive time end-point experiments, that LEMA reliably recapitulates

the progressive stages of metastasis development, from: 1) the arrest of tumour cells, 2) growth into micrometastasis, 3) and formation of overt lymph node metastases. Moreover, adapting a “cell accounting” technique previously developed for quantifying steps in hematogenous metastasis (Luzzi et al., 1998; Cameron et al., 2000), we were able to demonstrate how the formation of lymph node metastases is an inefficient process. We found that only 0.08% of tumour cells that arrive in the axillary lymph node were successful in forming overt metastases. However, one caveat of histological studies that examine disease progression is that they produce static “snap shots” of a pathologic process that is dynamic in nature. For example, Holmgren and colleagues (1995) demonstrated that the growth of micrometastases in lung is in a state of flux that is largely influenced by the rate of cell proliferation and rate of cell apoptosis. Thus once we observe a histological “snap-shot” of a metastatic deposit, it is not readily apparent whether the lesion would continue to grow into a lymph node tumour or spontaneously regress. To address this limitation, the current research uses non-invasive three-dimensional high frequency ultrasound (3D HFUS) imaging to longitudinally study the dynamic growth of individual lymph node metastases.

When compared to other imaging modalities such as magnetic resonance imaging, x-ray computed tomography, and positron emission tomography, ultrasound is the most prevalent diagnostic imaging modality used in the United States (Szabo, 2004). The frequency of clinical ultrasound scanners ranges from

1 – 15 MHz and spatial resolution ranges from 3 mm to 0.5 mm, accordingly. HFUS ranges from 20-100 MHz, and can resolve structures on the micrometer scale; however, there is a trade-off since depth penetration of the ultrasound waves into the tissue is diminished due to frequency-dependent attenuation (Vogt et al., 2010). Thus HFUS largely has been used in near-surface clinical applications (imaging skin & superficial lymph nodes), and small animal imaging. With respect to small animal imaging cancer research, HFUS has proven to be a useful tool in studying orthotopic tumour growth (Cheung et al., 2005), the development of liver metastases (Graham et al., 2005), and assessing the efficacy of targeted therapies against tumour vasculature (Franco et al., 2006). In regards to lymph node imaging, several groups have used high frequency ultrasound in monitoring lymph node size in pathological conditions such as autoimmune lymphoproliferative disease (Teachey et al, 2008) and lymph node hyperplasia (Bosisio et al, 2009). The latter study is of particular interest because the authors demonstrated the reliability of HFUS in serially imaging lymph nodes as small as  $0.1 \text{ mm}^3$  and reported that error measurements accounted for 6.7% of variability when measuring small lymph nodes.

The present research demonstrates the utility of 3D HFUS (40 MHz) in serially imaging the development of lymph node metastases in mice. Specifically, I demonstrate how ultrasound parameters such as volume, roundness index, B-mode brightness, and percent vascularity can be used to characterize the progression of lymph node metastasis development. In addition, we report the



sensitivity and specificity of these parameters in differentiating metastatic lymph nodes from non tumour-bearing lymph. The most important finding of this study is the ability of HFUS to detect small non-palpable metastatic deposits ranging from 1.2 to 4.4 mm in diameter without the use of contrast agents or cell labels. The size range of small metastatic deposits detected in this study is smaller than the clinical limit of detection which ranges from 4.5 - 5 mm in diameter (Starritt et al, 2005; Sibon et al, 2007). This suggests that ultrasound scanning at higher frequencies maybe more sensitive in detecting smaller metastases compared to scanning at lower ultrasound frequency. The small metastatic deposits observed in this study appeared as distinct hyperechoic regions which permitted image segmentation and the acquisition of volumetric data over successive time points. From these findings, we conclude that HFUS is a cost-effective and time-efficient imaging modality well suited for longitudinal study of lymph node micrometastases mice.

## **3.2 Materials and Methods**

### **3.2.1 Cell culture**

B16F10-LacZ murine melanoma cells (Kirstein et al, 2009) were maintained in  $\alpha$ -MEM containing 10% fetal bovine serum at 37°C and 5% CO<sub>2</sub>. Cells were then trypsinized with 0.25% trypsin and 1mM EDTA, centrifuged at 800 rpm for 5 minutes, then resuspended in HBSS. The cell pellet was washed twice in HBSS prior to performing a trypan blue exclusion assay to test cell viability. Cell viability was between 95-99%. From these cells, a working cell suspension containing  $1.5 \times 10^7$  B16F10-lacZ cells in a volume of 1mL was prepared for intranodal (inguinal) injection. A volume of 200 $\mu$ L containing  $3 \times 10^6$  cells were injected into each mouse.

### **3.2.2 Animal model and surgical technique**

Surgical procedures for LEMA are described in more detail in Chapter 2. The current study used LEMA to induce tumour growth in axillary lymph nodes, however, tumour cells were not labeled with 3  $\mu$ m beads nor co-injected with 16  $\mu$ m reference beads. Described briefly, female C57Bl/6 mice (Harlan Sprague Dawley, Indianapolis, IN), 5 weeks of age, were cared for in accordance with standards of the Canadian Council on Animal Care, under an approved protocol of the University of Western Ontario Council on Animal Care. Surgery was performed on mice under gas anesthesia (1.5% isoflurane in O<sub>2</sub>) on a water-heated stage. Under aseptic conditions, the right inguinal lymph node was

slowly injected with 200  $\mu\text{L}$  of a suspension containing  $3 \times 10^6$  B16F10-LacZ cells (see Figure 3.1 A). During the injection, the cell suspension could be seen leaving the inguinal lymph node via the efferent lymphatic duct when observed under a dissection microscope. After injection, the inguinal lymph node was surgically removed to prevent early onset of morbidity due to rapid tumour growth in the inguinal lymph node (see Figure 3.1 B). The surgical wound was closed with stainless steel staples, and mice were injected with Metacam (0.1mg/kg; Boehringer Ingelheim Vetmedica Inc, St. Joseph, Missouri) and allowed to recover. From previous experiments using this model, after 14 days post-injection, palpable axillary lymph node metastases form in 70-90% of the mice (see Figure 3.1 C).

A separate group of aged-matched mice ( $n = 3$ ) served as a control group where mice underwent the same surgical procedures as outlined above, except saline was injected in the inguinal lymph node rather than tumour cells. This was done to determine whether tissue damage from the surgical procedure affected the downstream axillary lymph node.

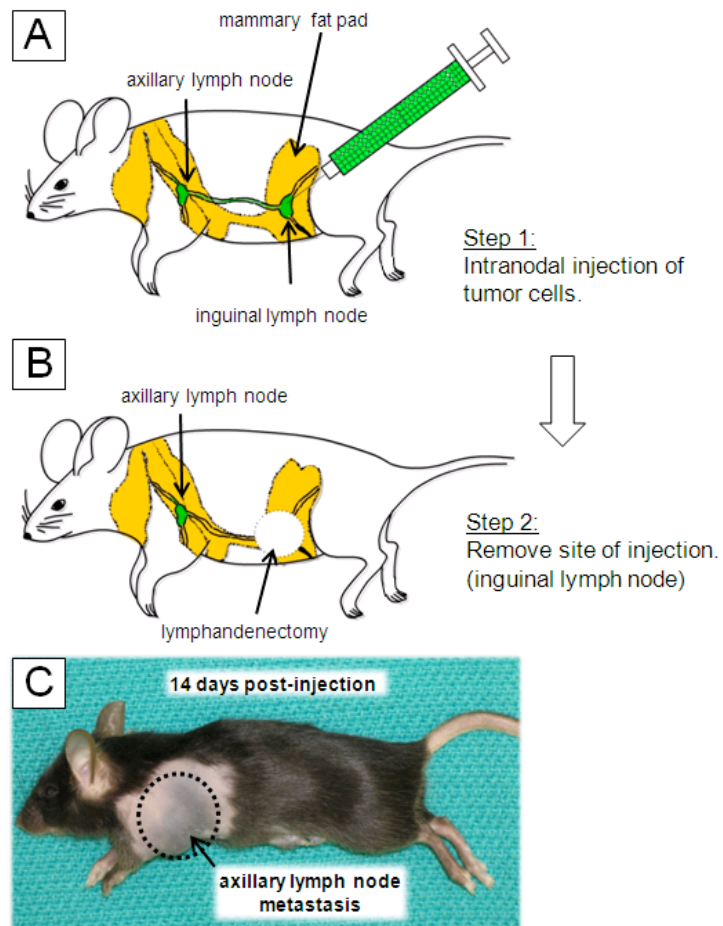


**Figure 3.1 A novel animal model recapitulating lymph node metastasis.**

To experimentally induce the formation of lymph node metastases, tumour cells were introduced directly into the lymphatic vasculature via an intranodal injection of tumour cells in the inguinal lymph node (panel A). Morbidity from tumour growth at the injection site was prevented by surgical removal of the inguinal lymph node (panel B). After 14 weeks post-injection, axillary lymph node metastases formed (panel C).

### 3.2.3 Ultrasound B-mode & power Doppler imaging

To non-invasively monitor the changes in lymph node volume, roundness index (RI), B-mode image brightness (grey value), and vascular volume fraction from power Doppler ultrasound during the development of lymph node metastases, the Vevo 2100 high-frequency ultrasound imaging system (VisualSonics Inc., Toronto, Ontario, Canada) was used. The Vevo 2100 is the linear array system described by Foster *et al* (2009). The Vevo 2100 ultrasound probe used in this study (MS-550D) has a 40-MHz center frequency with a 7-mm focal depth. The nominal in-plane spatial resolution at the focus is 40  $\mu\text{m}$  (axial) x 80  $\mu\text{m}$  (lateral). Imaging of mice was similar to the methods described by Graham *et al.* (2005). Briefly, the shoulder area nearest to the axillary lymph node was depilated with commercial Nair<sup>TM</sup> hair removal cream. During imaging, the mouse was positioned on its side and was kept under anesthesia with 1.5% isoflurane on a heated stage. Two-dimensional (2D) images of the lymph node were acquired in the sagittal plane after ultrasound contact gel was applied to the depilated shoulder area. For three-dimensional (3D) imaging, parallel 2D images were obtained by mounting the transducer on a computer-controlled linear motor that was programmed to acquire images at 30- $\mu\text{m}$  intervals along the length of the lymph node. All mice were imaged every second day until 14 days post-injection (Figure 3.2), a time point at which 70%-90% of mice typically developed lymph node metastases (Chapter 2).

Ultrasound volume measurements were obtained as described by Tong et al (1998). Briefly, the boundaries of lymph nodes or hyperechoic regions were manually segmented within parallel planes separated by 300  $\mu\text{m}$ . The total volume of the object of interest was calculated by summing the outlined areas and multiplying the inter-slice distance.

Three-dimensional power Doppler imaging was used to measure changes in percent vascularity of lymph nodes during the development of metastases. Percent vascularity is the percentage of pixels within the ultrasound volume in which blood flow was detected by the power Doppler system. The acquisition settings for power Doppler were 10 x 14  $\text{mm}^2$  field of view, frequency 32MHz, 100% transmit power, 30 dB receiver gain, wall filter at maximum, and 4 kHz pulse repetition frequency. These settings were selected to image normal lymph node vascularity in non-tumour bearing mice. Power Doppler imaging was immediately performed after each B-mode imaging scan, as described above. In total, B-mode and power Doppler imaging took approximately 8 minutes to complete per mouse.

To obtain measurements of percent vascularity, the boundaries of lymph node tumours were manually segmented within parallel planes separated by 300  $\mu\text{m}$ . The percent vascularity represents the percentage of the pixels within the region of interest (ROI) which have a power Doppler signal associated with them.

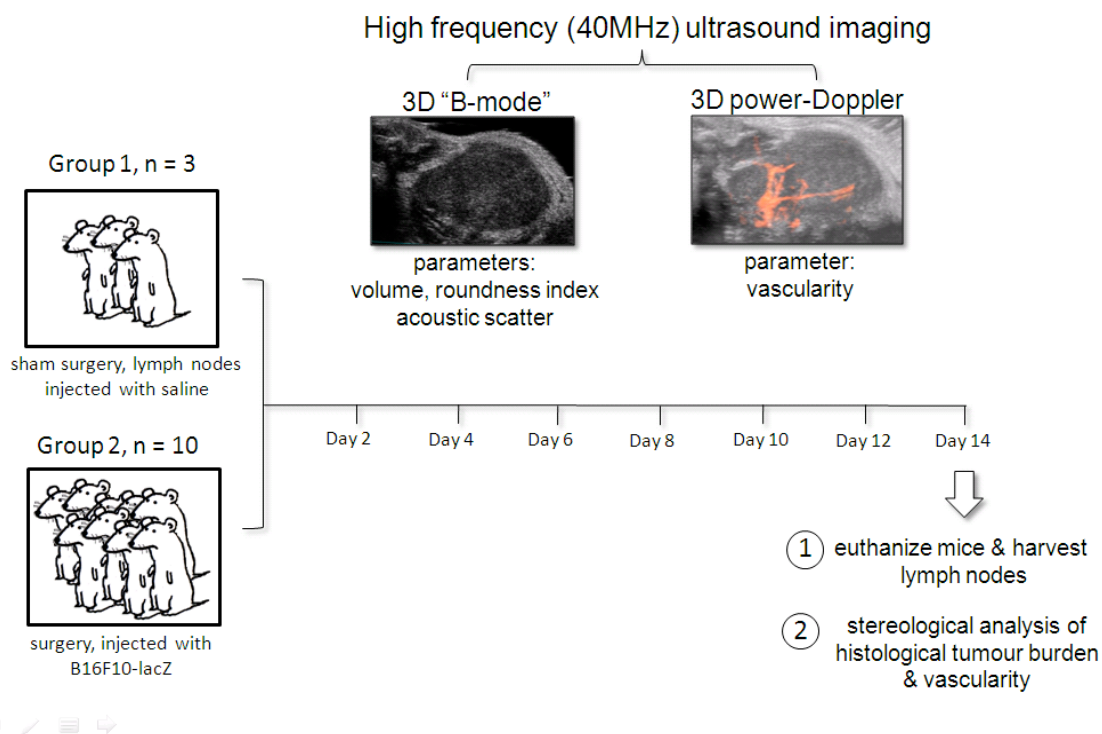


**Figure 3.2 Imaging protocol to longitudinally study the progression of lymph node metastasis.** Mice that have received an injection of tumour cells were monitored every 2nd day for 14 days. B-mode ultrasound and 3D power-Doppler imaging were performed to measure changes in lymph node volume, roundness index, B-mode image brightness, and lymph node vascularity. Control mice were subject to sham surgery and saline injection to determine if the changes in ultrasonic parameters were specific to the presence of growing metastases. At the end point, mice were euthanized and lymph nodes harvested and stained for lacZ and H&E for morphometric analysis.

### 3.2.4 Ultrasound Imaging Analysis

Lymph node images were manually segmented in parallel planes at 300  $\mu\text{m}$  intervals through the 3D ultrasound images and lymph node volumes were estimated as described in Graham et al. (2005). For lymph nodes with distinct hyperechoic regions, subvolumes of these brighter regions were analyzed in the same manner.

The roundness index (RI) of the lymph node, defined as the ratio of the longest axis to the shortest axis of the lymph node (Vassallo *et al.*, 1993), was measured in 2D images of lymph nodes. Five images were obtained from each lymph node at all time points and exported into the ImageJ software package (Abramoff et al, 2004) for analysis. In ImageJ, lymph nodes were segmented and the RI was manually calculated. The five RI measurements were averaged for each lymph node.

To assess differences in B-mode image brightness (grey scale value) between lymph nodes negative for metastases (as assessed by histology) and lymph node metastases and regions suspected of being metastatic tissue, five 2D images of lymph nodes were imported into ImageJ. The images were stored using a logarithmically compressed grey scale with 256 grey levels and a 65-dB dynamic range. Three circular regions of interest (ROIs), with a diameter of 0.3 mm, were uniformly spaced along the length of the lymph node and the mean grey pixel value from all the pixels within the ROI was calculated. The 15 grey



values from the 5 images analysed were averaged for each lymph node. In cases where lymph nodes had hyperechoic regions suspected of being small metastatic deposits, a sub-region analysis was performed where mean grey values sampled from hyperechoic were compared to mean grey values obtained from regions of the lymph node that appeared normal. Sub-region comparison analysis was performed on three lymph nodes that harboured distinct hyperechoic sub-regions.

### **3.2.5 Assessing sensitivity and specificity of ultrasound parameters in detecting lymph node metastases**

To assess how well the above ultrasound parameters can accurately detect the presence of lymph node metastases when compared to the “gold standard” of histological evaluation by a pathologist, the sensitivity and the specificity of each parameter was calculated. In the context of this study, sensitivity refers to the proportion of mice with actual lymph node metastases and considered positive by ultrasound. Specificity refers to the proportion of mice without lymph node metastases and considered negative by ultrasound (Florkowski, 2008). For each ultrasound parameter, raw values were arranged from lowest to highest, and a threshold value was applied as a “cut-off” point that differentiated lymph nodes that were negative for metastases and lymph nodes that harboured metastases. For example, Vassallo and colleagues (1993) considered lymph nodes with a small RI value ( $< 2$ ) to be positive for metastasis. Therefore when the range of values within the negative lymph node group was

examined, the smallest RI value was 3.4. This value is then considered the threshold value where any lower RI value would be considered “positive” for metastasis, whereas any value higher than the threshold value would be considered “negative”. When comparing the number of “negative” and “positive” lymph nodes by ultrasound evaluation to the actual number of true negatives and positives by the “gold standard” of histological assessment, *sensitivity* and *specificity* values can be calculated from the following equations:

Sensitivity = True Positive Fraction (TPF)

$$\text{TPF} = \frac{\text{Correct positive diagnosis}}{\text{Actual number of positive cases}}$$

Specificity = 1 - False Positive Fraction (FPF)

$$\text{FPF} = \frac{\text{Incorrect positive diagnosis}}{\text{Actual number of negative cases}}$$

TPF and FPF values were calculated using cut-off values for volume, roundness index, B-mode brightness, and percent vascularity. The cut-off values were chosen based on the range of values observed in negative lymph nodes. The resulting sensitivity and specificity values for each parameter were tabulated.

### 3.2.6 Lymph node staining and histology

Fourteen days after injection, all animals were sacrificed after final imaging and whole axillary lymph nodes were harvested and placed in ice-cold phosphate buffer (0.1 M sodium phosphate monobasic, 0.1 M sodium phosphate dibasic, pH 7.3) until the organs from all mice were collected. Organs were subsequently stained with X-gal (Bioshop, Burlington, Canada) solution as described by Goring *et al.*, (1987) to visualize LacZ-expressing cells. X-gal stained lymph nodes were imaged in whole mount using a SteREO Lumar (Zeiss Canada) dissection scope attached to a digital camera (Canon). For histologic examination, fixed organs were paraffin-embedded for routine histological sectioning (thickness, 5  $\mu\text{m}$ ) and staining with hematoxylin and eosin (H&E).

### 3.2.7 Histological and stereological analysis

To acquire an estimate of histological tumour burden, a point count ( $P_P$ ) method described by Underwood (1970) was used to calculate the fractional area of the lymph node section containing tumour tissue. Using ImageJ analysis software, a point grid consisting of  $0.01\mu\text{m}^2$  squares was superimposed onto digital images of H&E stained lymph node sections. The point estimate ( $P_P$ ) was calculated by determining the number of points falling on tumour tissue divided by the total number of points falling on the lymph node.  $P_P$  was calculated for 3 sections per lymph node to obtain a mean per mouse.

### 3.2.8 Statistical analysis

Statistical analysis was performed using Microsoft Excel 2007 (Microsoft Corporation, Redmond, Washington) and GraphPad Prism version 4.0 (GraphPad Software Inc., San Diego, California) for Windows XP. Prior to performing statistical analyses on means, data were tested for normality. When data were normally distributed, means that were measured over time were compared by parametric repeated measures analysis of variance (ANOVA), and post-hoc Tukey's multiple comparisons test was performed to determine which means were significantly different. When data were not normally distributed, means that were measured over time were compared by non-parametric repeated measures Friedman's test, and post-hoc analysis using Dunn's multiple comparisons test.

To compare ultrasound volume measurements of metastatic tissue in lymph nodes to histological area measurements, a correlation coefficient ( $r^2$ ) value was generated using a linear regression model to determine if a positive correlation existed between the two parameters.

### **3.3 Results**

#### **3.3.1 Lymph node experimental metastasis assay**

LEMA is a new animal model that recapitulates the stages of metastasis development in the lymph node. In this assay, axillary lymph node metastases are formed by the direct introduction of tumour cells into the lymphatic vasculature via intranodal injection into the inguinal lymph node. Prior to injection of tumour cells, mice were scanned by ultrasound for baseline measurements of lymph node volume, roundness index, B-mode brightness, and percent vascularity. The incidence of metastases 14 days after injection is shown in Table 3.1, as assessed by histopathology.

Table 3.1 Metastasis incidence from experimental lymph node metastasis assay

Time elapsed post-injection	Negative*		Positive*	
	Incidence	Micrometastases <sup>1</sup>	Overt metastases <sup>2</sup>	
		Incidence	Incidence	Incidence
14 days	2/10	1/10	7/10	

\*Pathological findings by standard H&E staining, results confirmed by pathologist (ABT).

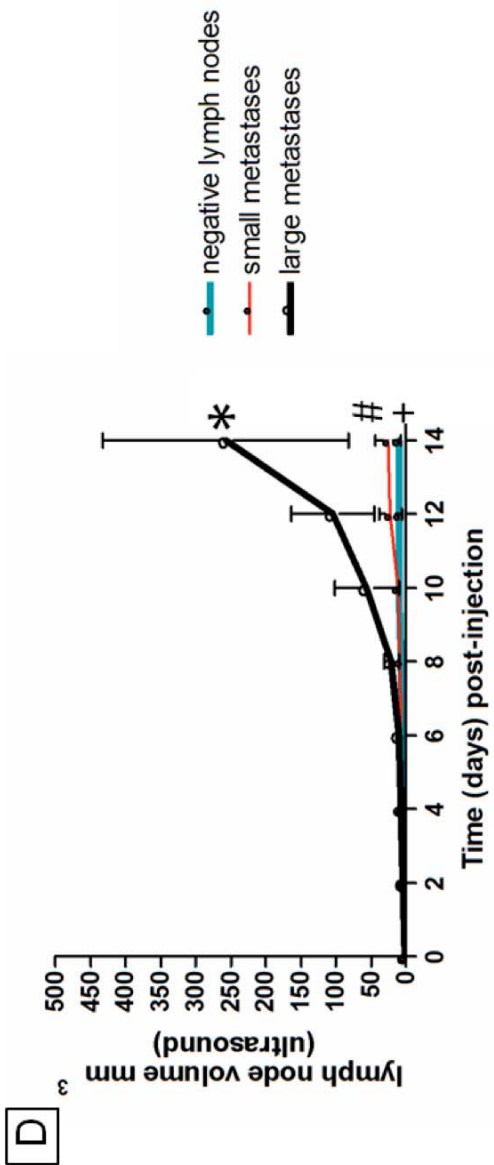
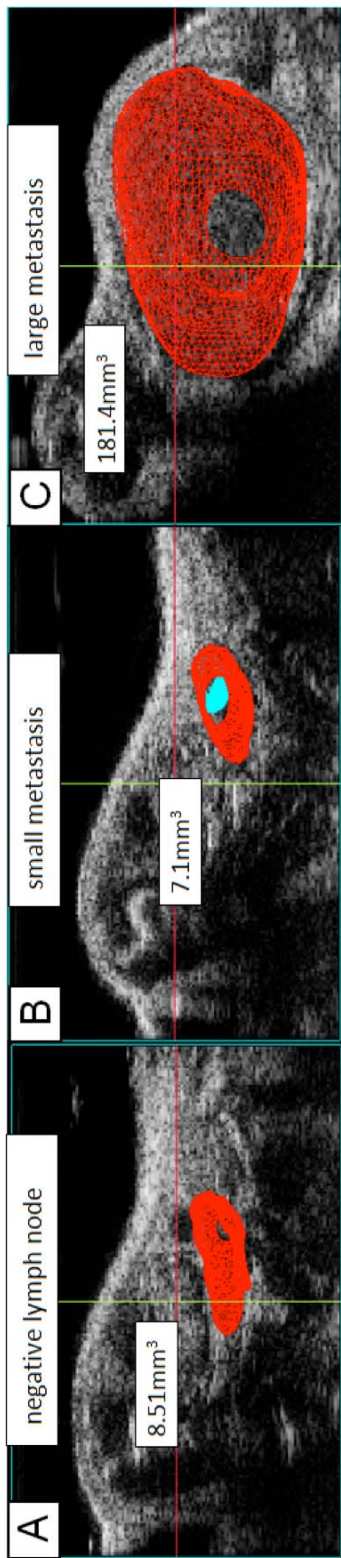
<sup>1</sup>Multicellular tumor foci between 0.2mm and 2mm in diameter, <sup>2</sup>Metastatic deposits larger than 2mm, 6<sup>th</sup> ed. AJCC Staging Manual (Green *et al.*, 2002).

### **3.3.2 Changes in lymph node volume during the development of metastases**

High-frequency ultrasound was used to non-invasively monitor the changes in lymph node volume during the stages of early seeding, formation of micrometastases, and the development of overt tumours. Mice were divided into distinct groups based on their histological characterization at end point: 1) negative lymph nodes with no metastases (see Figure 3.3 A); 2) lymph nodes that harboured small metastases but normal parenchyma tissue was still apparent (Figure 3.3 B); and 3) large metastases where the lymph node was completely replaced by metastatic tissue (Figure 3.3 C). Statistical analysis of these three groups reveals significant changes in lymph node volume over time as measured by ultrasound. Large lymph node metastases exhibited the greatest increase in volume over time. Interestingly, when comparing the median volumes of the three groups at 14 days, negative lymph nodes were not statistically different from those harbouring small metastases (see Figure 3.3 D legend).

**Figure 3.3 Ultrasound analysis of lymph node volume during the development of metastases.** Panels A, B, and C provide examples of a lymph node negative for metastases (assessed by histology), a lymph node with a small metastasis (white dashed box), and a large lymph node metastasis, respectively. Volumes are indicated in each panel. In panel D, longitudinal measurements of lymph node volume are shown for the three groups of lymph nodes. Means  $\pm$  standard deviations are graphed. All groups significantly changed in volume over time (\*,+ repeated measures ANOVA,  $p < 0.0001$ ,  $n = 5$ ; # Friedman test,  $p < 0.01$ ,  $n = 3$ ). At end point, comparison of the three groups (Kruskal-Wallis,  $p < 0.05$ ) showed no difference between negative lymph nodes and small metastases (post-hoc Dunn's multiple comparisons test,  $p > 0.05$ ). In contrast, large metastases were significantly different from negative lymph nodes (post-hoc Dunn's multiple comparisons test,  $p < 0.01$ ).

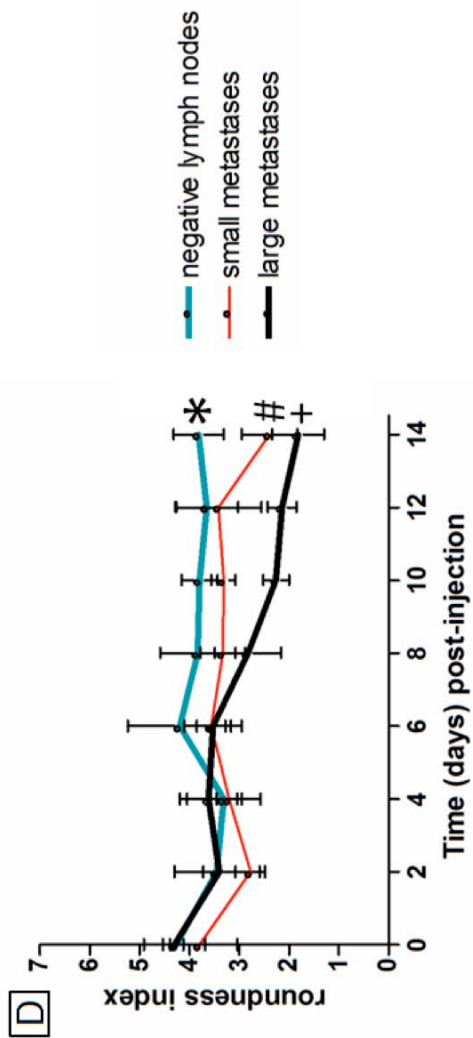
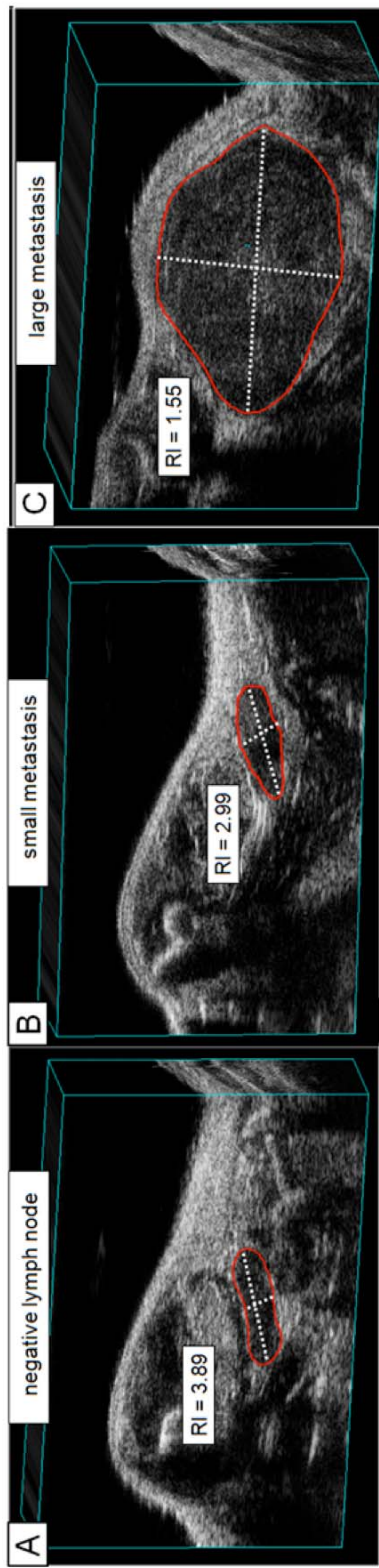




### **3.3.3 Changes in lymph node roundness index during the development of metastases**

Representative examples of lymph nodes with RI values from each group of mice are shown in Figure 3.4 A, B, and C. Negative lymph nodes had high RI values (greater than 3.4) which are characteristic of normal flat, prolate spheroid-shaped lymph nodes (Figure 3.4 A). The growth of small metastatic deposits increased the vertical height of lymph nodes, resulting in a lower RI value (less than 3.4; Figure 3.4 B). In large metastases, tumour growth resulted in a rounder shape (low RI value; Figure 3.4 C). Longitudinal RI measurements of the three groups of lymph nodes are shown in Figure 3.4 D. Repeated measures ANOVA of RI values reveal negative lymph nodes and lymph nodes with small metastases showed no significant change in RI over time. In contrast, lymph nodes that developed large metastases significantly became rounder over time (therefore decreasing RI value). At the end point, median RI values of negative lymph nodes, small metastases, and large metastases were found to be significantly different from each other (non-parametric ANOVA (Krusal-Wallis). Negative lymph nodes and lymph nodes with large metastases were found to be significantly different from each other, whereas median RI value of lymph nodes with small metastases did not significantly differ from either group.

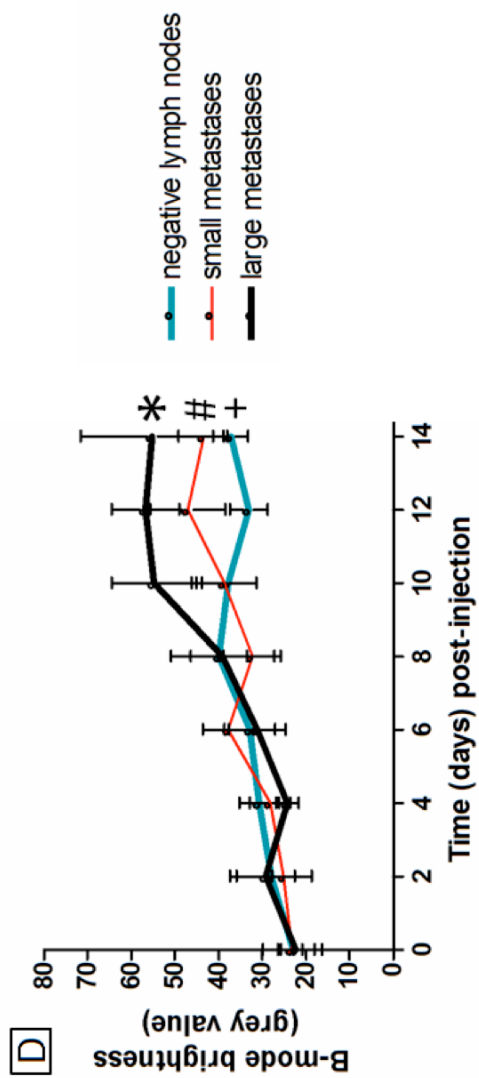
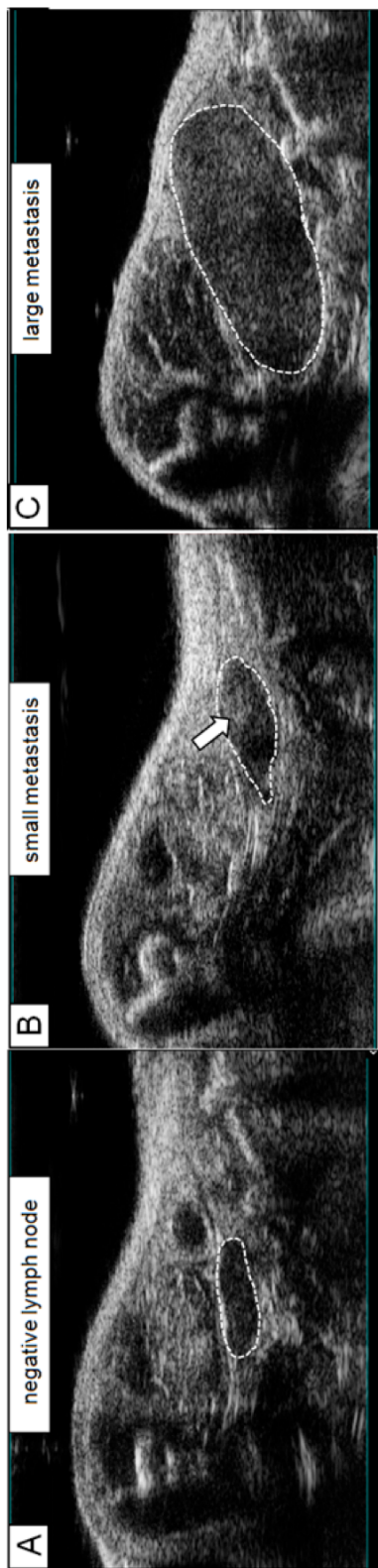
**Figure 3.4 Ultrasound analysis of lymph node roundness index during the development of metastases.** Panels A, B, and C provide examples of a negative lymph node, a lymph node with a small metastasis, and a large lymph node metastasis, respectively. RI values are shown for each lymph node. In panel D, longitudinal measurements of lymph node RI values are shown for the three groups. Means  $\pm$  standard deviations are shown. Both negative lymph nodes (\*) and small metastases (#) showed no significant change in RI over time, repeated measures ANOVA ( $p > 0.05$ ,  $n = 5$ ) and Friedman test ( $p > 0.05$ ,  $n = 3$ ), respectively. Large metastases (+) did show a significant change in RI over time (repeated measures ANOVA,  $p < 0.0001$ ,  $n = 5$ ). At end point, the median RI values of all groups were compared (Kruskal-Wallis,  $p < 0.01$ ). There were significant differences between the three groups, where negative lymph nodes and large metastases were significantly different from each other (Dunn's multiple comparisons test,  $p < 0.01$ ). The median RI value of lymph nodes did not significantly vary from both negative lymph nodes and lymph nodes with large metastases.



### **3.3.4 Changes in lymph node B-mode brightness during the development of metastases**

The B-mode brightness of lymph nodes was measured over time to determine if differences exist between negative and metastatic lymph nodes. Representative examples of a negative lymph node, a lymph node with a small metastasis, and an overt lymph node metastasis are shown in Figure 3.5 A, B and C. Negative lymph nodes typically appeared hypoechoic (darker) than the surrounding adipose tissue. Lymph nodes with small metastatic deposits showed distinct sub-regions that appear hyperechoic (brighter) compared to adjacent lymph node parenchyma; see Figure 3.5 B, and Figure 3.6 A, D, G and J for examples. Large lymph node metastases were more hyperechoic compared to normal lymph nodes. Longitudinal assessment of B-mode brightness in the three groups of lymph nodes is shown in Figure 3.5 D. Mean pixel brightness sampled from negative lymph nodes showed significant changes over time, however there were no time points that were significantly different from each other. In contrast, lymph nodes with small metastases, and lymph nodes that developed into large metastases, did show significant increases in B-mode brightness over time. At end point, the B-mode brightness of overt lymph node metastases was significantly higher than negative lymph nodes (see Figure 3.6 B).

**Figure 3.5 Ultrasound analysis of lymph node B-mode brightness during the development of metastases.** Panels A, B, and C exhibit the echogenic properties of a negative lymph node, a lymph node with a small metastasis, and a large lymph node metastasis, respectively. In panel D, longitudinal measurements of lymph node B-mode brightness are shown for all three groups of lymph nodes, means  $\pm$  standard deviations are shown. All groups showed significant changes over time (\*, + repeated measures ANOVA,  $p < 0.05$ ; # Friedman test  $p < 0.05$ ). At later time points, large lymph node metastases showed grey values that were significantly higher than lymph nodes at pre-injection time point (10-14 days compared to day 0;  $p < 0.001$ ; Tukey's multiple comparisons test). At end point, B-mode brightness was significantly higher than negative lymph nodes (un-paired t test,  $p < 0.01$ ).



### **3.3.5 Intranodal hyperechoic regions in lymph nodes correspond to small metastatic deposits**

At the end point, there were three lymph nodes that harboured small metastatic deposits while retaining areas of normal lymph node organ structure (Figure 3.6 panels C,F,I,L). Corresponding 2D ultrasound images exhibited distinct hyperechoic regions (Figure 3.6 panels A,D,G,J) that appeared to correspond to the metastatic deposits. These regions were not found in normal lymph nodes. A sub-region B-mode brightness analysis of these 2D images was performed in ImageJ to determine if these hyperechoic regions were significantly brighter than surrounding areas within the same lymph node. In all three lymph nodes, these hyperechoic regions were significantly brighter than the surrounding tissue (Figure 3.6 panels E,H,K). With respect to the ultrasound images in Figure 3.6 E, H, K, manual measurements of the corresponding metastatic deposits in stained whole-mount lymph nodes were 1.5 mm (micrometastasis), 2.6 mm, and 3.8 mm at their widest diameter, respectively.

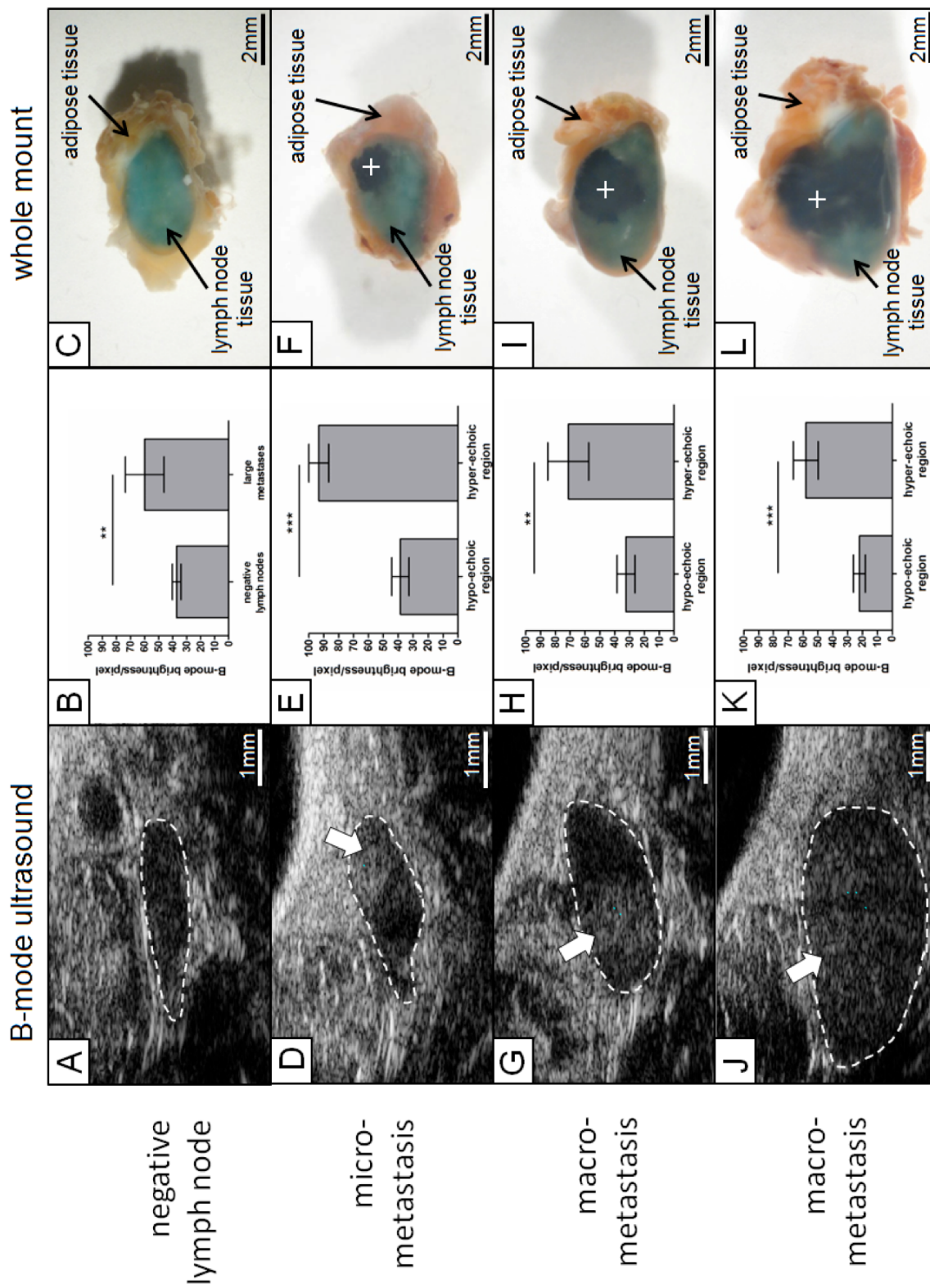
### **3.3.6 A positive correlation between ultrasound volumetric and histological area measurements**

When comparing the volume fraction of these hyperechoic regions and the area fraction of the metastatic deposit in histological sections, in addition to data from lymph nodes with large metastases, there was a strong positive correlation



( $r^2 = 0.94$ ) between ultrasound volumes and histological area measurements (Figure 3.7 C).

**Figure 3.6 Hyperechoic subregions of the lymph node corresponding to micro- and macrometastatic deposits.** B-mode ultrasound images of axillary lymph nodes are shown in panels A, D, G, J. An example of a negative lymph node is shown in panel A. Axillary lymph nodes shown in D, G, J containing hyperechoic subregions (dashed outlines). Scalebar =1 mm. In panel B, the mean B-mode brightness of negative lymph nodes (n = 5 lymph nodes) and lymph nodes with large metastases (n = 5 lymph nodes) were found to be significantly different (un-paired-t test,  $p < 0.01$ ). Intranodal subregion analyses were performed on B-mode images of the lymph nodes with small metastases shown in D, G, J. Hyperechoic (arrow) and hypoechoic regions within lymph nodes with small metastases were significantly different in mean B-mode brightness (n = 5 ROIs per subregion, paired t-test, \*\*  $p < 0.01$ ; \*\*\*  $p < 0.001$ ). Images of lymph node whole mounts corresponding to each ultrasound image are shown in panels C,F, I, L (metastatic deposits shown by +). Scalebar = 2 mm for whole mount images.



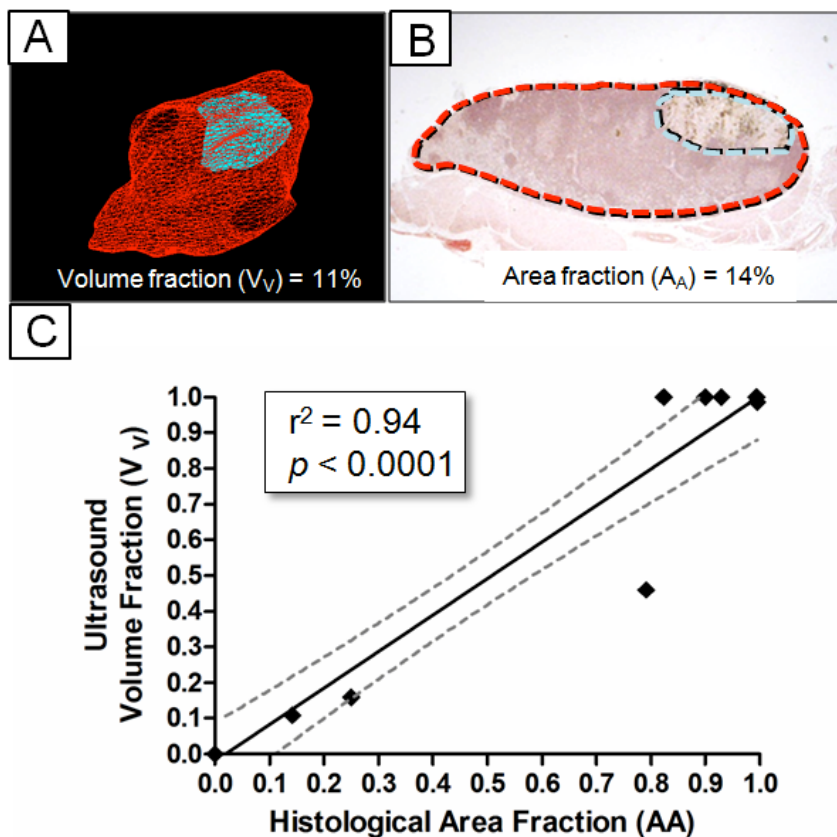


**Figure 3.7 Strong positive correlation between ultrasound volumetric and histological area measurements.** Examples of ultrasound volume fraction and histological area fraction of tumour-burden are shown in panel A and B, respectively. Panel A displays a volumetric rendering from B-mode ultrasound images of the lymph node (red) and the micrometastasis within (light blue). The corresponding histology section in panel B outlines the lymph node (red) and the micrometastasis (light blue). In panel C, ultrasound measurements of tumour volume fractions and histological tumour area fraction were compared by linear regression analysis ( $r^2 = 0.94$ ,  $p < 0.0001$ ,  $n = 13$ ). Dashed lines represent the 95% confidence interval.

### **3.3.7 Longitudinal imaging of micrometastatic deposits and small metastases**

B-mode images of lymph nodes with small non-palpable metastases and micromematastatic deposits had hyperechoic subregions that were conspicuous enough to outline and make volumetric measurements. This was done over several time points. Figure 3.8 demonstrates the volume changes of these hyperechoic regions over time. The variability in growth rates among the small metastatic deposits is apparent: mouse #9 showed the largest increase in volume in 6 days, mouse #4 only slightly increased during that time, and mouse #12, did not appear to change in volume in 6 days. This suggests the micrometastatic deposit in mouse #12 was in a state of dormancy.

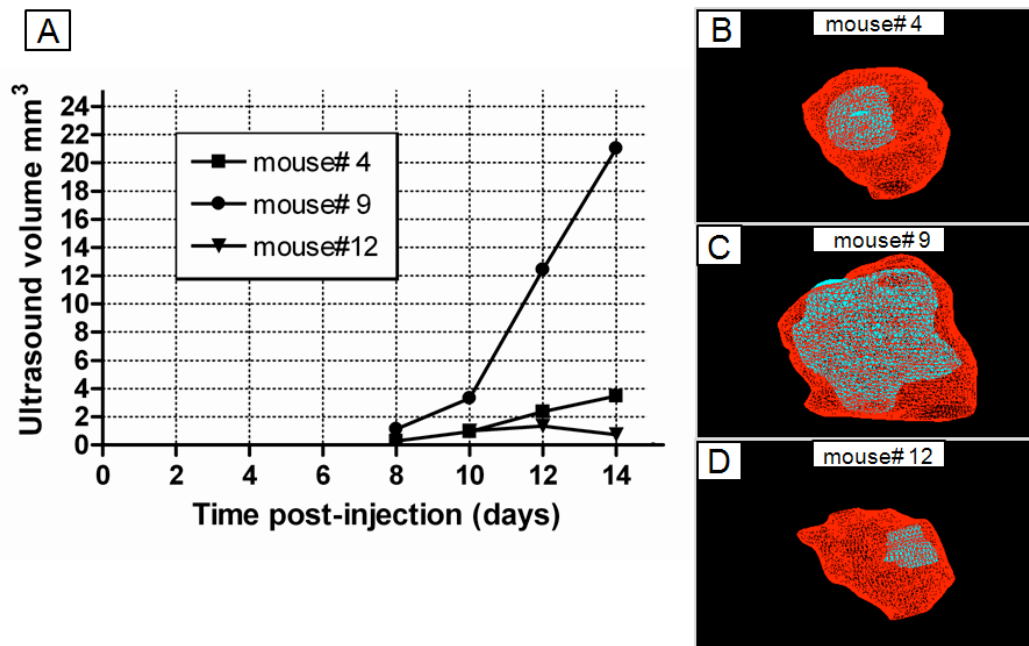
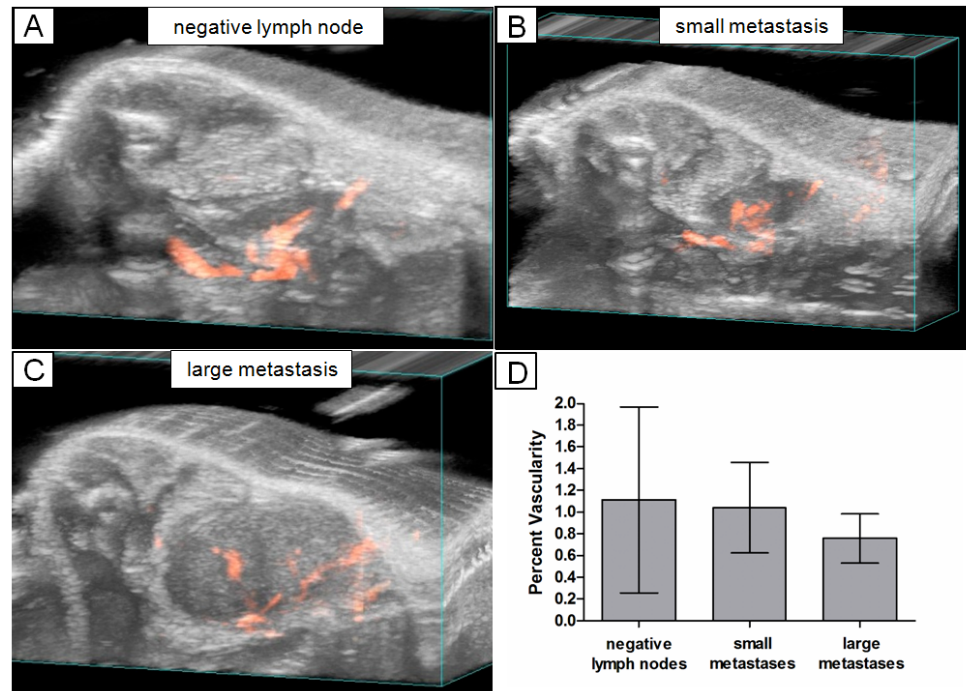


**Figure 3.8 Growth of small non-palpable metastatic deposits in lymph nodes.** Distinct hyperechoic regions of lymph nodes with small metastases became apparent in mouse #4 and #9 at eight weeks post-injection, and mouse #12 developed a hyperechoic region ten weeks post-injection. In panel A, mouse#9 showed a hyperechoic region with a higher rate of volume increase than the remaining two lymph nodes. In contrast, the axillary lymph node of mouse#12 had a hyperechoic region that appeared to increase in size from day 8 to 12, after which a decrease in volume was observed. In panels B, C, and D, volumetric renderings of the lymph nodes (red) and their metastatic deposits (light blue) are shown at 14 days post-injection.

### **3.3.8 Lymph node percent vascularity of negative lymph nodes and metastatic lymph nodes.**

3D power Doppler was used to assess whether there were differences in percent vascularity (PV) between negative lymph nodes and metastatic lymph nodes (shown in Figure 3.9 panels A and B). A group comparison performed at the 14 day end-point showed no significant differences between negative lymph nodes, lymph nodes with small metastases, and large overt metastases (shown in Figure 3.9 panel D). There was a non-significant decrease in mean PV values from negative lymph nodes, to small lymph node metastases, and overt lymph node metastases.



**3.9 Lymph node percent vascularity of negative lymph nodes and metastatic lymph nodes.** Panels A displays a 3D rendering of a negative lymph node and associated vasculature (shown in red). Panel B depicts a lymph node with a small metastasis, and panel C, an example of a large lymph node metastasis. In panel D, mean PV values of all three groups of lymph nodes at 14 days are shown (means  $\pm$  standard deviations). Comparison all three groups show no significant differences in percent vascularity (Kruskal-Wallis,  $p > 0.05$ ).



### **3.3.9 The sensitivity and specificity of ultrasound parameters in detecting lymph node metastases**

Ultrasound volume was found to have a sensitivity of 88% and a specificity of 100% in detecting lymph node metastases when using a cut-off value of 20 mm<sup>3</sup> (Table 3.2). One caveat in using this threshold value, however, is the instance where a lymph node harbouring a micrometastatic deposit (volume 8.7 mm<sup>3</sup>) yielded a false negative. This indicates that micrometastatic deposits may be present without significantly changing the volume of the lymph node.

The overall B-mode brightness of lymph node had a sensitivity of 75% and a specificity of 100% in detecting lymph node metastases. All negative lymph nodes have mean grey values lower than the cut-off value (grey value = 45). The sensitivity was diminished due to two lymph nodes with small metastases that also have overall mean grey values less than 45.

When one considers using decreased values of PV to detect the presence of lymph node metastases, PV has a sensitivity of 100% and a specificity of 60%. The lower specificity is due to two instances where negative lymph nodes had PV values less than 2 that resulted in two incorrect positive diagnoses.

RI is considered to be the most accurate parameter in detecting lymph node metastases. A cut-off value of 3 resulted in a sensitivity of 100% and specificity of 100% (Table 3.2). Furthermore, RI was sensitive in detecting lymph

nodes with small metastases including a lymph node harbouring a micrometastasis (example shown in Figure 3.4 B).

Table 3.2 Sensitivity and specificity of ultrasound parameters in detecting lymph node metastases

Ultrasound parameter	Sensitivity	Specificity
Lymph node volume	88%	100%
Roundness index	100%	100%
B-mode brightness	75%	100%
Percent vascularity	100%	60%

### 3.4 Discussion

The clinical impact of lymph node metastases on patient survival underscores the importance of developing preclinical models that recapitulate this pathological process. Each step of the metastatic cascade is potentially rate limiting (Chambers et al., 2002). Therefore, determining which step(s) of the metastatic cascade where metastasized cells are most amenable to intervention will lead to the development of novel anti-metastatic therapeutics. One innovative approach that has shed light on the metastatic process *in vivo* is the use of imaging modalities such as optical (Luzzi et al., 1998), high-frequency ultrasound (Graham et al., 2005), PET (Ren et al., 2009), and MRI (Heyn et al., 2006). High frequency ultrasound in particular, is an attractive option for imaging metastases due to its high resolution (50  $\mu\text{m}$ ), short scan times (in order of minutes), relative safety, and cost efficiency in obtaining longitudinal 3D information on soft tissues. In the current research, we present the first high frequency ultrasound study that characterizes the development of axillary lymph node metastasis in a syngeneic mouse model of melanoma.

As demonstrated by this report, high frequency ultrasound is well suited for longitudinal study of lymph node metastasis development. Longitudinal changes observed in parameters such as volume, RI, and B-mode brightness were sensitive in detecting lymph node metastases from non tumour-bearing lymph nodes. In particular, the roundness index was the parameter with both the highest sensitivity and specificity in differentiating overt and non-palpable lymph

node metastases (examples shown in 3.4 B,C) from negative lymph nodes. Specifically, when using a cut-off value of 3, RI was able to detect a lymph node with a micrometastatic deposit.

Another interesting finding in this study is the manner in which metastatic tissue appeared brighter than the normal lymph node tissue. The higher B-mode brightness of metastatic deposits is attributable to the larger amplitude of backscattered echoes returning to the transducer compared to the backscatter from normal lymph node parenchyma. The observation that metastatic deposits were hyperechoic was surprising since previous work by Graham and colleagues (2005) observed metastases to be hypoechoic (darker) compared to the normal liver parenchyma. A plausible explanation of the apparent discordant observations on the echogenicity of metastases is the difference in organ site (lymph node vs. liver). Since ultrasound contrast between two adjacent tissues is dependent on their difference in acoustic impedances, the surrounding parenchymal tissue may be a factor that contributes to the ultrasound contrast of metastases. Irrespective of the exact cause of higher B-mode brightness of lymph node metastases, we were able to exploit this phenomenon and track the growth of small metastatic deposits (Figure 3.8). Moreover, we were able to track a micrometastatic deposit over time (Figure 3.8 D); in this case, the micrometastasis did not seem to significantly change in volume over time. Dormancy in micrometastases is purported to be due to a balance of cell

proliferation and apoptosis, as seen previously observed by Holmgren and colleagues (1995).

In addition to B-mode derived parameters that describe the lymph node shape and echogenicity during the development of lymph node metastases, our study also assessed if there were metastasis-associated changes in lymph node vascularity via power Doppler imaging. At end-point, we did not see any significant differences in percent vascularity between negative lymph nodes, small and large lymph node metastases. Although there was a decreasing trend from negative lymph nodes to large lymph node metastases, the large variability within each group resulted in no significant difference.

To conclude, this is the first report to demonstrate the utility of 3D HFUS imaging in the non-invasive and longitudinal study of the development of lymph node metastases *in vivo*. More specifically, 3D HFUS imaging permits temporal sampling of parameters such lymph node volume, shape, and B-mode brightness during the growth of lymph node tumours in live mice. Furthermore, the current research reports the sensitivity of these parameters in differentiating metastatic lymph nodes from non-metastatic lymph nodes. The most striking finding of the current work is the ability to identify and longitudinally image micrometastatic deposits (as small as 1.2 mm in diameter) within the lymph node without the use of contrast agents or cell labels. The ability to longitudinally and non-invasively image both micrometastatic disease and overt lymph node tumours in the preclinical setting will provide researchers with a new tool to assess the efficacy

of novel anti-metastatic therapeutics. Lymph node ultrasound imaging can be used to ask: How do quickly vs. slowly growing metastases respond to chemotherapeutics? What is the duration of treatment that results in inhibition of metastasis growth, or maintenance of micrometastatic dormancy? Does reducing lymph node tumour burden decrease systemic metastatic disease? The answers to such questions will provide cancer researchers with new insight in the treatment of lymphatic metastatic disease.

### 3.5 References

- Abramoff MD, Magelhaes PJ, Ram SJ. Image Processing with ImageJ. *Biophotonics International*. 2004; 11: 36-42.
- Bosisio MR, Maisonneuve C, Gregoire S, et al. Ultrasound biomicroscopy: a powerful tool in probing murine lymph node size in vivo. *Ultrasound in Medicine and Biology*. 2009; 35: 1209-1215.
- Cabanas R. An approach for the treatment of penile cancer. *Cancer*. 1977; 39: 456-466.
- Cady B. Regional lymph node metastases, A singular manifestation of the process of clinical metastases in Cancer: Contemporary animal research and clinical reports suggest unifying concepts. In: Rosen ST (series ed.), Leong SPL (book ed.). *Cancer Treatment and Research: Cancer Metastasis and the Lymphovascular System, Basis for Rational Therapy*. New York, NY: Springer Science+Business Media, LCC; 2007:185-202.
- Cameron MD, Schmidt EE, Kerkvliet N, et al. Temporal progression of metastasis in lung: cell survival, dormancy, and local dependence of metastatic inefficiency. *Cancer Research*. 2000; 60:2541-2546.
- Chambers AF, Groom AC, MacDonald IC. Dissemination and growth of cancer cells in metastatic sites. *Nature Reviews Cancer*. 2002; 2:563-572.



- Cheung AM, Brown AS, Hastie LA, et al. Three-dimensional ultrasound biomicroscopy for xenograft growth analysis. *Ultrasound in Medicine and Biology*. 2005; 31:865-870.
- Florkowski C. Sensitivity, specificity, receiver-operating characteristics (ROC) curves and likelihood ratios: Communicating the performance of diagnostic tests. *The Clinical Biochemist Reviews*. 2008; 29:S83-S87.
- Foster FS, Mehi J, Lukacs M, et al. A new 15-50 MHz array-based micro-ultrasound scanner for preclinical imaging. *Ultrasound in Medicine and Biology*. 2009; 35:1700-1708.
- Franco M, Man S, Chen L, et al, Targeted anti-vascular endothelial growth factor receptor-2 therapy leads to short-term and long-term impairment of vasclular function and increase in tumour-hypoxia. *Cancer Research*. 2006; 66:3639-3648.
- Graham KC, Wirtzfeld LA, MacKenzie LT, et al. Three-dimensional high-frequency ultrasound imaging for longitudinal evaluation of liver metastases in preclinical models. *Cancer Research*. 2005; 65: 5231-5237.
- Gorring DR, Rossant J, Clapoff S, et al. In situ detection of beta-galactosidase in lenses of transgenic mice with a gamma-crystallin/lacz gene. *Science*. 1987; 235(4787): 456-458.

- Heyn C, Ronald JA, Ramadan SS, et al. In vivo MRI of cancer cell fate at the single-cell level in a mouse model of breast cancer metastasis to the brain. *Magnetic Resonance in Medicine*. 2006; 56:1001-1010.
- Holmgren L, O'Reully MS, Folkman J. Dormancy of micrometastases: balanced proliferation and apoptosis in the presence of angiogenesis suppression. *Nature Medicine*. 1995; 1:149-153.
- Kirstein JM, Graham KC, Mackenzie LT, et al. Effect of anti-fibrinolytic therapy on experimental melanoma metastasis. *Clinical and Experimental Metastasis*. 2009; 26:121-131.
- Luzzi KJ, MacDonald IC, Schmidt EE, et al. The multistep nature of metastatic inefficiency. *American Journal of Pathology*. 1998; 153:865-873.
- Morton DL, Wen DR, Wong JH, et al. Technical details of intraoperative lymphatic mapping for early stage melanoma. *Archives of Surgery*. 1992; 127: 392-399.
- Mumprecht V, Detmar M. Lymphangiogenesis and cancer metastasis. *Journal of Cellular and Molecular Medicine*. 2009; 13:1405–1416.
- Ren G, Miao Z, Liu H, et al. Melanin-targeted preclinical PET imaging of melanoma metastasis. *Journal of Nuclear Medicine*. 2009. 50: 1692-1699.
- Shung KK. *Diagnostic Ultrasound Imaging and Blood Flow Measurements*. New York., NY; Taylor & Francis Group. 2006

- Sibon C, Rizzatto G, Belotti E, et al, The contribution of high-resolution ultrasonography in preoperatively detecting sentinel-node metastases in melanoma patients. *Melanoma Research*. 2007; 17:233-237.
- Starritt EC, Uren RF, Scolyer RA, et al, Ultrasound examination of sentinel nodes in the initial assessment of patients with primary cutaneous melanoma. *Annals of Surgical Oncology*. 2005; 12: 18-23.
- Szabo T. *Diagnostic ultrasound imaging: inside out*. Boston, MA; Elsevier/Academic Press; 2004.
- Teachey DT, Seif AE, Brown VI, et al. Targeting Notch signalling in autoimmune and lymphoproliferative disease. *Blood*. 2008; 111: 705-714.
- Testori A, Lazzro G, Baldini F, et al. The role of ultrasound of sentinel nodes in the pre- and post-operative evaluation of stage I melanoma patients. *Melanoma Research*. 2005; 15:191-198.
- Tong S, Cardinal HN, McLoughlin RF, et al. Intra- and Inter-observer variability and reliability of prostate volume measurement via two-dimensional and three-dimensional ultrasound image. *Ultrasound in Medicine and Biology*. 1998; 24:673-681.
- Underwood EE. *Quantitative Stereology*. Massachusetts. Addison-Wesley. 1970.

Vassallo P, Edel G, Roos N, et al. In-vitro high-resolution ultrasonography of benign and malignant lymph nodes. *Investigative Radiology*. 1993; 28:698-705.

Vogt M, Opretzka J, Perrey C, et al. Ultrasonic microscanning. *Proceedings of the Institute of Mechanical Engineers Part H Journal of Engineering in Medicine*. 2010; 224: 225-240.

## **Chapter 4.0: The cellular detectability of positive contrast-labeled tumour cells at clinical field strength MRI**

### **4.1 Introduction**

The ability to non-invasively image the metastatic burden at a secondary site would provide researchers with a powerful tool to study the biology of the population of metastatic cells, as well as aid the development of novel anti-metastatic therapeutics. One such imaging modality that can detect the presence of single labeled cells, while at the same time provide fine anatomical detail to its location is cellular magnetic resonance imaging (MRI). Cellular MRI is a burgeoning field that utilizes the high resolution (50 $\mu$ m), non-invasive, and longitudinal imaging capabilities of MRI in the tracking of magnetically labeled target cells (Anderson *et al*, 2006).

The application of cellular MRI in metastasis research has provided an unprecedented view on the dynamic growth of individual tumour cells at the secondary site in live animals (Heyn *et al*, 2006). More recently, Townson *et al* (2009) demonstrated how cellular MRI can be used to assess the population of metastatic tumour cells at the secondary site in response to anti-proliferative chemotherapeutics. Both these studies have used superparamagnetic iron oxide (SPIO)-based  $T_2$ -sensitive contrast agents to magnetically label the cells and detect their presence in a whole-body scan as a dark spot or “signal void”. This “signal void” is a susceptibility artifact that extends well outside the volume

occupied by the cell, and this extension augments the detectability of the cell (Liu et al, 2009).

When using iron oxide-based contrast agents for cellular imaging *in vivo*, however, the researcher must be cognizant of several caveats that can diminish both the specificity of the iron oxide cell label, and the ability to quantify the number of labeled cells. The specificity of negative contrast enhancement from iron oxide is diminished by several endogenous sources of negative contrast in the body such as areas of hemorrhage and necrosis (Anderson et al, 2006; Liu et al 2009; Bulte 2009). Quantification of iron oxide-labeled cell number in the body becomes inaccurate in situations where labeled cells are clustered and their respective “signal voids” overlap, (Dodd et al, 1999; Heyn et al, 2006; Townson et al 2009).

To overcome the limitations of using negative contrast agents with large susceptibility artifacts, researchers have been exploring labeling methods using paramagnetic,  $T_1$ -sensitive, positive contrast agents such as gadolinium (Gd)-chelates to visualize target cells *in vivo*. Target cells labeled with Gd-chelates appear hyperintense in the MR image because the  $Gd^{3+}$  ions increase the relaxation rates ( $R_1$ ) of nearby hydrogen protons of water molecules. Since the degree of contrast enhancement is based on the concentration the gadolinium ions within a voxel (3-dimensional pixel), the main advantage in using Gd-chelates is that MR measurements are quantitative in determining target cell number, especially in high numbers, compared to assessing the number of iron

oxide-labeled cells. The ability to quantify target cell number *in vivo* using a Gd-based contrast agent is exemplified by Amirbekian and colleagues (2007) who demonstrated a strong correlation between the number of macrophages detected by histology versus MR signal enhancement from Gd-labeled macrophages. Therefore, since degree of positive contrast enhancement is reflective of target cell number, the application of positive contrast cellular MRI to non-invasively evaluate tumour cell number at a metastatic site, such as the lymph node, would prove to be useful in the non-invasive assessment of nodal status, especially in the early stages of metastatic colonization, and may guide delivery of intralymphatic therapy (Lucarelli et al, 2009).

With this goal in mind, the research described herein sets the stage for allowing accurate *in vivo* quantification of tumour cells within lymph nodes by providing a proof of principle that demonstrates the measurement of positive contrast signal enhancement and  $R_1$  relaxation rates can be a quantitative measure of tumour cell number under *in vitro* conditions. The current study utilizes a novel positive contrast agent, called gadofluorine M (GdF), which has been shown by Giesel et al (2006) to have superior signal enhancement compared to traditional Gd-chelates such as Gd-diethylene, triamino, pentaacetic acid (Gd-DTPA) when labeling stem cells.

The current work characterizes the labeling of breast cancer cells with GdF, as well as assessing the detectability and quantification of GdF-labeled cells in clinical field strength MRI. Fluorescence microscopy was used to

visualize tumour cell uptake of GdF, and estimate the efficiency of cell labeling. Previous authors (Simon et al, 2006; Terreno et al, 2006) have shown how compartmentalization of MR contrast agents into vesicles can diminish their ability to produce signal enhancement. Thus, to ascertain the possibility that the relaxivity of GdF may be diminished due to intracellular compartmentalization, immune-fluorescence confocal microscopy was used to determine if intracellular GdF was sequestered into late endosomes. Next, a range of GdF-loading concentrations were assessed for toxicity effects on breast cancer cells *in vitro*. The amounts of signal enhancement and change in  $R_1$  values from cell pellets labeled with the same range of GdF-labeling concentrations were measured *in vitro* on two clinical field strength MRI scanners: 1.5 Tesla (T) and 3T. Cell lysates of the pellets were analyzed by inductively coupled atomic emission spectroscopy to confirm whether the signal enhancement and  $R_1$  value observed across the series of cell pellets were due to corresponding changes in intracellular concentration of GdF. Next, the lower limit of detectability of GdF-labeled tumour cells was assessed in an *in vitro* agarose MRI phantom containing a series of cell pellets where the percentage of GdF-labeled tumour cells increases step-wise from 0% to 100%. Additionally, the MRI phantom was used to optimize an MR pulse sequence that produced the highest contrast between unlabeled cells and GdF-labeled cells. Finally, the MRI phantom was used to demonstrate how signal enhancement and  $R_1$  values positively correlate with tumour cell number.





## 4.2 Materials and Methods

### 4.2.1 Cell culture and *in vitro* labeling with Gadofluorine M

A lymphotropic human breast cancer cell line 231-D3H2-LN (Caliper Life Sciences, Hopkinton, Massachusetts) was grown in Dulbecco's modified essential medium (Sigma-Aldrich, Oakville, Ontario) supplemented with 10% fetal bovine serum, 5% L-glutamine, and 5% non essential amino acids, and cultures maintained at 37°C with 5% CO<sub>2</sub>.

For standard labeling conditions, 231-D3H2-LN cells were grown to 70% confluency in T75 flasks and incubated with 5mL of Opti-MEM (Invitrogen, Burlington, Ontario) containing Gadofluorine M (GdF, Bayer-Schering, Germany) for 24 hours. A fluorescent version of the compound, Gadofluorine M-carbocyanine (GdF-cc) where the mannose moiety is replaced with carbocyanin (red fluorophore), was used to optically visualize contrast agent uptake and quantify labeling efficiency. Labeling efficiency was manually quantified from 3 micrographs and was expressed as a percentage of labeled cells to total number of cells in the micrograph. The effect of different loading concentrations of GdF on cell viability was assessed in a colorimetric MTS viability assay. For the MTS cell viability assay (product# G3582, Promega, San Luis Obispo, California),  $5 \times 10^4$  tumour cells were plated in 7 wells (96 well format) corresponding to 0, 25, 100, 250, 1000, 2500, and 10000 $\mu$ M of GdF in Opti-MEM and labeled for 24 hours. After incubation, cells were washed and the MTS assay was performed

according to manufacturer's instructions and plates were scanned using a standard plate reader at absorbance 490nm. The assay was performed in triplicate.

#### **4.2.2 Visualizing intracellular localization of GdF in breast cancer cells**

To visualize the intracellular localization of GdF after uptake, a fluorescent version of the contrast agent, gadofluorine M-carbocyanine (GdF-cc; Bayer-Scherring, Germany) was used to label the 231-D3H2-LN cells. Cells were grown to 70% confluency in a 2 chamber slide (Nalge Nunc International, New York, USA) and were labeled with a 0.05  $\mu\text{mole/mL}$  working concentration GdF-cc in Opti-MEM for 24 hours. After 24 hours, cells were washed with 0.1M phosphate buffered saline (PBS, pH 7.2). Cells were fixed in 1.2% formalin in phosphate buffer for 12 minutes then washed with PBS. To permeabilize cells, cells were incubated in PBS with 0.01% Tween-20 for 10 minutes. The chamber slides were then blocked with 4% bovine serum albumen (BSA) for 10 minutes at room temperature. Antibodies against mannose-6-phosphate receptor (Abcam, Massachusetts, USA), a late endosomal marker, were diluted 1:200 with 4% BSA in PBS and incubated on the cells overnight in a humidified chamber at 4°C. Slides were washed and blocked for 10 minutes prior to the addition of fluorescent secondary antibodies (goat anti-mouse conjugated to fluorescein isothiocyanate, FITC; Jackson ImmunoResearch Laboratories, Pennsylvania, USA). Slides were incubated with secondary antibodies in a humidified chamber in the dark for 1 hour. Slides were then washed with PBS and counter-stained

with blue fluorescent 4',6-diamidino-2-phenylindole (DAPI; Sigma-Aldrich) for 5 minutes. To test for specificity of the fluorescence immunostain, tumour cells were incubated with goat anti-mouse secondary antibodies conjugated to FITC only. Slides were mounted in Vectashield (Vector Laboratories, Ontario, Canada) and imaged by a Zeiss LSM 410 confocal microscope equipped with a He/Ne laser, Kr/Ar laser, and UV laser.

#### **4.2.3 *In vitro* MRI of cell pellets labeled at different GdF-loading concentrations**

To assess the detectability of breast cancer cells labeled with GdF at different loading concentrations, cell pellets consisting of  $1 \times 10^7$  labeled cells for each loading concentration (0, 25, 100, 250, 100, 2500, 10000  $\mu\text{M}$ ) were prepared in sextuplet. Labeling conditions are as stated in "Standard labeling conditions" in section 4.2.1. Cell pellets were spun down in a PCR multiplate (364-well format) to allow for convenient single slice MR sampling of each cell pellet/GdF loading condition. After centrifugation, images of the phantom and metric ruler were taken with a digital camera in order to determine the dimensions of the cell pellets. Afterwards, the gel phantom was scanned using both 1.5T (GE CV/i whole-body clinical MR scanner) and 3T (GE 750 whole body MR imager) clinical strength scanners to determine which field strength provided the best quality of image since it is well known that the relaxivity of gadolinium chelates is field dependent (Rinck et al, 1999).

To compare image quality of the cell pellets scanned at 1.5T and 3T, we evaluated the signal-to-noise ratio (SNR) and contrast-to-noise ratio (CNR) in the images obtained from each scanner. SNR is equal to the mean signal intensity of the object divided by the standard deviation of the mean noise of the background (air). CNR is the difference between brightest cell pellet and unlabeled cell pellet divided by the standard deviation of the mean noise of the background (air).

#### **4.2.4 Measurement of $T_1$ relaxation times of cell pellets labeled at different GdF-loading concentrations.**

Using a 1.5T scanner, cell pellets were serially scanned with spin-echo inversion recovery (IR) pulse sequences at various inversion times (50ms, 100ms, 200ms, 300ms, 500ms, 800ms, 1200ms, 1800ms, 2500ms, 3500ms), where TR: 3000ms, TE: minimum 10.1 ms, NEX:6, BW:20.83, Freq: 256, phase:128, field of view: 8cm, slice thickness: 2 mm. Pellets were then scanned using a 3T scanner where serial spin-echo inversion recovery spin-echo images were obtained with the previously described scanning parameters at 1.5T.  $T_1$  maps at both 1.5 and 3T were generated by importing the series of IR images into an MRImapper software package (Beth Israel Deaconess Medical Center, Boston, Massachusetts). Signal enhancement measurements of the cell pellets were obtained using image analysis software ImageJ (NIH, Bethesda, Maryland).

#### **4.2.5 Quantification of intracellular GdF by inductively coupled plasma atomic emission spectroscopy**

To determine the amount of GdF in tumour cells at each loading concentration of GdF, we performed inductively coupled plasma atomic emission spectroscopy (ICP-AES) on lysates of each cell pellet. To prepare lysates, cell pellets were resuspended and fast frozen and thawed twice to disrupt cell membranes. 2M nitric acid ( $\text{HNO}_3$ ) was added to each cell suspension to a final volume of 3mLs. The resulting suspensions were left overnight at  $60^\circ\text{C}$ . After incubation at  $60^\circ\text{C}$  the cell suspensions were centrifuged to remove insoluble material. The solutions were then nebulized in argon plasma and measured by a Perkin-Elmer Optima-3300 DV system. The 342 nm atomic emission line of Gd was chosen for the ICP-AES analysis. The intensity of the emission line is directly proportional to the amount of Gadolinium in the sample. Sample intensities were compared to reference standards of known amounts of GdF. The amount of gadofluorine M in each cell pellet was expressed as femtomoles per cell.

#### **4.2.6 Construction of gel phantom for *in vitro* MRI scanning**

To mimic the pathological situation where tumour cells progressively colonize the mouse lymph node, and to determine whether or not positive-contrast enhanced MRI is sensitive enough to detect and measure (via signal enhancement and  $T_1$  relaxation times) differences in tumour cell number, a gel phantom was constructed to contain seven wells with cell pellets consisting of

increasing ratios of GdF-labeled tumour cells to unlabeled tumour cells. Cell pellets were made from  $1 \times 10^7$  tumour cells labeled with  $1000 \mu\text{m}$  GdF using previously described cell culture conditions. A 1% agarose gel (in Hank's buffered saline solution, Invitrogen, Ontario, Canada) was solidified in a cell culture 50mL conical tube and contained 7 cylindrical wells (height 40 mm, diameter 2 mm). Seven cell suspensions (total cell number  $1 \times 10^7$  cells) with increasing of percentage of GdF-labeled tumour cells (0%, 4%, 8%, 16%, 31%, 62%, 100% labeled cells) were loaded into the wells of the gel phantom. The gel phantom was spun down at 800rpm for 5 minutes to pellet the cells prior to scanning by MRI.

#### **4.2.7 Evaluating 3D SPGR, and FIESTA pulse sequences for imaging MRI phantom**

We compared two different pulse sequences, 3D-spoiled gradient recoiled (3D-SPGR) and fast imaging employing steady state acquisition (FIESTA) in detecting the GdF-labeled tumour cells.  $T_1$ -weighted 3DSPGR is a commonly used MR sequence that provides higher SNR images with  $T_1$ -weighted contrast. The FIESTA pulse sequence is known to offer the highest possible signal-to-noise ratio (SNR) per unit time of all known sequences but may not be sensitive to the gadolinium-based contrast agents (Scheffler and Lehnardt, 2003). These two pulse sequences were optimized by adjusting the flip angles ( $10^\circ$ ,  $20^\circ$ ,  $30^\circ$ ,  $40^\circ$ ,  $50^\circ$ ).

#### **4.2.8 Measurement of $T_1$ relaxation times of cell pellets containing different ratios of GdF-labeled tumour cells.**

To measure the  $T_1$  relaxation times and signal enhancement of the pellets, the gel phantom was scanned at 3T using a series of fast spin-echo inversion recovery pulse sequence using different inversion times (50ms, 100ms, 200ms, 300ms, 400ms, 600ms, 800ms, 1000ms, 1200ms, 1400ms, and 2400ms); where TR: 4000ms, TE:minimum 9.96ms, NEX: 6, BW:20.83, Freq: 256, phase:128, field of view:8cm, slice thickness: 2 mm.  $T_1$  maps were generated as described in section 4.2.4.  $T_1$  relaxation times from 144 voxels sampled from each cell pellet were obtained and analysed by methods described in “Statistical Analysis.”

#### **4.2.9 Statistical analysis**

Statistical analysis was performed using Microsoft Excel 2007 (Microsoft Corporation, Redmond, Washington) and GraphPad Prizm version 4.0 (GraphPad Software Inc., San Diego, California) for Windows XP. Prior to performing statistical analyses on means, data were tested for normality. When data were normally distributed, the comparison of several means were compared by analysis of variance (ANOVA), and post-hoc Tukey’s multiple comparisons test was performed to determine which means were significantly different. When data were not normally distributed, the comparison of several means was done using the Kruskal-Wallis test, and post-hoc analysis using Dunn’s multiple comparisons test.



To correlate MR measurements of signal enhancement (grey values) and  $R_1$  values to the actual number of GdF-labeled tumour cells, a correlation coefficient ( $r^2$ ) value was generated using a linear regression model to determine if a positive correlation existed between the two parameters.

### **4.3 Results**

#### **4.3.1 Labeling efficiency and cell viability at different loading concentration of GdF**

To visualize uptake and quantify labeling efficiency, we used GdF-cc as a surrogate marker of tumour cell uptake of the non-fluorescent version of the compound. The breast cancer cells labeled with GdF-cc are shown in Figure 4.1. From three fluorescent micrographs, labeling efficiency ranged from 98-100%. The MTS cell viability assay shows the range of GdF-loading concentrations (25 $\mu$ M to 1000 $\mu$ M) that do not significantly affect cellular metabolism (dehydrogenase activity) when compared to unlabeled tumour cells. Above 1000 $\mu$ M of GdF-loading, cellular metabolism becomes significantly lower (represented by lower absorbance values) than unlabeled cells.

#### **4.3.2 Visualization of intracellular localization of GdF by immunofluorescence microscopy**

To determine if GdF was being sequestered into endosomes, we stained GdF-cc labeled tumour cells with the late endosomal marker mannose-6-phosphate receptor, the results of which are shown as a maximum intensity projection confocal image in Figure 4.2. The red pixels represent the distribution of GdF-cc contrast agent throughout the cytosol. The green punctate pattern represents the location of late endosomes. The fluorescent micrograph qualitatively illustrates how the GdF contrast agent is found throughout the

cytosol, and is not sequestered into late endosomes, suggesting that the observed contrast enhancement was not diminished by compartmentalization into vesicles.

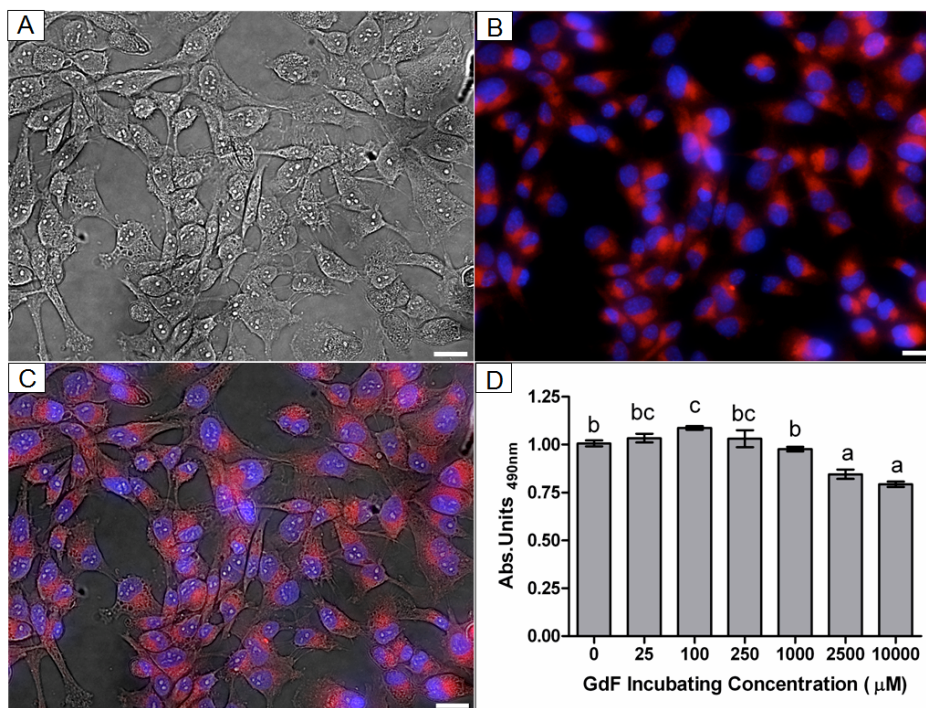


**Figure 4.1. Tumour cell uptake of GdF-cc, labeling efficiency, and cell viability from GdF-loading.** Panel A displays lymphotropic 231-D3H2-LN human breast cancer cells shown in brightfield. Panel B is a fluorescent micrograph showing GdF-cc (red) uptake and nuclei are stained with DAPI (blue). Panel C is a fused image of panels A and B. Scalebar = 20µm. In panel D, cellular metabolism (dehydrogenase activity) was the dependant variable measured at the indicated range of loading concentrations of GdF. Means ± standard deviations are shown. The observed means analysed by ANOVA ( $p < 0.0001$ ) and pairs of means were compared by Tukey's multiple comparisons test where columns that were significantly different are denoted by different letters; columns with the same letters are not significantly different.

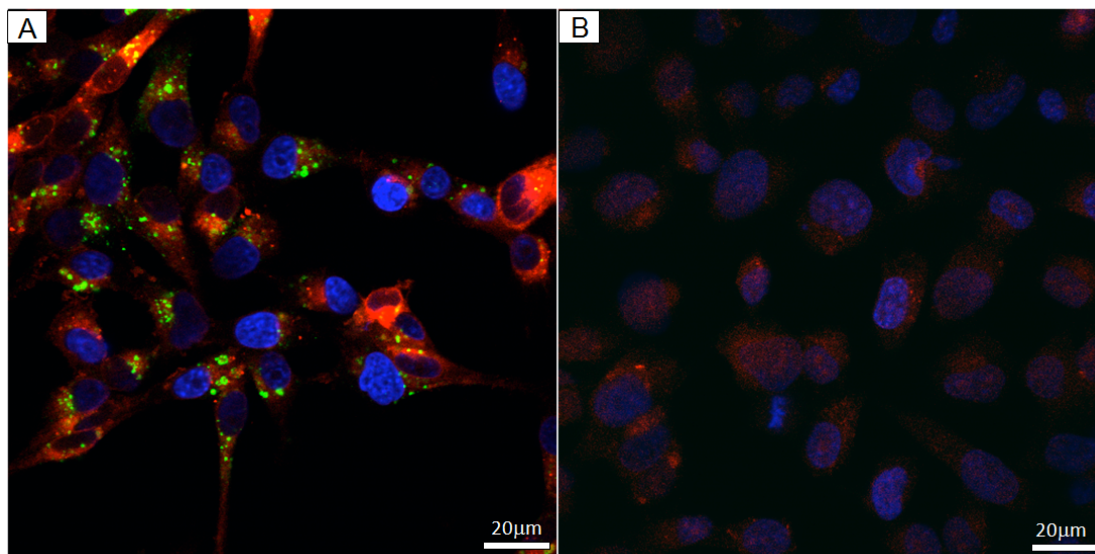


**Figure 4.2 Visualization of intracellular location of GdF-cc in tumour cells by immunofluorescent microscopy.** Confocal maximum intensity projection images are shown in panels A and B. In panel A, GdF-cc labeled tumour cells were immunostained for mannose-6-phosphate (late endosomal marker) to determine if the MRI contrast agent was sequestered into endosomes. GdF-cc (red) did not colocalize into endosomes, instead, GdF can be found throughout the cytoplasm. To differentiate specific fluorescent staining and autofluorescence, panel B shows tumour cells that were only stained with secondary FITC-conjugated antibodies. Nuclei are counterstained with DAPI (blue). Scalebar = 20µm.

### **4.3.3 MRI of cell pellets with different loading concentrations of GdF scanned at 1.5T & 3T**

The ability to measure changes in signal enhancement and  $T_1$  relaxation times from the presence of labeled tumour cells in a metastatic site at clinical field strengths lend to the translation of these findings to clinical applications. Therefore, we assessed the sensitivity of 1.5T and 3T clinical scanners in detecting the changes in signal enhancement and  $T_1$  relaxation times of cell pellets labeled at different loading concentrations of GdF. Examples of  $T_1$ -weighted images of the cell pellets scanned at 1.5T and 3T using a spin-echo pulse sequence are shown in Figure 4.3 A and B, respectively. In regards to evaluating image quality as defined by SNR and CNR, images scanned at 3T were ~5-fold higher in SNR and CNR compared to 1.5T. Actual values are listed in the figure legend of Figure 4.3.

### **4.3.4 Quantification of signal enhancement and $T_1$ relaxation of cell pellets of different GdF-loading conditions at 1.5T and 3T**

Two-dimensional cross-sectional slices of the cell pellets were used to assess signal enhancement and  $T_1$  relaxation at both 1.5T and 3T. Changes in  $R_1$  relaxation rates ( $1/T_1$ ) as a function of GdF-loading concentration at 1.5T and 3T are depicted in Figure 4.4 C and D, respectively. Although the changes in  $R_1$  times over different GdF-loading conditions show a similar trend, we see  $R_1$  values are slightly higher at 1.5T compared to 3T. The signal enhancement of

cell pellets was examined at 1.5T and 3T in Figure 4.4 E and F, respectively, we see similar changes in signal intensity, however at 1.5T, signal intensities are slightly higher. In light of the cell viability assay at various GdF-loading concentrations (Figure 4.1 D), tumour cells are able to tolerate a range of GdF-loading concentrations (from 25 to 1000 $\mu$ M) without having significant effects on cell viability. Within this range of concentrations, no significant changes in  $R_1$  values and signal enhancement were observed. At higher GdF-loading concentrations (2500 $\mu$ M to 10000 $\mu$ M) significant increases in signal enhancement and  $R_1$  relaxation rates were observed, however tumour cell viability was significantly reduced at these higher loading conditions.

#### **4.3.5 Intracellular concentration of GdF of cell pellets over a range of GdF-loading conditions**

Cellular GdF uptake was expressed as femtomole per cell. The amount of GdF per cell is shown in Figure 4.5. GdF-loading concentrations from 25 $\mu$ M to 1000 $\mu$ M did not significantly change the intracellular concentration of GdF. However from 2500 $\mu$ M to 10000 $\mu$ M, the amount of intracellular GdF increased, with 10000 $\mu$ M showing the highest level of intracellular GdF.

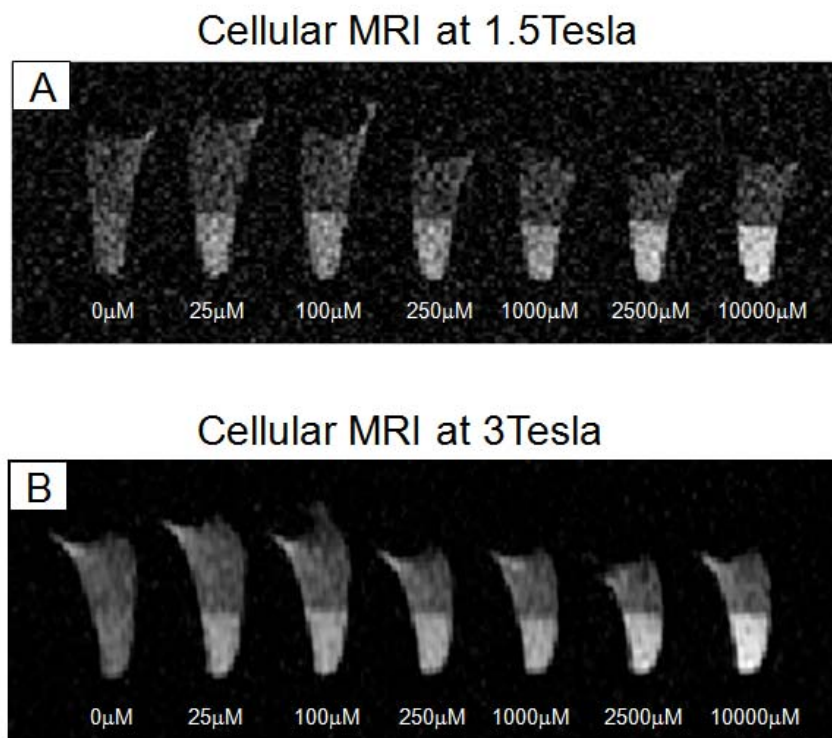


**Figure 4.3 Cellular MRI of cell pellets labeled at different loading concentrations of GdF.** Examples of  $T_1$ -weighted spin echo images of cell pellets taken at 1.5T and 3T are shown in panels A and B, respectively. At 1.5T, SNR = 7.4 and CNR = 4.1; whereas at 3T, SNR = 35.5 and CNR = 18.6.

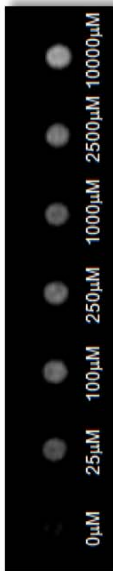


**Figure 4.4 Cellular MRI of cell pellets at 1.5T and 3T.**

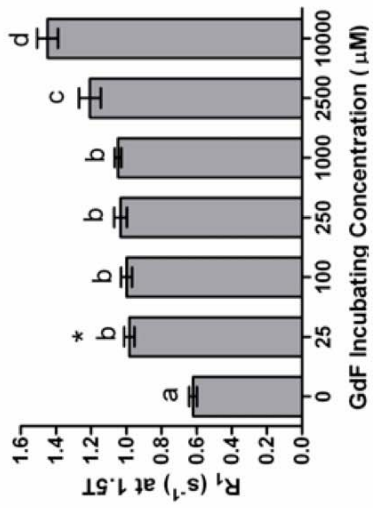
Measurements of  $R_1$  relaxation rates and signal enhancement (grey values) at 1.5T and 3T were sampled from 2D MR slices, as shown in panels A and B, respectively.  $R_1$  values were obtained from  $T_1$  maps constructed from a series of inversion recovery images taken at varying TI times, as shown in panels C and D. Signal enhancement measurements are shown in panel E and F, respectively. Means and standard deviations of 6 cell pellets labeled with the same GdF-loading condition are shown. Groups were analyzed by ANOVA ( $p < 0.0001$ ) and pairs of columns were analyzed by Tukey's multiple comparisons test. Pairs of columns with the same letter are not significantly different, whereas columns with different letters are significantly different.

### Cellular MRI at 1.5Tesla

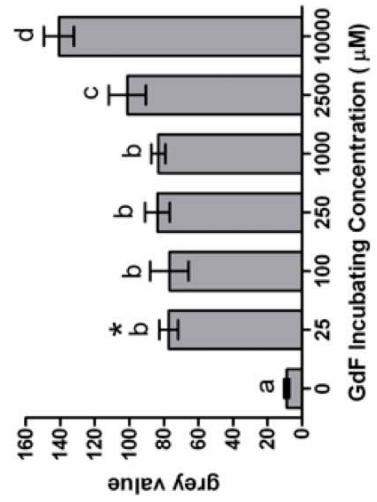
A



C



E

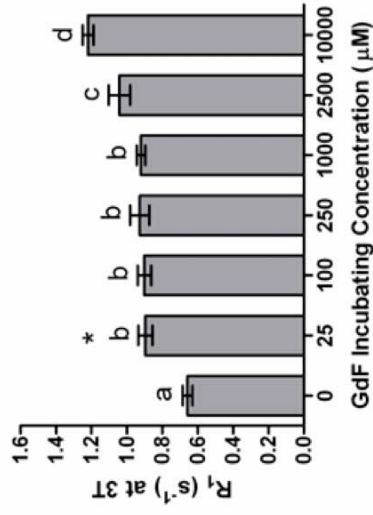


### Cellular MRI at 3Tesla

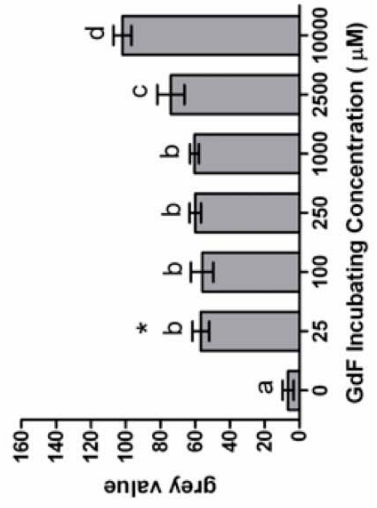
B



D



F



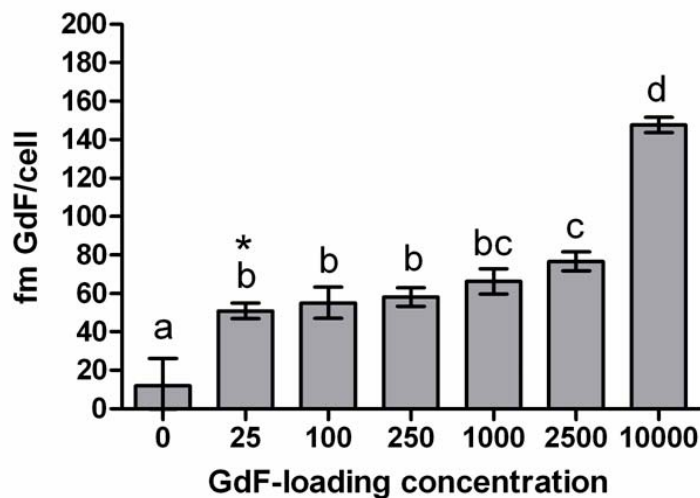


**Figure 4.5 Measurement of intracellular GdF of cell pellets by ICP-AES.**

ICP-AES was used to measure intracellular GdF of cell pellets labeled at different loading concentrations. Means and standard deviations of 6 cell pellets labeled with the same GdF-loading condition are shown. Groups were analyzed by ANOVA ( $p < 0.0001$ ); pairs of columns were analyzed by Tukey's multiple comparisons test. Pairs of columns with the same letter are not significantly different, whereas columns with different letters are significantly different.

#### **4.3.6 *In vitro* MRI phantom to assess the detectability of GdF-labeled tumour cells at varying numbers**

To mimic the pathological situation where tumour cells progressively colonize a given volume of tissue at the metastatic site (eg. lymph node), we constructed an MRI phantom (Figure 4.6 A,B) to contain a series of cell pellets that have the same volume and total cell number, but where the percentage of GdF-labeled tumour cells mixed with unlabeled tumour cells was increased (ie. 0%, 4%, 8%, 31%, 62%, 100% GdF-labeled tumour cells in total cell pellet).

#### **4.3.7 Comparison of CNR from 3D SPGR and FIESTA pulse sequences**

Two MR pulse sequences (3D SPGR and FIESTA) were assessed to determine which sequence maximizes the CNR. The MRI phantom was imaged with each pulse sequence at varying flip angles to determine which parameters provided images with the best contrast to noise ratio. 3D SPGR images at varying flip angles are shown in Figure 4.7 panels A-E, and the calculated CNR value for each image is shown. From these images it is evident that a SPGR pulse sequence with a flip angle of  $10^0$  maximizes the contrast between the cell pellet consisting of 100% labeled tumour cells and the unlabeled cell pellet. FIESTA images shown at varying flip angles are shown in Figure 4.3.8 panels F-J. The FIESTA sequence provides high SNR images, however, the change of signal intensity does not relate to the concentration of GdF as demonstrated by Figure 4.7 panels I and J.

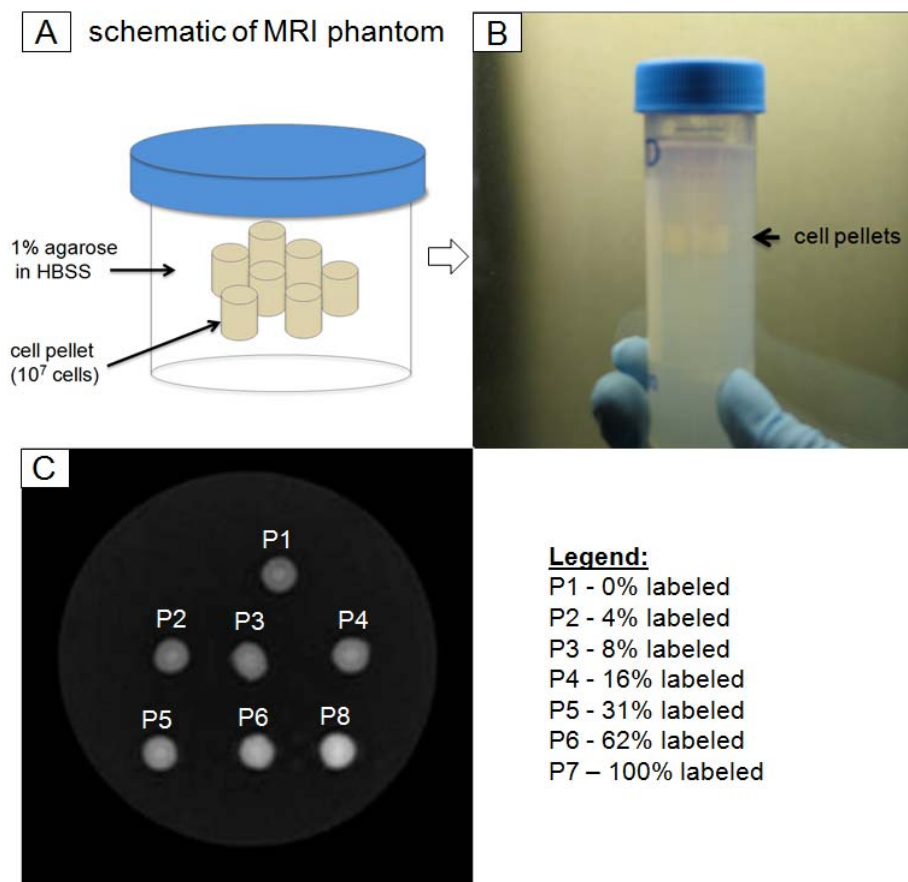
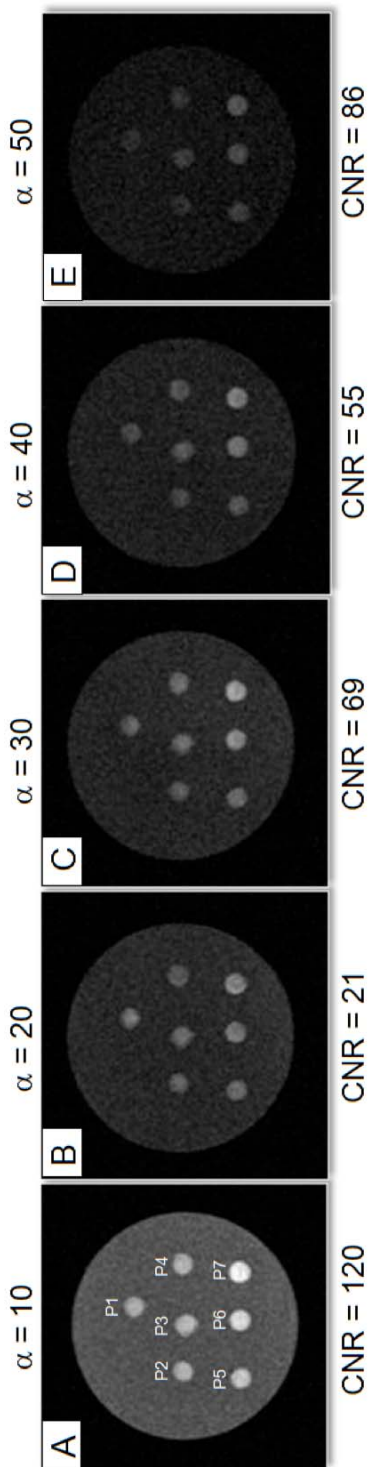


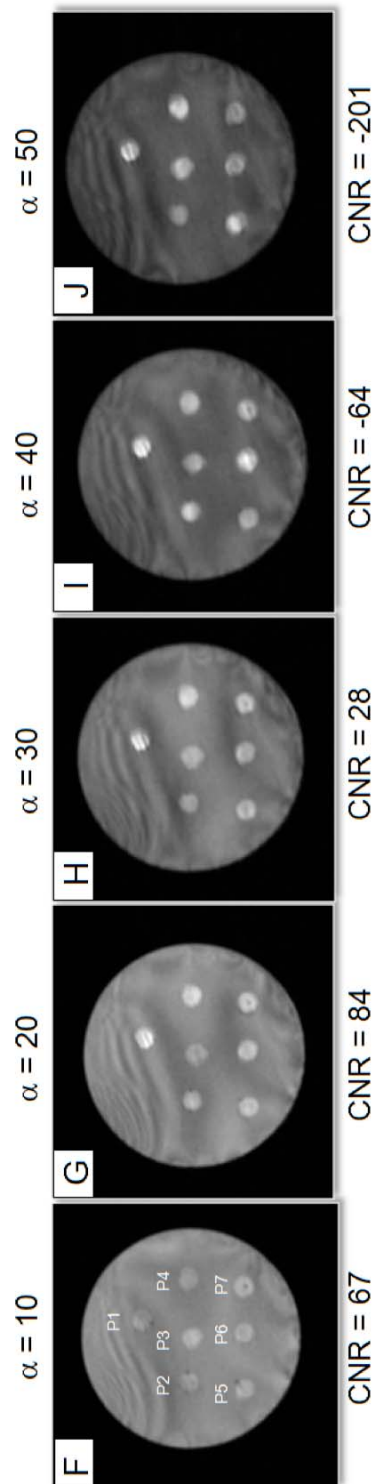
**Figure 4.6 MRI phantom to assess the sensitivity of positive-contrast enhancement at 3T in detecting differing amounts of GdF-labeled tumour cells.** A schematic of a 1% agarose gel in a 50mL conical culture tube containing a series of cell pellets ( $1 \times 10^7$  total number of cells) with increasing percentage of GdF-labeled tumour cells, is shown in panel A. The actual phantom is shown in panel B. Panel C shows an example image of a 2D cross-sectional MRI slice taken at 3T. The percentage of labeled tumour cells in each pellet is indicated in the legend. The actual volume of the cell pellets was measured to be  $\sim 19.8 \text{ mm}^3$  ( $r = 1 \text{ mm}$ ,  $h = 6.3 \text{ mm}$ ).

**Figure 4.7 Comparison of image quality between 3D SPGR and FIESTA pulse sequences.** Image quality as defined by high CNR was evaluated in two MRI pulse sequences: 3D SPGR and FIESTA. CNR was calculated as the difference between the cell pellet with 100% GdF-labeled cells (P7, dashed square) and unlabeled cell pellet (P1, dashed circle) divided by the standard deviation of background noise. 3D-SPGR images are shown at varying flip angles ( $\alpha$ ) in panels A-E. FIESTA images are shown at varying flip angles in panels F-J. CNR values are listed below each image.

## 3D SPGR



## FIESTA



#### **4.3.8 Increased signal enhancement and $R_1$ relaxation rates of cell pellets with higher numbers of GdF-labeled tumour cells**

In Figure 4.8 A, a 3D SPGR (flip angle  $10^\circ$ ) image is shown. The mean signal enhancement (mean grey value) of each cell pellet, sampled by a pixel-by-pixel basis from the 3D SPGR image are shown in the graph in Figure 4.8 C. Signal enhancement is shown to increase significantly in a dose-dependent manner from 8% to 100% GdF-labeled cell pellet. 8% corresponds to  $8 \times 10^5$  GdF-labeled cells within the cell pellet.  $T_1$  relaxation values of the cell pellets are represented in a  $T_1$  map of the phantom shown in Figure 4.8 B. The mean  $R_1$  values ( $1/T_1$ ) sampled from a pixel-by-pixel basis from the  $T_1$  map are shown in Figure 4.8 D. Statistical analysis of  $R_1$  values demonstrates the lowest percentage of GdF-labeled tumour cells required to produce a significant increase in  $R_1$  is 4%, or  $4 \times 10^5$  GdF-labeled cells.

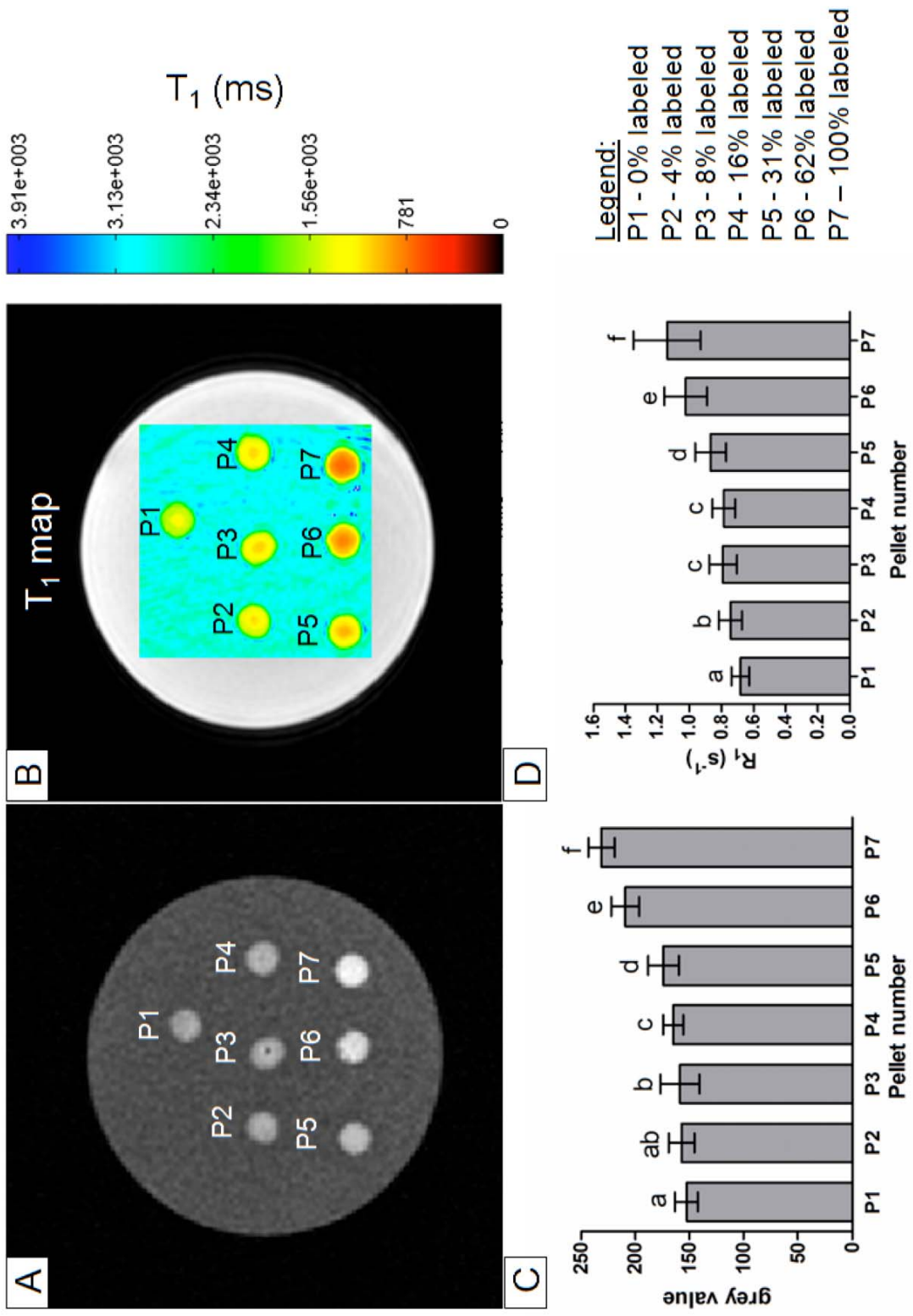
#### **4.3.9 The change in MR signal enhancement and $R_1$ measurements strongly correlates to the number of GdF-labeled tumour cells.**

To demonstrate that MR measurements of signal enhancement and  $R_1$  values can be used as a quantitative measure of the abundance of GdF-labeled tumour cells within a given volume, linear regression analysis was performed to determine the correlation coefficient each parameter. In both cases, the change in signal enhancement or  $R_1$  value strongly correlated with tumour cell number, correlation coefficients were  $r^2 = 0.93$  and  $r^2 = 0.93$ , respectively. The high



degree of correlation demonstrates the feasibility of using positive contrast enhancement to quantify the abundance of tumour cells.

**Figure 4.8 MRI of cell pellets containing different proportions of GdF-labeled tumour cells.** Panel A shows a 2D cross-sectional MR scan of the phantom using a 3DSPGR pulse sequence with a  $10^\circ$  flip angle. Quantification of signal enhancement (144 voxels sampled from each cell pellet) is shown below in panel C. In panel B, a  $T_1$  map of the phantom was obtained from a series of inversion recovery images taken with varying TI times. 144 voxels from each cell pellet were sampled to obtain  $T_1$  relaxation times, which was then expressed as  $R_1$  relaxation rates ( $1/T_1$ ) and analyzed in the graph in panel D. Means and standard deviations of 144 voxels in both panels C and D are shown. Groups were analyzed by ANOVA ( $p < 0.0001$ ) and pairs of columns were analyzed by Tukey's multiple comparisons test. Pairs of columns with the same letter are not significantly different, whereas columns with different letters are significantly different from each other.



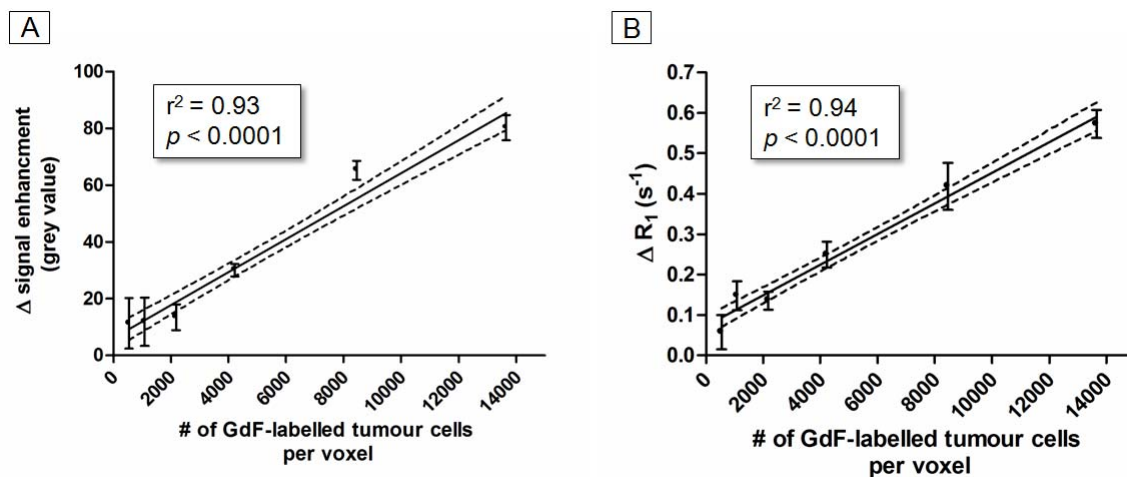


**Figure 4.9 Changes in MR signal enhancement and  $R_1$  values strongly correlate with the number of tumour cells per voxel.** Panel A shows a strong correlation ( $r^2 = 0.93$ ,  $p < 0.0001$ ) between the change in signal enhancement (from unlabeled cells) with the concentration of GdF-labeled tumour cells per voxel. In panel B demonstrates a strong correlation ( $r^2 = 0.94$ ,  $p < 0.0001$ ) between the change in  $R_1$  relaxation rate (from unlabeled cells) with the concentration of GdF-labeled tumour cells per voxel.

#### 4.4 Discussion

The utility of cellular MRI in the assessment of tumour cells in secondary organs in the preclinical setting has been well demonstrated by Heyn and colleagues (2006). Furthermore, cellular MRI can be used to assess the efficacy of chemotherapeutics on the metastatic cell population at the secondary site (Townson et al, 2009). Both these studies use SPIO to magnetically label tumour cells. Iron-oxide-based contrast agents are extremely sensitive in single cell detection since iron oxide particles produce large susceptibility artifacts (signal void) that extends far beyond the volume of the actual labeled cell (Liu et al, 2009). Quantification of iron-oxide labeled tumour cells in the secondary organ is possible when the distribution of cells is sparse enough to count individual cells (Heyn et al, 2006; Townson et al, 2009). However, in situations where the distribution of iron-oxide labeled cells are concentrated into small volume where their respective signal voids “overlap”, measurements of signal void area, volume, and  $R_2$  relaxation rates become inaccurate (Heyn et al, 2006, Rad et al; 2007; Townson et al, 2009).

To overcome this limitation, the use gadolinium-based positive contrast agents in cellular detection *in vivo* can offer an alternative method of quantifying the number tumour cells at the metastatic site. For Gd-chelates, contrast enhancement is dependent on the local concentration of  $Gd^{3+}$  ions and their efficiency in relaxing nearby water protons (Caravan 2006), rather than producing a large hypointense susceptibility artifact. Although not as well suited in detecting

single cells, Gd-chelates have successfully been used in imaging target cells “in bulk” within animals. For example, Nolte and colleagues (2008) were able to image  $1 \times 10^6$  GdF-labeled glioma cells injected into the mouse brain. Several other groups have explored positive contrast enhanced cellular MR imaging using other cell types such mesenchymal stem cells (Geisil et al, 2006), human monocytes (Henning et al, 2007), and macrophages (Adler et al, 2010). To date, however, studies in exploring the use of gadolinium-based positive contrast agents in quantifying tumour cell number at the metastatic site are lacking.

To address the need for improved methods in quantifying tumour cells at the secondary site, the current work sets the stage for *in vivo* quantification of tumour cells by providing a proof of principle that demonstrates MR measurements of positive contrast enhancement can be correlated with the number of Gd-labeled tumour cells, under *in vitro* conditions. The current research demonstrates the feasibility of labeling breast cancer cells with GdF, a novel Gd-chelate, and demonstrates the cellular detectability of GdF-labeled cells by MRI at clinical-field strengths such as 3T. By using an MR phantom containing a series of cell pellets with increasing amounts of GdF-labeled tumour cells, the current study demonstrates how the change in MR measurements such as signal enhancement and  $R_1$  values are quantitative measures of the number of tumour cells. Furthermore, the lowest amount of labeled cells per voxel detected by  $R_1$  measurements was 546 cells, which corresponded to a cell pellet containing  $4 \times 10^5$  labeled cells.

Future studies that use targeted Gd-chelates to detect metastatic cells can use the information provided in the current study to quantify tumour cell number in secondary organs *in vivo* using parameters such as signal enhancement and  $R_1$  values. The ability to quantify the abundance of metastatic cells in secondary organs will prove to be an invaluable tool in accurately assessing metastatic burden, as well as determining the efficacy of anti-metastatic therapeutics.

#### 4.5 References

- Adler ED, Bystrup A, Briley-Saebo KC, et al. In vivo detection of embryonic stem cell-derived cardiovascular progenitor cells using Cy3-labeled gadofluorine M in murine myocardium. *Journal of the American College of Cardiology: Cardiovascular Imaging*. 2009; 2: 1114-1122.
- Amirbekian V, Lipinski MJ, Briley-Saebo KC, et al. Detecting and assessing macrophages in vivo to evaluate atherosclerosis noninvasively using molecular MRI. *Proceedings of the National Academy of Sciences*. 2007; 10: 961-966.
- Anderson SA, Lee KK, Frank JA. Gadolinium-Fullerenol as a paramagnetic contrast agent for cellular imaging. *Investigative Radiology*. 2006; 41: 332-338.
- Bulte JW. In vivo MRI cell tracking: Clinical studies. *American Journal of Roentgenology*. 2009; 193:314-325.
- Bulte JW, Douglas T, Witwer B. Magnetodendrimers allow endosomal magnetic labeling and in vivo tracking of stem cells. *Nature Biotechnology*. 2001; 19:1141-1147.
- Cady B. Regional lymph node metastases, A singular manifestation of the process of clinical metastases in Cancer: Contemporary animal research and clinical reports suggest unifying concepts. In: Rosen ST (series ed.), Leong



- SPL (book ed.). *Cancer Treatment and Research: Cancer Metastasis and the Lymphovascular System, Basis for rational Therapy*. New York, NY: Springer Science+Business Media, LCC; 2007:185-202.
- Caravan P, Ellison JJ, McMurry TJ. Gadolinium (III) chelates as MRI contrast agents: structure, dynamics, and applications. *Chemical Reviews*. 1999; 99: 2293-2352.
- Caravan P. Strategies for increasing the sensitivity of gadolinium based MRI contrast agents. *Chemical Society Reviews*. 2006; 35: 512-523.
- Chambers AF, Groom AC, MacDonald IC. Dissemination and growth of cancer cells in metastatic sites. *Nature Reviews Cancer*. 2002; 2:563-572.
- Dodd SJ, Williams M, Suhan JP, et al. Detection of single mammalian cells by high-resolution magnetic resonance imaging. *Biophysical Journal*. 1999; 76: 103-109.
- Erdogan S, Medarova ZO, Roby A, et al. Enhanced tumour MR imaging with gadolinium-loaded polychelating polymer-containing tumour-targeted liposomes. *Journal of Magnetic Resonance Imaging*. 2008; 27: 574-580.
- Foster PJ, Dunn EA, Karl KE et al. Cellular magnetic resonance imaging: in vivo imaging of melanoma cells in lymph nodes of mice. *Neoplasia*. 2008; 10: 207-2016.

- Giesel FL, Stroick M, Griebe M, et al. Gadofluorine M uptake in stem cells as a new magnetic resonance imaging tracking method. *Investigative Radiology*. 2006; 41: 868-873.
- He Y, Rajantie I, Pajusola K, et al. Vascular endothelial cell growth factor receptor 3-mediated activation of lymphatic endothelial is crucial for tumour cell entry and spread via lymphatic vessels. *Cancer Research*. 2005; 65: 4739-4746.
- Henning TD, Saborowski O, Golovko D, et al. Cell labeling with the positive MR contrast agent Gadofluorine M. *European Radiology*. 2007; 17: 1226-1234.
- Heyn C, Bowen CV, Rutt BK. Detection threshold of single SPIO-labeled cells with FIESTA. *Magnetic Resonance in Medicine*. 2005; 53: 312-230.
- Heyn C, Ronald JA, Ramadan SS, et al. In vivo MRI of cancer cell fate at the single-cell level in a mouse model of breast cancer metastasis to the brain. *Magnetic Resonance in Medicine*. 2006; 56:1001-1010.
- Kraitchman DL, Caravan P. Magnetic resonance labeling of stem cells: Is positive tracking a plus or minus? *Journal of the American College of Cardiology: Cardiovascular Imaging*. 2009; 2: 1123-1125.
- Liu W, Frank JA. Detection and quantification of magnetically labeled cells by cellular MRI. *European Journal of Radiology*. 2009; 70: 258-264.

- Long CM, van Laarhoven HW, Bulte JW, et al. Magnetovaccination as a novel method to assess and quantify dendritic cell tumour antigen capture and delivery to lymph nodes. *Cancer Research*. 2009; 69: 3180-3187.
- Lucarelli RT, Ogawa M, Kosaka N, et al. New approaches to lymphatic imaging. *Lymphatic Research and Biology*. 2009; 7:205-214.
- Misselwitz B, platzek J, Weinmann HJ. Early MR lymphography with gadofluorine M in rabbits. *Radiology*. 2004; 231: 682-688.
- Morawski AM, Winter PM, Crowder KC, et al. Targeted nanoparticles for quantitative imaging of sparse molecular epitopes with MRI. *Magnetic Resonance in Medicine*. 2004; 51: 480-486.
- Nolte IS, Gungor S, Erber R, et al. In vitro labeling of glioma cells with gadofluorine M enhances T<sub>1</sub> visibility without affecting glioma cell growth or motility. *Magnetic Resonance in Medicine*. 2008; 59: 1014-1020.
- Rad AM, Arbab AS, Iskander AS, et al. Quantification of superparamagnetic iron oxide (SPIO)-labeled cells using MRI. 2007; 26:366-374.
- Rinck PA, Muller RN. Field strength and dose dependence of contrast enhancement by gadolinium-based MR contrast agents. *European Radiology*. 1999; 9:998-1004.

- Riviere C, Boudghene FP, Roger J. Iron oxide nanoparticle-labeled rat smooth muscle cells: cardiac MR imaging for cell graft monitoring and quantification. *Radiology*. 2005; 235: 959-967.
- Rohani R, Chickera SN, Willert C, et al. In vivo cellular MRI of dendritic cell migration using micrometer-sized iron oxide (MPIO) particles. *Molecular Imaging and Biology*. 2010; DOI: 10.1007/s11307-010-0403-0
- Rose A. The sensitivity of performance of the human eye on an absolute scale. *Journal of the Optical Society of America*. 1948; 38: 196-208.
- Scheffler K, Lehnhardt S. Principles and applications of balanced SSFP techniques. *European Radiology*. 2003; 13: 2409-2418.
- Schoppmann SF, Birner P, Stockl J, et al. Tumour-associated macrophages express lymphatic endothelial growth factors and are related to peritumoural lymphangiogenesis. *American Journal of Pathology*. 2002; 161: 947-956.
- Shapiro EM, Sharer K, Skrtic S, et al. In vivo detection of single cells by MRI. *Resonance in Medicine*. 2006; 55: 242-249.
- Simon GH, Bauer J, Saborovski O, et al.  $T_1$  and  $T_2$  relaxivity of intracellular and extracellular USPIO at 1.5T and 3T clinical MR scanning. *European Radiology*. 2006; 16:738-745.
- Stacker SA, Caesar C, Baldwin ME, et al. VEGF-D promotes the metastatic spread of tumour cells via the lymphatics. *Nature Medicine*. 2001; 7: 186-191.

- Terreno E, Geninatti CS, Belfiore S, et al. Effect of the intracellular localization of a Gd-based imaging probe on the relaxation enhancement of water protons. *Magnetic Resonance in Medicine*. 2006; 55: 491-497.
- Townson JL, Ramadan SS, Simeone C, et al. Three-dimensional imaging and quantification of both solitary cells and metastases in whole mouse liver by magnetic resonance imaging. *Cancer Research*. 2009; 69: 8326-8331.
- Vlad RM, Kolios MC, Czarnota GJ, et al. Evaluating the extent of cell death in 3D high frequency ultrasound by registration with whole-mount tumour histopathology. *Medical Physics*. 2010; 37: 4288-4297.
- de Vries IJ, Lesterhuis WJ, Barentsz JO, et al. Magnetic resonance tracking of dendritic cells in melanoma patients for monitoring of cellular therapy. *Nature Biotechnology*. 2005; 23: 1407-1413.
- Willmann JK, Kimura RH, Deshpande N, et al. Targeted contrast-enhanced ultrasound imaging tumour angiogenesis with contrast microbubbles conjugated to integrin-binding Knottin peptides. *Journal of Nuclear Medicine*. 2010; 51:433-440.

## **Chapter 5.0: GENERAL DISCUSSION**

### **5.1 THESIS SUMMARY**

The primary objective of this thesis was to study and quantify the fate of tumour cells after arresting in draining lymph nodes in a preclinical model of melanoma. To accomplish this, the second chapter of this thesis describes the development of a new lymph node experimental metastasis assay (LEMA) that permits a “cell accounting” analysis where the percentage of tumour cells of the original injectate that survived to form various types of metastatic lesions in the lymph node can be calculated at progressive time intervals. From this analysis, we were able to demonstrate how metastasis formation in the lymph node is an inefficient process where only 0.08% of the tumour cells that arrive are able to form lymph node tumours.

The third chapter of this thesis demonstrates the utility of HFUS in the non-invasive and longitudinal study of the growth of lymph node metastases, using the same animal model described in the second chapter. The growth rate of lymph node metastases varied from mouse to mouse, and in some cases, the metastatic lesion did not change in volume over 6 days. The most striking finding of this study was how small micrometastatic lesions appeared hyperechoic (bright) within the lymph node. The high contrast of these small metastatic lesions permitted the observation of their growth over time. The unprecedented ability of HFUS to track the growth of micrometastases provide a new avenue to

study and assess the efficacy of chemotherapeutics on the growth of micrometastatic deposits in a preclinical model.

The fourth chapter of this thesis deals with developing *in vitro* quantitative methods for assessing tumour cell number by positive contrast cellular imaging at 3T MRI. To demonstrate the potential utility of positive contrast MRI in accurately assessing tumour cell number *in vivo* at clinical field strength, an *in vitro* MRI phantom was developed to contain a series of cell pellets with increasing amounts of positive contrast-labeled cells. This *in vitro* study provides evidence demonstrating a strong positive correlation between the change in positive contrast signal enhancement and tumour cell number. The change in  $R_1$  values were also found to strongly correlate with tumour cell number. This study will be informative for future research exploring the use of positive contrast labeling in assessing tumour burden at secondary organs.

## **5.2 DISCUSSION – ASSESSING THE FATE OF ISOLATED TUMOUR CELLS AND MICROMETASTASES IN THE DEVELOPMENT OF OVERT LYMPH NODE METASTASES**

### **5.2.1 The need for a new model of lymph node metastasis**

Assessing the fate of tumour cells after they arrest in draining lymph nodes was a difficult task to undertake since current animal models of lymphatic metastasis use the spontaneous metastasis assay to study the initial steps of lymphatic metastasis. In a spontaneous metastasis assay, tumour cells spontaneously metastasize from an artificial primary tumour that is created by the orthotopic injection of tumour cells in the appropriate tissue or organ. This is a stochastic model in that the researcher has no control on the timing and number of cells that arrive in the draining lymph node. Therefore, a new model of lymph node metastasis was created to study the latter half of lymphatic metastasis – metastasis formation in the draining lymph node.

### **5.2.2 LEMA and metastatic inefficiency in the lymph node**

In LEMA, a suspension of tumour cells and reference beads is injected into the upstream (inguinal) lymph node where the fluid immediately exits and drains into the downstream (axillary) lymph node. From this point, LEMA recapitulates the progressive stages of metastasis development. In progressive time intervals, isolated tumour cells are seen at 90 minutes and 3 days, followed by micrometastases at 3 and 7 days, and then overt metastases are seen at 7



and 14 days post-injection. Since tumour cells were co-injected with similarly sized reference beads, a “cell accounting” analysis permitted the quantification of tumour cell survival as isolated tumour cells, micrometastases, and overt metastases was calculated. From this analysis, it became apparent that metastasis formation is an inefficient process. Ninety percent of the tumour cells that arrested in the lymph node were lost from 90 minutes to 3 days. At 3 days, 0.3% of the original inoculum were able to form micrometastases. At 7 days, no isolated tumour cells were found, 0.006% and 0.002% of the tumour cells that arrested were able to form micrometastases and overt metastases, respectively. Finally at 14 days, 0.003% and 0.08% of the tumour cells were able to form micrometastases and overt metastases, respectively.

### **5.2.3 Clinical relevance**

This is the first study to provide a detailed quantitative assessment of tumour cell fate in lymph nodes. The major conclusions from this study are that the majority of tumour cells (90%) that arrive in the lymph node do not form metastases, and only a small subset (0.08%) form overt lymph node tumours, for the cell line used here. Despite these interesting biological findings, the relevant question remains: How do these findings translate to patient care in the clinic? Indeed the removal of lymph node tumours are part of standard clinical practice in patient staging and controlling local spread (Meng et al, 2011). However, this procedure is associated with adverse affects such as seroma, inflammation, infection, and lymphedema in patients (Meng et al, 2011). Therefore, a practical

application of the current model is in the development of novel intralymphatic anti-metastatic therapeutics that reduces or eliminates lymph node tumours. If lymph node tumour burden can be reduced or eliminated altogether, this may spare patients from undergoing radical axillary lymph node dissection.

#### **5.2.4 Future studies**

Intravital fluorescence videomicroscopy (IVFVM) can be used to directly determine if sinus histiocytes are responsible to tumour cell toxicity during the initial stages of lymph node colonization. LEMA utilizes two lymph nodes that are interconnected. In **Chapter 2.0**, the inguinal lymph node was the site of injection, and the downstream axillary lymph node was where tumour formation occurred. However, any pair of interconnected lymph nodes can be studied in this manner. The inguinal lymph node is highly accessible for intravital imaging (von Andrian, 1996). Therefore upstream intralymphatic injection of 3  $\mu\text{m}$  bead-labeled, fluorescent tumour cells can permit IVFVM observation of tumour cell arrest and early colonization of the inguinal lymph node. IVFVM can be performed at 90 minutes, 24, 48, and 72 hours will permit the assessment of tumour cell interaction with sinus histiocytes. Parameters such as the number of sinus histiocytes, fluorescent tumour cells with 3  $\mu\text{m}$  beads, and sinus histiocytes with 3  $\mu\text{m}$  beads at each time point can determine if the loss of tumour cells is accompanied by a concomitant increase in sinus histiocytes that contain 3  $\mu\text{m}$  beads.

### **5.3 DISCUSSION – HIGH-FREQUENCY (40 MHz) ULTRASOUND IMAGING OF THE DEVELOPMENT OF EXPERIMENTAL LYMPH NODE METASTASES**

#### **5.3.1 The utility of HFUS in tracking the dynamic growth of lymph node tumours**

The previous study utilized LEMA to ascertain the fate of tumour cells after they arrest in draining lymph nodes. Through detailed time end-point experiments, metastatic progression was found to be an inefficient process. One major caveat of time end-point experiments is that one cannot track the future or the past of a metastatic lesion observed (Chambers et al 2002). To address the limitation of this experimental approach, the current study employs the same animal model to demonstrate the utility of HFUS in the non-invasive and longitudinal study of the dynamic growth of lymph node metastases.

HFUS has been previously demonstrated to be a relatively safe, inexpensive, and time efficient method in the non-invasive and serial acquisition of high resolution (40  $\mu\text{m}$ ), 3D information on metastatic growth in the liver (Graham et al, 2005). The current study used HFUS to characterize the development of lymph node tumours. With a scan time of 8 minutes per mouse, the user can acquire information such as 3D volume, RI, B-mode brightness, and percent vascularity. The sensitivity and specificity of each parameter in differentiating metastatic from non-metastatic lymph nodes is reported. From longitudinal observations of changes in lymph node volumes, the growth rate of lymph nodes that developed into large tumours varied considerably from mouse

to mouse. This is reflected in 14-day end-point volumes which ranged from ~98 to 543 mm<sup>3</sup>; for comparison, normal lymph node volumes ranged from 8.5 to 12.9 mm<sup>3</sup>.

### **5.3.2 Non-invasive and longitudinal imaging of micrometastases**

A surprising observation in this study was the hyperechoic appearance of lymph node metastasis in B-mode images. Metastases from several different cell lines were previously reported to be hypoechoic in the liver (Graham et al, 2005). Analysis of ultrasound images reveals how the B-mode brightness of metastatic lymph nodes significantly increases over time compared to non tumour-bearing lymph nodes, which exhibited no significant change over time. The most striking feature about this study was the ability to track hyperechoic metastatic deposits as small as a micrometastasis (< 2 mm in diameter). In mice with metastatic lymph nodes, a subset of mice (3 out of 10) had lymph nodes with metastatic deposits that were only apparent by ultrasound; these small, non-palpable metastatic deposits, ranged from 1.2 to 4.4 mm in diameter. When experimental end-point was reached at 14 days, lymph nodes were processed for histological analysis of tumour burden. Stereological analysis revealed a strong positive correlation ( $r^2 = 0.94$ ) between 2D measurement of histological tumour burden and 3D ultrasound volumetric measurements of tumour burden. The capability of HFUS to reliably track micrometastatic deposits opens a new avenue of research to non-invasively study the progression of micrometastatic disease within the lymph node.

### **5.3.3 Clinical relevance**

The ability to track changes in metastatic burden in lymph nodes would prove to be highly useful in assessing the efficacy of anti-metastatic intervention in preclinical treatment models. Therapies that prove to be efficacious in delaying the progression of micrometastatic disease, or reducing lymph node tumour burden in human xenograft mouse models can potentially translate to the treatment of patients in the clinic.

### **5.3.4 Future work**

Future research studying lymph node metastases can use HFUS in determining whether lymph node tumours contribute to further systemic dissemination of metastatic cells. In 2008, Rebhun and colleagues demonstrated that lymph node tumours seeded the lungs with metastases as equally well as primary tumours in the ear skin. By using the same mouse ear tumour model, HFUS can be used to monitor the growth of lymph node tumours and determine whether lymph node metastatic burden is correlated with the number of pulmonary metastases. Furthermore, lymph node tumour burden can potentially be reduced by high intensity focus ultrasound HIFU ablation. HFUS can be used to monitor the effects of HIFU ablation on lymph node tumour burden and to determine whether the average number of pulmonary metastases is significantly different from mice with lymph node tumours that did not receive HIFU ablation

treatment. If the average number of pulmonary metastases is significantly reduced by treating lymph node tumours with HIFU ablation, then this would provide evidence supporting the notion that lymph node tumours act as reservoirs of metastatic cells that can further disseminate into system circulation.

## **5.4 DISCUSSION - THE CELLULAR DETECTABILITY OF POSITIVE CONTRAST-LABELED TUMOUR CELLS AT CLINICAL FIELD STRENGTH MRI**

### **5.4.1 Problems in quantifying iron-oxide labeled tumour cells**

Imaging single tumour cells at the metastatic site has been previously demonstrated (Heyn et al, 2006; Townson et al, 2009; Foster et al, 2008). These authors demonstrate the sensitivity in detecting the presence of tumour cells that were labeled with superparamagnetic iron-oxide particles. However, quantification of the number of iron-oxide-labeled cells becomes problematic when imaged in “bulk” where the tumour cells’ respective signal voids overlap (Heyn et al, 2006; Townson et al, 2009).

To address this limitation, cellular labeling with paramagnetic gadolinium-based contrast agents are favorable since they do not produce a local susceptibility artifact (signal void), but rather, the local accumulation of gadolinium ions causes voxels to appear brighter. Although not as sensitive as iron-oxide on a per millimolar basis, this is compensated by developing strategies in delivering a higher payload of Gd-chelates to the target, or increasing the relaxivity of the Gd-chelate itself.

#### **5.4.2 Assessment of tumour cell number by positive contrast cellular MRI *in vitro***

The current study explores the feasibility of imaging GdF-labeled breast cancer cells at 3T MRI. To demonstrate whether MR parameters such as signal enhancement and  $R_1$  relaxation rate can measure the abundance of GdF-labeled tumour cells, an agarose *in vitro* MR phantom was constructed to contain a series of cell pellets with increasing ratios of GdF-labeled cells to unlabeled cells. In using a 3D SPGR pulse sequence with a 10 degree flip angle, we were able to demonstrate a strong and positive correlation ( $r^2 = 0.94$ ) between the changes in signal enhancement and tumour cell number. A  $T_1$  map of the cell pellets was constructed and  $R_1$  values for each cell pellet were calculated. Comparing  $R_1$  values to the number of GdF-labeled cells by linear regression analysis reveals a strong, positive correlation ( $r^2 = 0.94$ ). These results show that positive contrast cellular MRI can be used to quantify the abundance of tumour cells under *in vitro* conditions. Furthermore, the cell pellet with the smallest amount of GdF-labeled cells that produced a measurable change in mean  $R_1$  values was  $4 \times 10^5$  labeled cells or 546 labeled cells per voxel.

#### **5.4.3 Clinical relevance**

Assessing metastatic tumour burden in patient lymph nodes is important in staging of the disease and influences the choice of therapy. Information from current research, such as MR pulse sequence parameters, can be used in the



assessment of targeted Gd-based contrast agents developed for *in vivo* quantification of metastatic tumour burden in the lymph nodes. The use of targeted Gd-based contrast agents may provide a more accurate assessment of metastatic tumour burden which can spare patients from undergoing unnecessary lymph node dissection procedures and avoid adverse events such as seroma, infection and lymphoedema (Meng et al, 2010).

#### **5.4.4 Future work**

The current work sets the stage for *in vivo* quantification of metastatic tumour cells in the secondary organ. Future work can assess a clinically used Gd-chelate conjugated to a human tumour-specific targeting moiety such as mAb 2C5, an anti-nuclear antibody (Erdogan et al, 2008). The novel Gd-chelate-mAb2C5 contrast agent would be tested *in vitro* (similar to the current research) to determine the lower limit of human tumour cell detection at 3T MRI. For *in vivo* experiments, LEMA would be used with human tumour cells to induce the formation of lymph node tumours. The Gd-chelate-mAb2C5 contrast agent would be tested in a cohort of 8 mice with lymph node tumours to determine if the contrast agent is selectively retained in lymph node metastases. Administration of untargeted Gd-chelate into a separate cohort of 8 lymph node tumour-bearing mice would serve as a control. Signal enhancement and  $R_1$  values of lymph node tumours of mice that received targeted Gd-chelate-mAb2C5 contrast agent would be compared to lymph node tumour-bearing mice that received non-targeted Gd-chelate. A significant increase in signal enhancement or  $R_1$  values in lymph node

tumour-bearing mice would demonstrate Gd-chelate-mAb2C5 is a contrast agent that can specifically detect human lymph node tumours.

## 5.5 CONCLUSIONS

Tumour cell dissemination to draining lymph nodes and the establishment of metastases are parts of the natural history of many types of cancer. Assessment of the number and extent of lymph node tumours is crucial in disease staging and influences the choice of treatment. The current thesis explored the uncharted events after tumour cells arrest in draining lymph nodes. It was discovered that the majority of tumour cells (90%) are lost during the initial stages of colonization. Metastatic progression of the few surviving tumour cells proceeded in an inefficient manner where only 0.08% of the original cells that arrived were able to successfully form overt metastases. To understand the dynamic growth of lymph node tumours *in vivo*, we utilized HFUS to longitudinally assess lymph node tumour growth in individual mice. Heterogeneity in lymph node tumour growth rate was observed from mouse to mouse. The current thesis demonstrates how HFUS has the unprecedented capability to longitudinally track the progression of micrometastatic disease in murine lymph nodes. This should be a useful tool in future metastasis research that studies the growth of micrometastatic deposits and assesses how they respond to anti-metastatic therapeutics. The final work of this thesis demonstrates the capability of clinical strength MRI to detect and quantify the abundance of tumour cells, under *in vitro* conditions. This will pave the way for future studies that evaluate novel targeted gadolinium-based contrast agents that can aid in the accurate assessment of metastatic tumour burden in cancer patients.

## 5.6 References

- Chambers AF, Groom AC, MacDonald IC. Dissemination and growth of cancer cells in metastatic sites. *Nature Reviews Cancer*. 2002; 2:563-572.
- Erdogan S, Medarova ZO, Roby A, et al. Enhanced tumor MR imaging with gadolinium-loaded polychelating polymer-containing tumor-targeted liposomes. *Journal of Magnetic Resonance Imaging*. 2008; 26: 574-580.
- Foster PJ, Dunn EA, Karl KE et al. Cellular magnetic resonance imaging: in vivo imaging of melanoma cells in lymph nodes of mice. *Neoplasia*. 2008; 10: 207-216.
- Graham KC, Wirtzfeld LA, MacKenzie LT, et al. Three-dimensional high-frequency ultrasound imaging for longitudinal evaluation of liver metastases in preclinical models. *Cancer Research*. 2005; 65: 5231-5237.
- Heyn C, Ronald JA, Ramadan SS, et al. In vivo MRI of cancer cell fate at the single-cell level in a mouse model of breast cancer metastasis to the brain. *Magnetic Resonance in Medicine*. 2006; 56:1001-1010.
- Meng Y, Ward S, Cooper K, et al. Cost-effectiveness of MRI and PET imaging for the evaluation of axillary lymph node metastasis in early stage breast cancer. *European Journal of Surgical Oncology*. 2011; 37: 40-46.

Rebhun RB, Lazar AJ, Fidler IJ. Impact of sentinel lymphadenectomy on survival in a murine model of melanoma. *Clinical and Experimental Metastasis*. 2008; 25:191-199.

Townson JL, Ramadan SS, Simeone C, et al. Three-dimensional imaging and quantification of both solitary cells and metastases in whole mouse liver by magnetic resonance imaging. *Cancer Research*. 2009; 69: 8326-8331.

von Andrian UH. Intravital microscopy of the peripheral lymph node microcirculation in mice. *Microcirculation*. 1996; 3: 287-300.

## APPENDIX 1 - COPYRIGHT AGREEMENT

14/01/2011

Rightslink® by Copyright Clearance Ce...

Powered by **RIGHTSLINK**  [Home](#) [Account Info](#) [Help](#)  
COPYRIGHT CLEARANCE CENTER, INC.



**Title:** A New Breast Cancer Model for Lymphatic Metastasis  
**Author:** Michael Lizardo  
**Publication:** Springer eBook  
**Publisher:** Springer  
**Date:** Sep 5, 2007  
 Copyright © 2007, Springer US

Logged in as:  
Michael Lizardo

[LOGOUT](#)

### Order Completed

Thank you very much for your order.

This is a License Agreement between Michael M Lizardo ("You") and Springer ("Springer"). The license consists of your order details, the terms and conditions provided by Springer, and the [payment terms and conditions](#).

[Get the printable license](#).

License Number	2587790073064
License date	Jan 14, 2011
Licensed content publisher	Springer
Licensed content publication	Springer eBook
Licensed content title	A New Breast Cancer Model for Lymphatic Metastasis
Licensed content author	Michael Lizardo
Licensed content date	Sep 5, 2007
Type of Use	Thesis/Dissertation
Portion	Full text
Number of copies	1
Author of this Springer article	Yes and you are a contributor of the new work
Title of your thesis / dissertation	Biological and Imaging Studies on Experimental Lymph Node Metastasis
Expected completion date	Apr 2011
Estimated size(pages)	120
Total	0.00 CAD

[CLOSE WINDOW](#)

Copyright © 2011 [Copyright Clearance Center, Inc.](#) All Rights Reserved. [Privacy statement](#).  
 Comments? We would like to hear from you. E-mail us at [customercare@copyright.com](mailto:customercare@copyright.com)

## APPENDIX 2 – ETHICS APPROVAL FOR USE OF ANIMAL SUBJECTS



09.21.09

**\*This is the Original Approval for this protocol\***  
 \*A Full Protocol submission will be required in 2013\*

Dear Dr. Chambers:

Your Animal Use Protocol form entitled:

Steps of Breast Cancer Metastasis: Experimental Models and Identification of Targets for Intervention.

Funding Agency CBCRA - Grant#No. 016506; LHR F7224, LHR F7227, LHR F7225

has been approved by the University Council on Animal Care. This approval is valid from **09.21.09 to 09.30.10**.

The protocol number for this project is **2009-072**.

1. This number must be indicated when ordering animals for this project.
2. Animals for other projects may not be ordered under this number.
3. If no number appears please contact this office when grant approval is received.  
 If the application for funding is not successful and you wish to proceed with the project, request that an internal scientific peer review be performed by the Animal Use Subcommittee office.
4. Purchases of animals other than through this system must be cleared through the ACVS office. Health certificates will be required.

#### ANIMALS APPROVED FOR 4 Years

Species	Strain	Other Detail	Pain Level	Animal # Total for 4 Years
Mouse	Various As outlined in protocol	5-6 weeks; Female	D	683

#### REQUIREMENTS/COMMENTS

Please ensure that individual(s) performing procedures on live animals, as described in this protocol, are familiar with the contents of this document.

**The holder of this Animal Use Protocol is responsible to ensure that all associated safety components (biosafety, radiation safety, general laboratory safety) comply with institutional safety standards and have received all necessary approvals. Please consult directly with your institutional safety officers.**

c.c. A Tuck, J Lewis, I MacDonald, N Hague, K Bothwell, P Coakwell, W Lagerwerf

*The University of Western Ontario*  
 Animal Use Subcommittee / University Council on Animal Care  
 Health Sciences Centre, • London, Ontario • CANADA – N6A 5C1  
 PFI: 519-661-2111 ext. 86770 • FL 519-661-2028 • www.uwo.ca / animal

# CURRICULUM VITAE

Page 1 of 5

## Michael Mark Lizardo

Canadian Citizen

Department of Medical Biophysics  
1151 Richmond St. N, Medical Science Building  
University of Western Ontario  
London, Ontario, Canada  
N6A 5C1

### Education

Doctor of Philosophy	2005-2011	<b>University of Western Ontario</b> Department of Medical Biophysics Thesis: <i>From Isolated Tumour Cells to Overt Lymph Node Metastases: Biological and Imaging Studies on the Development of Experimental Lymph Node Metastases</i> Supervisors: Drs. AF Chambers & IC MacDonald
Master of Science	2003-2005	<b>University of Manitoba</b> Department of Pathology Thesis: <i>Adhesive Interactions between Lymphatic Endothelial Cells and Melanoma Cells in a Mouse Model</i> Supervisor: Dr. FW Orr
Bachelor of Science Honours	1996-2001	<b>University of Winnipeg</b> Department of Biology Thesis: <i>Mitochondrial Fusion and Flagellar Growth during Spermiogenesis in the Insect <i>Rhodnius prolixus</i></i> Supervisor: Dr. E. Byard

### Awards and Scholarships

Date:	Total Amount:	Duration of Award:	Title of Award & Organization:
Sept. 2010	\$15,425	2 semesters	Studentship from the Translational Breast Cancer Research Unit of the London Regional Cancer Program
Sept. 2009	\$18,500	1 year	Studentship from the Translational Breast Cancer Research Unit of the London Regional Cancer Program
Sept. 2008	\$18,500	1 year	Studentship from the Translational Breast Cancer Research Unit of the London Regional Cancer Program
Sept. 2007	\$18,500	1 year	Studentship from the Translational Breast Cancer Research Unit of the London Regional Cancer Program
May 2007	\$2000	1 semester	Schulich Graduate Scholarship



**Awards and Scholarships**


---

Jan. 2007	\$2000	1 semester	Schulich Graduate Scholarship
Sept. 2006	\$18,500	1 year	Studentship from the Translational Breast Cancer Research Unit of the London Regional Cancer Program
Sept. 2005	\$10,000	2 years	Canadian Institute of Health Research Strategic Training Fellow in Vascular Research, Robarts Research Institute
Sept. 2005	\$18,500	1 year	Studentship from the Translational Breast Cancer Research Unit of the London Regional Cancer Program
May/ Sept. 2005	\$4000	2 semesters	Western Graduate Research Scholarship, University of Western Ontario
Sept. 2002	\$3000	2 years	John A. Grey Fellowship International Association of Dental Research
July. 2001	\$3000	2 months	Summer Studentship Head and Neck Cancer Foundation

**Research Experience**


---

Imaging Technician	Sept.2004-Dec.2005	<b>Genomic Center for Cancer Research &amp; Diagnosis, CancerCare Manitoba</b> Responsible for user training and maintenance of Zeiss microscope center.
Research Technician 1	Mar.2002-Jun.2002	<b>Manitoba Institute of Cell Biology, CancerCare Manitoba</b> Short-term project on genomic instability in head and neck cancer.
Research Technician 3	Sept.2002-Feb.2003	<b>Department of Oral Biology, University of Manitoba</b> Studied genomic instability in oral cancer.
Summer Research Assistant	Jul.2001-Aug.2001	<b>Department of Oral Biology, University of Manitoba</b> Studied lung surfactant proteins in a murine model of obesity

**Teaching Experience**


---

Teaching Assistant in 4 <sup>th</sup> year Medical Sciences	2007-2010	University of Western Ontario, Medical Science Program
Teaching Assistant in 3 <sup>rd</sup> year Medical Biophysics	2006-2009	University of Western Ontario, Department of Medical Biophysics

Teaching Assistant in 3 <sup>rd</sup> year Cell Biology	1998-2001	University of Winnipeg, Department of Biology
Teaching Assistant in 3 <sup>rd</sup> year Histology	1998-2001	University of Winnipeg, Department of Biology
Teaching Assistant in 1 <sup>st</sup> year Biology.	1998-2001	University of Winnipeg, Department of Biology

### Research Skills/Techniques

---

#### *Laboratory Techniques:*

Working experience in cell culture techniques, western blotting, paraffin/fresh frozen tissue embedding & sectioning, haematoxylin & eosin staining, immunohistochemistry, immuno-fluorescence staining, fluorescent *in situ* hybridization, combined protein and FISH analysis, chromosome preparation, G-banding, molecular biology techniques, and mammalian cell transfections. Certified in small animal handling (mouse and rat). Small animal (mouse) imaging using intravital fluorescence videomicroscopy techniques (Zeiss and Olympus inverted microscopes), and high frequency ultrasound (Vevo770 High Resolution *In Vivo* Micro-Imaging System). Hands on knowledge of lung, liver, lymph node experimental metastasis assays, and orthotopic spontaneous metastasis assays (mammary fat pad, subcutaneous, and intradermal tumour formation). Knowledgeable in stereological/image analysis, and statistical analysis.

#### *Computer Skills:*

Working knowledge of Windows XP, MacOS, Microsoft Word, Excel, Powerpoint, GraphPad, ImageJ, Adobe Photoshop, Adobe Illustrator, Adobe Acrobat, Macromedia Flash, Rasmol. In addition, I have experience with microscope software packages such as Axiovision v4.3 (Zeiss), MacProbe v4.4 (Applied Imaging), Northern Eclipse v7.0 (Empix Imaging), and Metasystems Group software such as Isis, Ikaros, and Metafer.

### Attended Scientific Meetings, Workshops, and Training Courses

---

June 2010	Department of Oncology (U.W.O) Research and Education Day (poster presentation). Awarded a Best Poster Award.
April 2010	101 <sup>st</sup> Annual Meeting of the American Association for Cancer Research (poster presentation)
May 2008	Reasons for Hope Conference, Montreal Quebec (poster presentation)
June 2007	Department of Oncology (U.W.O) Research and Education Day (invited seminar)
June 2006	Department of Oncology (U.W.O) Research and Education Day (poster presentation)
May 2006	Reasons for Hope Conference, Montreal Quebec (poster presentation)
Aug. 2005	Teaching Assistantship Training Program, University of Western Ontario
Apr. 2005	Animal Care and Use Training Course, Animal Care and Veterinary Services, University of Western Ontario
Jun. 2004	17 <sup>th</sup> Annual Canadian Student Health Research Forum (poster presentation)
Mar. 2004	94 <sup>th</sup> Annual Meeting of the American Association of Cancer Research
Aug. 2002	1 <sup>st</sup> Annual Meeting of the Society of Biological Imaging in Boston Massachusetts.
Sept. 2001	Fluorescent <i>In Situ</i> Hybridization & Imaging Workshop Genomic Center for Cancer Research and Diagnosis Inc.
Feb. 2001	Prairies Universities Biological Symposium (invited seminar)

### **Academic and Mentorship Activities**

---

- 2007/8 Served as a reviewer on University of Western Ontario Academic Development Fund
- 2007 mentored Alexander Graves, 3<sup>rd</sup> year student in Medical Sciences, currently an M.Sc. student in Dr. Mai's laboratory, Manitoba Institute of Cell Biology, Winnipeg, Manitoba
- 2008 mentored Baraa Al-Khazraji, 3<sup>rd</sup> year student in Medical Biophysics, currently a Ph.D. student in Dr. Jackson's laboratory, Dept. of Medical Biophysics, University of Western Ontario, London, Ontario
- 2009 mentored Leonard Guizzetti, 4<sup>th</sup> year project student in Medical Biophysics, currently an M.Sc. student in Dr. Dhanvantari's laboratory, Lawson Health Research Institute, London, Ontario
- 2008/9 mentored Dean B. Percy, 4<sup>th</sup> year project student in Medical Biophysics, currently an M.Sc. student in Dr. Foster's laboratory, Robarts Research Institute, London, Ontario
- 2009 mentored Marianne Stroz, 3<sup>rd</sup> year student in Medical Biophysics, currently a 4<sup>th</sup> year Honours student, Dept. of Medical Biophysics, University of Western Ontario, London, Ontario
- 2010 mentored Matthew Lowerison, 3<sup>rd</sup> year student in Medical Biophysics, Dept. of Medical Biophysics, University of Western Ontario, London, Ontario

### **Community Involvement**

---

- Volunteered for Rose in My Book fundraising group, London Ontario (2009)
- Volunteered for Cancer Relay For Life, London, Ontario (June 2007, 2008)
- Member of PrideWestern student group, University of Western Ontario
- Volunteered for training as an Ally Western Facilitator, University of Western Ontario (2006)
- Volunteered for Pride London Film Festival and other Pride London social events (2007)
- Volunteered for the London Fringe Theatre Festival (2006)

### **Publications (abstracts and peer-reviewed articles)**

---

#### *Abstracts*

1. Lizardo MM, Hague MN, Tuck AB, MacDonald IC, Chambers AF. 2010. A New Model to Study the Metastatic Colonization of Murine Lymph Nodes (abstract). 2010 Department of Oncology Research and Education Day.
2. Lizardo MM, Ronald JA, Chen Y, Misselwitz B, Schuets G, Rutt, BK, Chambers AF. 2010. Cellular MRI of a Lymphotropic Human Breast Cancer Cells Labeled with Gadofluorine M (abstract). 2010 Annual Meeting of the American Association of Cancer Research.
3. Lizardo MM, Al-Khazraji B, Percy DB, Wirtzfeld LA, MacDonald IC, Fenster A, Laceyfield JC, Chambers AF. 2008. Optical Fluorescence and High Frequency (40MHz) Ultrasound Imaging of Spontaneous Lymph Node Metastases in a Xenograft Model of Breast Cancer. 2008 Reason for Hope Meeting, Canadian Breast Cancer Research Association.
4. Lizardo MM, Groom AC, MacDonald IC. Intravital Videomicroscopy of Lymphatic Metastasis. 2006 Reason for Hope Meeting, Canadian Breast Cancer Research Association
5. Lizardo MM, Qiu H, Qi K, Orr FW. 2004. The Adhesion Interactions between Metastatic Melanoma Cells and Lymphatic Endothelial Cells in a Mouse Model (Abstract). 2004 *Canadian Student Health Research Forum*.

6. Lizardo MM. 2001. Expression of the Mitochondrial Fusion Protein (Fuzzy Onions) during Spermiogenesis in the insect (Abstract). 2001 *Prairie Universities Biological Symposium*.

*Peer-reviewed articles*

1. Lizardo MM, Hague MN, Morris V, Tuck AB, MacDonald IC, Chambers AF. 2010. Metastatic Inefficiency in the colonization of murine lymph nodes. (*Manuscript in preparation*)
2. Lizardo MM, Hague MN, MacDonald IC, Lacefield JC, Chambers AF. 2010. Non-invasive imaging of (micro)metastatic deposits in the lymph nodes using 3D high-frequency (40Mhz) ultrasound. (*Manuscript in preparation*)
3. Lizardo MM, Ronald JA, Yuanxin C, Misselwitz B, Rutt BK, Chambers AF. 2010 Cellular detectability of positive contrast (gadofluorine-M)-labeled cancer cells in an *in vitro* phantom of a lymph node. (*Manuscript in preparation*)
4. Leong HS, Lizardo MM, Nambiar SC, Ablack A, Kim D, Chambers AF, Lewis JD. 2009. *In vivo* visualization of epithelial-mesenchymal transition in real time using a rapidly tuneable E-cadherin. (*submitting to Nature Methods*)
5. Lizardo MM, MacDonald IC, Tuck AB, Chambers AF. 2007. A new breast cancer model for lymphatic metastasis. In: *Cancer Metastases and the Lymphovascular System: Basis for Rational Therapy*. S.P.L. Leong, (editor). New York: Springer. 11: 157-165. Invited book chapter.
6. Webb M, Emberly ED, Lizardo MM, Alowami S, Quing G, Alfiar A, Snell-Curtis LJ, Niu Y, Civetta A, Myal Y, Shiu R, Murphy L, Watson PH. 2005. Expression analysis of the mouse S100A7/psoriasin gene in skin inflammation and mammary tumorigenesis. *BMC Cancer*. 5:1-16.
7. Qi K, Qiu H, Sun D, Minuk G, Lizardo MM, Rutherford J, Orr FW. 2004. Impact of cirrhosis on the experimental hepatic metastases of B16F1 melanoma cells in C57BL/6 mice. *Hepatology*. 40:1144-1150.